8-22-2014 12:00 AM

Gamma-Radiolysis Kinetics of Liquid, Vapour and Supercritical Water

Nastaran Yousefi, *The University of Western Ontario*

GAMMA-RADIOLYSIS KINETICS OF LIQUID, VAPOUR AND SUPERCRITICAL WATER

(Thesis format: Integrated Article)

by

Nastaran <u>Yousefi</u>

Graduate Program in Chemistry

A thesis submitted in partial fulfillment
of the requirements for the degree of
Master of Science

The School of Graduate and Postdoctoral Studies
The University of Western Ontario
London, Ontario, Canada

i

Abstract

Inadequate understanding of radiation-induced water chemistry under supercritical conditions has been identified as one of the important obstacles in the development of a supercritical water-cooled reactor. Radiolysis of supercritical water generates a variety of redox reactive species, but their persistence in supercritical water is not well understood. This thesis describes the work performed towards addressing this deficiency: (1) the development of a reliable experimental method to determine the concentrations of water radiolysis products, primarily H_2, O_2 and H_2O_2, formed under γ-irradiation of sub- and supercritical water (SCW), (2) the expansion of the application ranges of the existing γ-radiolysis kinetic models for liquid water and water vapour to high temperatures and pressures, and (3) the development of the first versions of the supercritical water radiolysis models based on these two models. With each model calculations were performed as a function of temperature and the computational results were analysed to identify the key reactions and reaction parameters that are important in determining the effect of temperature on the net radiolytic production of H_2, O_2 and H_2O_2. The results indicate that the model approach that has been taken is promising and worthy of further development.

Keywords:

Acknowledgments

First and foremost I offer my sincerest gratitude to my supervisor, Dr. J. Clara Wren, who has supported me throughout my study with her patience and incredible knowledge while giving me the independence to work in my own way. I have gratefully benefited from her faith in me, encouragement and effort which made my Master degree a journey to remember. One simply could not wish for a better mentor and I could not thank her enough for giving me the opportunity to work under her supervision for two years.

I would also like to offer my special thanks to Dr. Jiju Joseph for her welcoming personality and never-ending aid in scientific discussions, and her assistance in experimental aspects of my work. I am particularly grateful for advice and comments given by Dr. Jamie Noël for experimental design. His insight has been a tremendous help during my study. Dr. Dave Wren's meticulous comments were an enormous help in the writing process and without his help this dissertation would have not been materialized.

In my daily work I have been blessed with a friendly and cheerful group of fellow students. They have been a marvelous group to work with. Also, the experience of spending times with them outside the lab was priceless.

Beyond Chemistry, I have been blessed with supportive family and friends that without any doubts made me the most fortunate person during my study. Their invaluable presence and help during difficult times of my life were much appreciated and could not be exchanged with anything else.

Table of Contents

Symbols and Acronyms

Symbols

A	absorbance
a	absorptivity
b	cell light path-length
c	concentration
cP	centipoise
D	diffusion coefficient
D_R	dose rate
e	electron charge
E_A	activation energy
E_{KE}	average kinetic energy
h	Plank constant
I	current
I	intensity
k	decay rate constant
k_B	Boltzmann constant
K_w	ionic product
P_{Cr}	critical pressure
P_{esc}	escape probability
Q	charge
r	effective radius
R	gas constant
r_c	onsager radius
R_s	onsager Radius
T	absolute temperature (K)
T_{Cr}	critical temperature
ε_0	dielectric constant of permittivity in a vacuum
ε_r	dielectric permittivity of a medium
η	viscosity
λ	wavelength
μ	mobility
ρ	density

Acronyms

AECL	Atomic Energy of Canada Limited
ASME	American Society of Mechanical Engineers
BPVC	Boiler and Pressure Vessel Code
GC	Gas Chromatography
GEN IV	Generation IV
GIF	Generation IV International Forum
IR	Infra Red
LET	Linear Energy Transfer
LRM	Liquid Radiolysis Model
MD	Molecular Dynamic
MS	Mass Spectroscopy
NMR	Nuclear Magnetic Resonance
PTFE	Polytetrafluoroethylene
SCW	Supercritical Water
SCWR	Supercritical Water-Cooled Reactor
SS	Stainless Steel
TCD	Thermal Conductivity Detector
UV	Ultraviolet
VRM	Vapour Radiolysis Model
μ-ECD	Micro cell Electron Capture Detector

List of Tables

List of Figures

CHAPTER 1
Introduction

1.1   Motivation and Rational

Ten countries joined together in January 2000 to form the Generation IV International Forum (GIF) to develop future advanced nuclear energy systems. Their objective is to have GEN IV systems available for international deployment by 2030 when many of the world's currently operating nuclear reactors will reach the end of their operating lives [1]. Several advanced reactor concepts have been selected by the GIF for development, one of which is a supercritical water-cooled reactor (SCWR).

The use of supercritical water (SCW) as the coolant in a nuclear reactor has long been considered as the natural evolution of water-cooled reactor technology because of the increased thermal efficiency higher temperature operation would provide [1-2]. Canada is developing a pressure-tube SCWR concept [3] that would operate with a core outlet temperature of 625 °C and a thermal efficiency of ~48%. However, the use of SCW as a reactor coolant poses some major challenges for the selection of in-core materials and an appropriate water chemistry control strategy that will enable in-core components to meet their service lives. The most important risk factor for materials performance is the corrosion rate of the fuel cladding, either as bulk metal loss or as localized corrosion. Although the effect of any dissolved oxygen on the corrosion of the candidate materials for fuel cladding (austenitic stainless steels and nickel-based alloys) in SCW remains unclear, it is clear that at

very high concentrations of oxidants the protective Cr-rich oxide film formed on many of these alloys can dissolve [4].

In a reactor core one of the main sources of oxidizing species in the coolant is radiolytic decomposition of water (radiolysis). As the coolant passes through the reactor core it is exposed to high fluxes of β and γ-radiation. Both forms of radiation are very effective in ionizing water molecules and breaking them into a number of redox active species [5]:

$$H_2O \xrightarrow{\gamma} \bullet OH, \bullet e_{aq}^{-}, \bullet H, H_2, H_2O_2, H^{+} \tag{1.1}$$

Recent measurements [6] using an SCW convection loop with an irradiation cell coupled to a 10 MeV, 10 kW linear electron accelerator [7] have demonstrated the risk of Cr oxide dissolution in an SCWR core due to the production of oxidizing conditions by water radiolysis.

The available data on the concentrations of oxidizing species in supercritical water in the radiation fields that are present in a reactor core are limited and the difficulties of performing well-controlled experiments on supercritical water means that this will likely remain the case for some time. While in-reactor experiments are planned [8] to measure the effect of ionizing radiation on the corrosion of materials under SCWR in-core conditions, until these data are available, it is necessary to use modelling to predict the expected concentrations of oxidizing species in an SCWR core. These predictions are needed to plan and perform out-of-reactor tests using water chemistries that mimic the expected in-core chemistry.

Predicting the concentrations of oxidizing species in the presence of continuous fluxes of ionizing radiation is also very difficult. Under continuous irradiation primary water radiolysis products are formed and react continuously, and the concentrations of important oxidizing species (such as $\bullet OH$, H_2O_2, O_2) reach a (pseudo-) steady state very quickly [5]. The steady-state concentrations of redox active species in irradiated water are strongly affected not only by the primary radiolysis production rate (reaction 1.1), but also by the subsequent chemical reactions of the primary radiolysis products with each other and other species that may be present. The concentrations cannot be predicted based on the kinetics of pairs of simple competition reactions. Consideration of multiple reactions linked together is required. Since the rates of elementary chemical reactions and mass transport rates will have different dependences on temperature and solvent properties the problem is even more complicated. Chemical kinetic modelling that includes large numbers of linked reactions is required to predict the steady-state concentrations of radiolysis products.

Supercritical water is an extremely challenging fluid that exists only at high temperatures and pressures (> 374 ºC and > 22 MPa). The solvation properties of water are important in controlling the chemical stability and transport behaviour of various species, particularly ions and radicals. These are factors that strongly influence reaction rates. Hence prediction of the concentrations of radiolysis products in SCW is not a simple extrapolation from modelling of room temperature water behaviour. Unfortunately, the effects of solvent properties in the sub- and supercritical water phases on reaction kinetics are not well established. The net impact of ionizing radiation on the concentrations of oxidizing species in supercritical water can be studied experimentally, but the data that will be obtained will

necessarily be somewhat limited to specific test conditions. The challenge in working with SCW will also limit the numbers of tests that can be performed.

To provide more immediately useful guidance for reactor designers, it is possible to develop a model for the radiolytic chemistry of supercritical water (SCW) (and water in the sub-critical regime near the critical point) with a view towards predicting the concentrations of key oxidization species as a function of coolant conditions (e.g., temperature). One of the most valuable applications of such model is its use to sort out the important from the unimportant reactions so that appropriate focus can be placed on ensuring that adequate accuracy of the rates of key reactions is obtained. In this regard, the data that is being obtained in supercritical water tests will provide crucial checks on the value of any modelling effort.

1.2   Research Objectives and Approaches

The overall research goal is to develop a sufficient understanding of steady-state radiolysis kinetics of SCW to be able to predict with reasonable accuracy the concentrations of key oxidizing species as a function of coolant conditions (e.g., temperature, hydrogen addition). Towards this goal, the objectives of this work were: (1) to develop a reliable experimental method to determine the concentrations of water radiolysis products, primarily H_2 and O_2, formed under γ-irradiation of sub- and supercritical water (SCW), and (2) to develop a chemical kinetic model for the radiolysis of sub- and supercritical water and to perform sensitivity analysis of the model to radiation and solution conditions.

Due to the high temperatures and pressures (> 374 ºC and > 22 MPa) of SCW, the design and construction of a radiolysis test cell for SCW radiolysis studies poses serious challenges, as the cell must satisfy several demanding criteria. Safety requirements and space limitations of the available γ-radiation chamber prevents on-line monitoring of the transient (reactive) radiolysis products using spectroscopic analyses. Thus, the experiments that can be performed will be limited to ex-situ analyses of thermally stable radiolysis products such as H_2 and O_2 gases. However, corrosion reactions of the materials that make up the radiolysis cell and gas-sampling lines (under SCW conditions) can influence the measurements of the radiolytically produced H_2 and O_2. Thus, to achieve objective (1), a main technical issue is minimization (ideally prevention) of such reactions. If surface reactions cannot be avoided, the effect the surface reactions under specific test conditions should be quantified. Calibration of the measured radiolysis product concentrations is not simple due to difficulties in preparing standard gas samples under SCW conditions. Thus, we needed to develop a method to introducing accurate concentrations of O_2 in SCW for calibration.

To date, only one model for the radiolysis chemistry of an early U.S. SCWR concept has been published [9]. While providing some valuable insights, that model included many simplifying assumptions that reduce its predictive value. A number of the physical properties of water (e.g., density and ion dissociation constant) change near the critical point [10,11]. The effects of the solvent properties of water on reaction kinetics in the sub- and supercritical water regimes are not well established and these properties can strongly impact on the model reactions.

Our objective is to develop a model for the radiation chemistry of water near the critical point that takes into account the influences of the changing water properties. We are approaching the modelling effort from two directions by developing two chemical kinetics models: (1) a liquid radiolysis model (LRM) and (2) a vapour radiolysis model (VRM). The liquid model (LRM) was constructed using a reaction set similar to that used in a radiolysis model that was developed and validated for liquid water at ambient temperatures [12–16]. The vapour model (VRM) uses the reaction set developed by Arkhipov et al. for vapour water radiolysis [17]. Comparison of the predictions of these models as the temperature approaches the SCW temperature should provide an insight into the effect of solvent properties on steady-state radiolysis kinetics, as the physical nature of supercritical water lies somewhere between a condensed state (liquid water) and a gas state (water vapour).

As the first step in developing the two models, the work performed under this thesis included: (1) critical evaluation of the reaction set and the rate constants as a function of temperature in the existing LRM and performing limited model validation experiments at 25, 150 ^{o}C and 250 ^{o}C, (2) assembling the reaction set and rate constants as a function of temperature for the VRM and coding them into software for solving the reaction kinetics by numerical integration, and (3) performing model simulations of the time dependent chemistry for radiolysis of pure water at temperatures ranging from 25 to 400 ^{o}C using both the LRM and VRM models.

1.3   Thesis layout

The layout of this thesis is as follows:

- Chapter 1 describes the motivation, rationale and objectives of the thesis.

- Chapter 2 presents the technical foundation for the work. It describes the properties of supercritical water, and the physics and chemistry of the interaction of radiation with matter.

- Chapter 3 provides information on the instrumentation, experimental procedures and analytical methods that were used in experiments.

- Chapter 4 describes the design and construction of a test cell to study the radiolysis of supercritical water. The design challenges and the evolution of the design are presented.

- Chapter 5 focuses on the gamma-radiolysis kinetics of liquid water. It contains description of a kinetic model designed for the radiolysis of liquid water and the bases for the model parameters. This chapter also includes model calculations for liquid water radiolysis at 25 °C, 150 °C and 250 °C and at different pHs.

- Chapter 6 describes the vapour radiolysis model and its parameters in detail. The temperature and pressure dependency of the vapour radiolysis products are presented in this chapter as well.

- Chapter 7 presents the experimental results from the radiolysis of biphasic liquid water and water vapour obtained at 25 °C, 150 °C and 250 °C. Also, model

simulation results are compared with experimental results.

- Chapter 8 addresses the assembly of two chemical kinetics models for the γ-radiolysis of sub-critical and supercritical water. The chapter includes preliminary predictions of the time dependent chemistry for radiolysis of water at temperatures near the critical temperature.

- Chapter 9 provides a conclusion and future work

1.4   References

[1]   "A Technology Roadmap for Generation IV Nuclear Energy Systems", U.S. DOE Nuclear Energy Research Advisory Committee and the Generation IV International Forum, 03-GA50034, Dec., 2002.

[2]   D. Danielyan, "Supercritical-Water-Cooled Reactor System - as One of the Most Promising Type of Generation IV Nuclear Reactor Systems", 2003.

[3]   D.R.M. Yetisir, M. Gaudet, "Development and Integration of Canadian SCWR Concept with Counter-flow Fuel Assembly", Proceedings of 6th International Symposium on Supercritical Water-Cooled Reactors (ISSCWR-6), Shenzhen, Guangdong, China, 2013.

[4]   S. Leistikow, "Isothermal Steam Corrosion of Commercial Grade Austenitic Stainless Steels and Nickel Base Alloys in Two Technical Surface Conditions", in: Proceedings of the Fourth International Congress on Metallic Corrosion (P:278), National Association of Corrosion Engineers, 1972.

[5]   J.W.T. Spinks, R.J. Woods, "An Introduction to Radiation Chemistry", 3rd ed., Wiley-Interscience, New York, 1990.

[6]   A.S. Bakai, D.A. Guzonas, V.N. Boriskin, A.N. Dovbnya, "Supercritical Water Convection Loop for SCWR Materials Corrosion Tests under Electron Irradiation: First Results and Lessons Learned", 6th International Symposium on Supercritical Water-Cooled Reactors (ISSCWR-6), Shenzhen, Guangdong, China, 2013.

[7]   A.S. Bakai, V.N. Boriskin, A.N. Dovbnya, D.A. Guzonas, "Supercritical Water Convection Loop (NSC KIPT) for Materials Assessment for the Next Generation Reactors", Proceedings of 5th International Symposium on Supercritical Water-Cooled Reactors(ISSCWR-5), March 13-16, Vancouver 2011.

[8]   M. Zychová et al., "New Research Infrastructure for SCWR in Centrum" Výzkumu Řež, The 6th International Symposium on Supercritical Water-Cooled Reactors, Shenzhen, Guangdong, China, March, 2013.

[9]   T.K. Yeh, M.Y. Wang, H.M. Liu, M. Lee, "Modeling Coolant Chemistry in a Supercritical Water Reactor", Transactions, Topsafe 2012, Safety in Reactor Operations, Helsinki, Finland, Apr 22-26, 2012, 457.

[10]   P. Kritzer, "Corrosion in High-Temperature and Supercritical Water and Aqueous Solutions: a Review", *Journal of Supercritical Fluids*, 29, 2004, 1.

[11]   H. Ohtaki, T. Radnai, T. Yamaguchic, "Structure of Water Under Subcritical And Supercritical Conditions Studied by Solution X-ray Diffraction", *Chemical Society Reviews*, 26, 1997, 41.

[12]   J.C. Wren, J.M. Ball, "LIRIC 3.2 an Updated Model for Iodine Behaviour in the Presence of Organic Impurities", *Radiation Physics and Chemistry,* 60, 2001, 577.

[13]   J.C. Wren, G.A. Glowa, "A Simplified Kinetic Model for the Degradation of 2-Butanone in Aerated Aqueous Solutions under Steady-State Gamma-Radiolysis", *Radiation Physics and Chemistry*, 58, 2000, 341.

[14]   J.M. Joseph, B.S. Choi, P. Yakabuskie, J.C. Wren, "A Combined Experimental and Model Analysis on the Effect of pH and O_2(aq) on γ-radiolytically Produced H_2 and H_2O_2, *Radiation Physics and Chemistry*, 77, 2008, 1009.

[15]   P.A. Yakabuskie, J.M. Joseph, J.C. Wren, "The Effect of Interfacial Mass Transfer on Steady-state Water Radiolysis", *Journal of Radiation Physics and Chemistry*, 79, 2010, 777.

[16]   P.A. Yakabuskie, J.M. Joseph, C.R. Stuart, J.C. Wren "Long-term γ-radiolysis Kinetics of NO_3^- and NO_2^- Solutions", *Journal of Physical Chemistry A,* 115, 2011, 4270.

[17]   O.P. Arkhipov, A.O. Verkhovskaya, S.A. Kabakchi, A.N. Ermakov, "Development and Verification of a Mathematical Model of the Radiolysis of Water Vapor", *Atomic Energy*, 103, 2007, 870.

CHAPTER 2

Technical Background and Literature Reviews

This section provides information on the technology base of supercritical water-cooled reactors. Also, it provides a technical foundation for the study of radiation-induced water chemistry under supercritical conditions.

2.1 Supercritical water-cooled reactor (SCWR)

The SCWR concept is being investigated by 32 organizations in 13 countries and is one of the six reactor technologies selected for further development under the Generation-IV program [1]. SCWRs are based upon two recognized technologies, light water reactors (LWRs) and supercritical fossil-fired boilers that are commonly deployed power-generating technologies in the world. An SCWR is a high-temperature, high-pressure water-cooled reactor that operates with the core coolant at temperatures above the thermodynamic critical point of water (374 °C and 22.1 MPa), Figure 2.1. Operation at pressures above the critical pressure eliminates coolant boiling, so the coolant remains single-phase throughout the coolant circuit. SCWRs are among the most promising advanced nuclear systems because of their high thermal efficiency (about 45% vs. about 35% efficiency for advanced LWRs), considerable plant simplification, and their capability for actinide management (depending on the core design) [2].

The long-term viability of a SCWR will depend on the ability of designers and operators to control and maintain water chemistry conditions that will minimize corrosion

and the transport of both corrosion products and radionuclides. To develop a successful design, engineers must be able to predict corrosion rates. The principal challenge in predicting corrosion and fission product transport is the absence of thermochemical and kinetic data above 300 °C and, most importantly, from 300 °C to 450 °C, where the properties of water change dramatically [3].
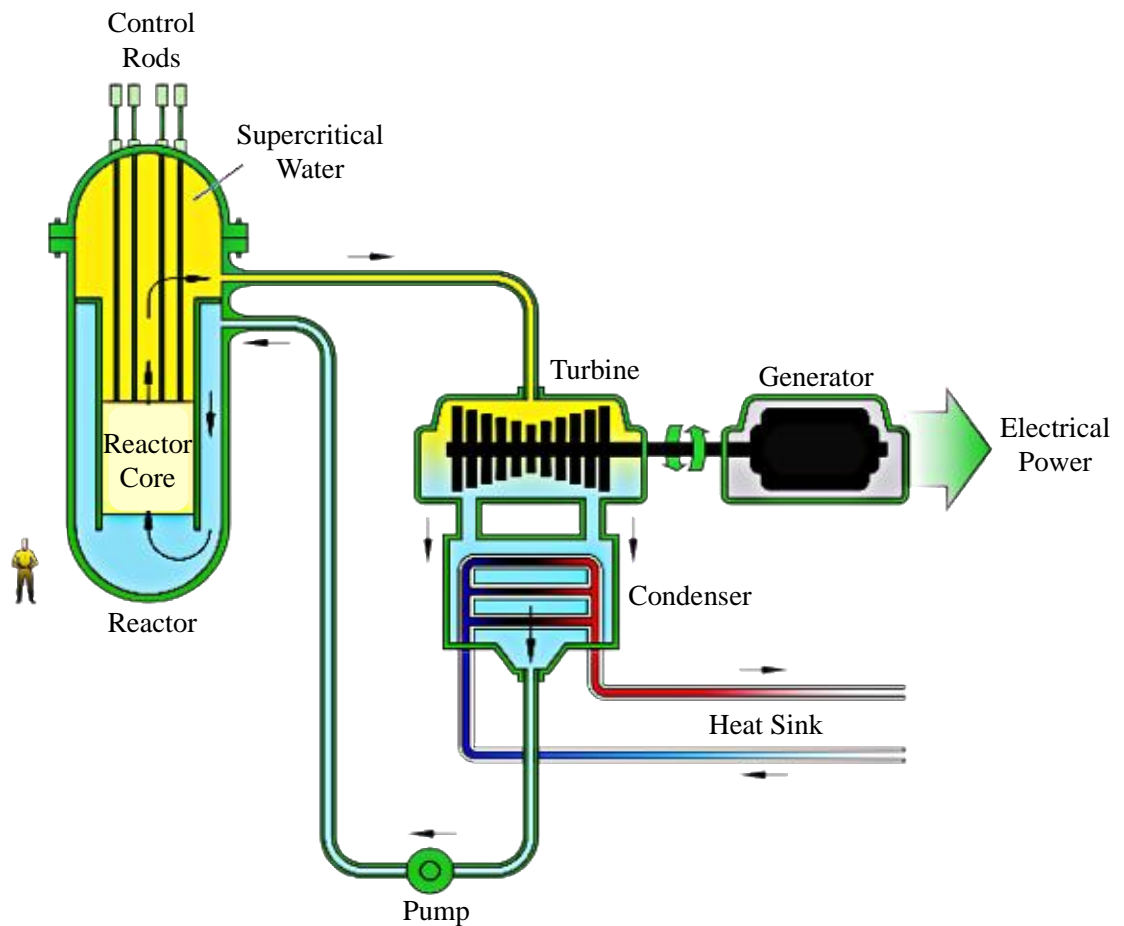
Figure 2.1: Schematic of an SCWR.

2.2   Properties of Sub- and Supercritical Water

Ionizing radiation (present in the reactor core) interacts with matter very differently from low energy radiation. The energy transfer from radiation particle to water molecules, the primary radiolysis and the subsequent chemical reactions are important in determining the net chemical effects induced by ionizing radiation. The relative importance of different processes depends on the type of radiation, and the chemical and solvent properties of water. The physical and chemical processes involved in radiolysis, with a particular focus on γ-radiation, are reviewed in Section 2.3.1.

2.2.1   Supercritical Fluids

Recently supercritical fluids have attracted attention from chemists and engineers because of their peculiar properties. For a pure compound the critical state is the set of conditions at which the distinction between the two phases, liquid and vapour in equilibrium with each other, disappears and there is no phase boundary. Usually the critical temperature (T_C) and pressure (P_C) refer to the point at which the boundary between the gas phase and liquid phase disappears, as shown in Figure 2.2. The state of matter at temperatures and pressures above the critical point is labeled a fluid.
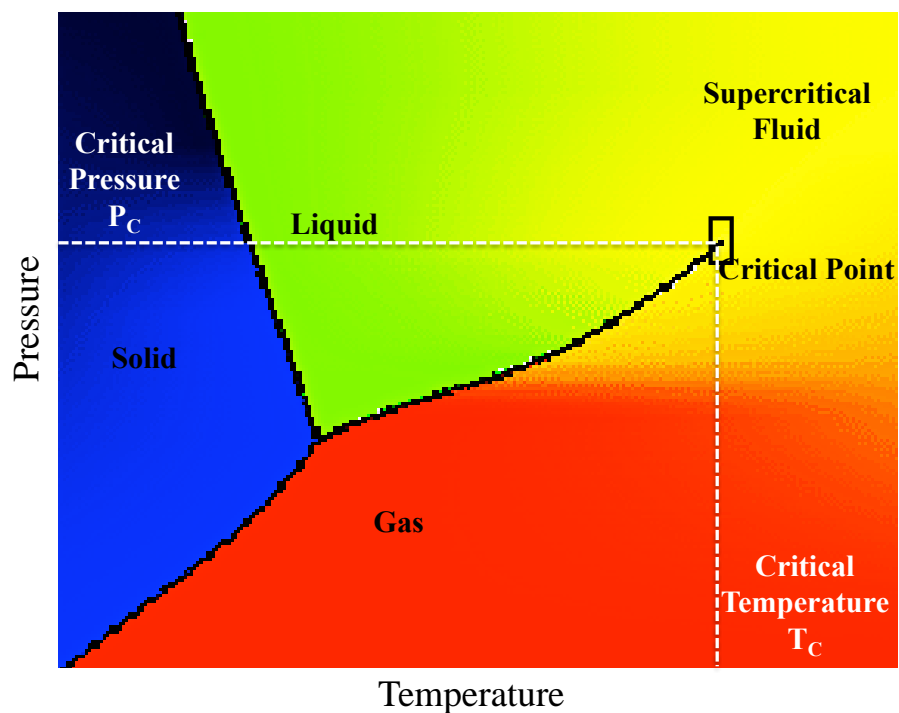
Figure 2.2: Schematic phase diagram.

2.2.2 Supercritical Water

The critical point for water is 374 ºC and 22 MP4. Supercritical water (SCW) possesses extraordinary properties that differ from those of liquid water at normal conditions [4,5]. Due to its high compressibility, its thermodynamics can be modified drastically with small changes in pressure and temperature. It has been shown that reaction rate constants in SCW depend on density [6]. Manipulation of the SCW density can change the relative stabilities of free radicals and ions, and change the dominant reaction mechanisms [7–9]. The following sub-sections examine some of the differences between SCW and normal water.

2.2.2.1   The Extent of Hydrogen Bonding in SCW

Water is an exceptional solvent at ambient conditions. It can form short-ranged, strongly attractive hydrogen bonds and this makes water a challenging fluid to understand [10]. Many of the properties of water depend on its hydrogen bonding and this network of bonds can be strongly affected by temperature and pressure. To study the structure of water and the statistical distribution of water molecules around each other, and to quantify the hydrogen bonding in water at supercritical conditions, a number of different techniques including neutron and X-ray diffraction, microwave, IR, Raman, and proton NMR spectroscopy are used. Also, theoretical and computational studies have greatly improved our knowledge of supercritical water at the molecular level. In principle, simulations by Monte Carlo and molecular dynamic techniques provide a valuable microscopic description of supercritical water, but these simulations are not yet precise enough for large scale applications [11].

Many experiments and model simulations have demonstrated that hydrogen bonds are still present in dense supercritical water although there is a reduction in the number of hydrogen bonds per molecule with respect to ambient conditions (Figure 2.3) [12]. At the critical temperature the energy of the hydrogen bond is still appreciably larger than the thermal energy of the water molecules [13]. However, the extended network structure that is responsible for the unique properties of liquid water is lost. This has an impact on key properties of water as a solvent.

Hydrogen Bonding in Water		
Solid Water	Liquid Water	Gaseous Water
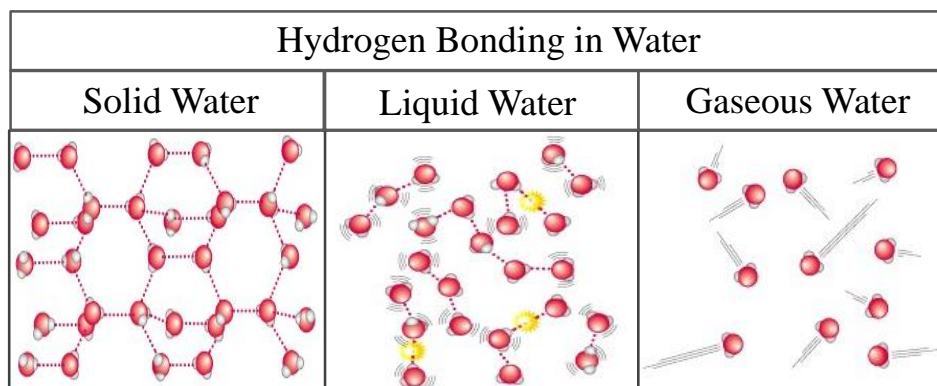
Figure 2.3: Schematic of hydrogen bonding in different states of water (© 2001 Sinauer Associates, Inc.

2.2.3 Ionic Dissociation of SCW

A key property of water is its ability to stabilize ions in solution. A measure of this is the dissociation equilibrium for water, which is characterized by the ionic product (K_w, $mol^2 \cdot dm^{-6}$).

$$H_2O \rightleftharpoons H^+ + OH^- \qquad\qquad K_w^{298} = 1.023 \times 10^{-14} \qquad\qquad (2.1)$$
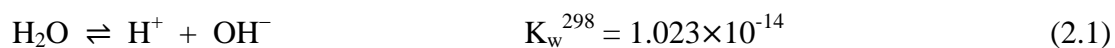
The dependence of the dissociation constant on temperature and pressure (shown as density) is shown in Figure 2.4. The ion product for water increases as the temperature rises and approaches the critical point; it becomes about three orders of magnitude higher than it is for ambient liquid water. However, a sharp decrease in K_w is observed as soon as the critical point is passed [14]. Supercritical water cannot stabilize water ions well and is a poor solvent for ions [8]. However, by increasing the pressure (and density) at a temperature above the critical point, the ability of water to stabilize ions can be increased. As a result SCW conditions can be 'tuned' to benefit ionic or free radical reaction mechanisms [15,16].
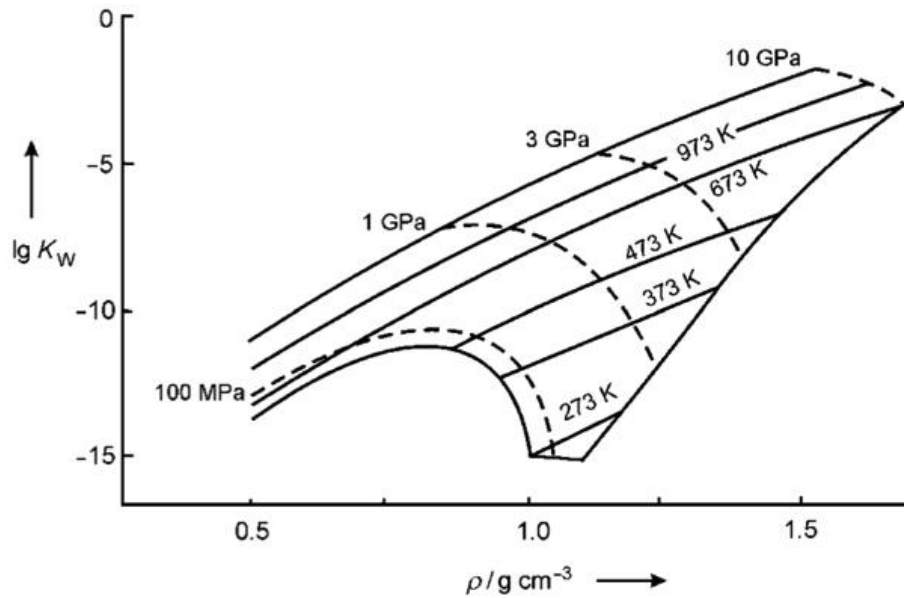
Figure 2.4: K_w of water up to 1273 K and densities up to 1.5 g·cm^{-3} [17] .

2.2.3.1.1 Transport Properties of SCW

Viscosity (η) is important in the analysis of liquid behaviour and fluid motion near solid boundaries. At normal conditions the viscosities of gases and liquids differ by about two orders of magnitude. In principle, a low viscosity is attractive in chemical processes because it reflects high molecular mobilities and facile mass transfer for diffusion-controlled chemical reactions [9,13]. The self-diffusion coefficient of a particle, D, of effective radius r obeys the Stokes–Einstein relation, where k_B is the Boltzmann constant,

$$D = \frac{k_B T}{6\pi\eta r} \tag{2.2}$$

This equation holds for water at temperatures up to the critical point [18]. The factor

$D\eta/T$ is almost constant and this facilitates predictions of solute diffusion rates. In the dilute

gas limit, D is proportional to the ratio of the viscosity and density (η/ρ).

2.2.3.2   Dielectric Properties of SCW

The dielectric constant (ε) is a measure of the polarizability of a material. Liquid

water has a relatively high dielectric constant ($\varepsilon \approx 80$ compared to organic solvents with $\varepsilon <$

10) and this enables it to solvate charged species (ions) readily. The high value of ε at normal

conditions (low temperatures and high densities) results from the strong dipole moment of

the water molecule and its ability to orient the dipole to surround ions within the water

structure [19]. However, as temperature increases, the thermal energy of water molecules

increases and the ability of a water molecule to maintain a particular dipole orientation

decreases. Model calculations [20] and experimental data for water at temperatures and

pressures up to 550 °C and 500 MPa respectively [21,22] show how ε decreases with

increasing temperature and increases with increasing density, Figure 2.5. At low densities

the dielectric constant, and the ability of water to dissolve ionic species decreases quickly.

Supercritical water has a dielectric constant that is on the order of $\varepsilon = 10 - 25$ [13]. These

values are greater than those for non-polar solvents and are high enough to dissolve and

stabilize ions, but are also low enough to make SCW miscible with nonpolar species.
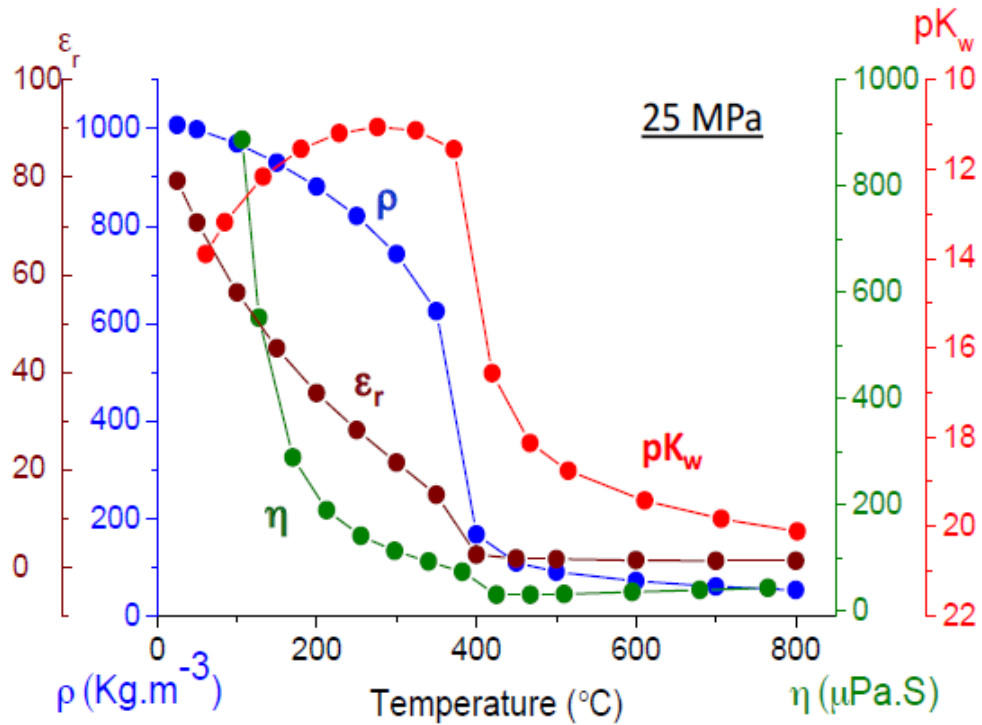
Figure 2.5: Physical properties of water as a function of temperature at 25 MPa.

2.3 Ionizing Radiation in a Nuclear Reactor

In a nuclear reactor, fission of uranium and plutonium isotopes leads to the release of radiation and the creation of fission product fragments, some of which are radioactive isotopes. A radioactive nuclide decays to a stable isotope by emitting a high-energy (fast) $^4He^{2+}$ (referred to as α-particle) or a fast electron (β-particle) with each particle emission accompanied by the emission of one or more high-energy γ photons. The energy of the radiation particle or photon emitted from a radionuclide is characteristic of the nuclide [23]. Each γ photon emitted from a radionuclide has a discrete energy that is characteristic of the

nuclide; the γ-rays emitted during the β-decay of ^{60}Co have energies of 1.332 MeV and 1.173 MeV. The energy of radiation particles and photons range from 0.1 MeV to 5 MeV [23]. This energy is not high enough to induce nuclear reactions but it is high enough to ionize atoms and molecules that are present on its path. Hence these particles and photons are known as ionizing radiation. In a reactor α particles are largely confined within the nuclear fuel and only the behaviour of β particles and γ photons is of interest for water radiolysis.

2.3.1   Radiation - Matter Interaction

2.3.1.1   Energy transfer in water

Ionizing radiation transfers its energy to an interacting medium mainly by colliding non-discriminately with the electrons bound to atoms and molecules in the medium. Due to its high initial kinetic energy each radiation particle undergoes a series of collisions before it loses most of its kinetic energy and becomes thermalized. The difference between β- and γ-radiation lies in the different initial energy transfer mechanism. For β particles the energy is transferred via elastic and inelastic collisions between the fast electron (β) and the bound electrons of the collision partners. For γ-radiation energy transfer is via photon-electron interaction (i.e. elastic and inelastic Compton scattering) [24–26]. The Compton-scattered recoiled electron can have a very high energy and is very much like a β-particle. This is why the chemical effects induced by both β and γ radiation in water (for the same absorbed energy) are essentially the same. The big difference between the two types of radiation is their penetration depth. Because the probability of a Compton scattering event is much lower

than the probability of an electron scattering event, γ photons can, on average, penetrate much further into matter than a β particle before they interact to form a Compton electron.

The main interactions in a radiation particle track are between the fast electron and the electron cloud that surrounds the atoms in a molecule. The larger the density of the bound electrons in the path (or track) of the radiation particle (or the primary electron), the higher the probability of energy transfers collision. The density of the bound electrons in the interacting medium is nearly proportional to the mass density of the medium.

The rate of energy transfer per unit of penetration depth through a medium is referred to as the linear energy transfer (LET) rate. The LET rate is important in determining the density of ions and electronically excited molecules that are formed along the radiation track. Since this density can affect further collision/reactions of species in the track, it will have consequences on the yields of radiolysis products that reach the bulk phase (after diffusing out of the localized zone near the track) where they can undergo bulk chemical reactions. The physical and chemical processes that determine the energy transfer rate, the ionization efficiency, and chemical decomposition yields that follow the energy transfer, are reviewed below.

2.3.1.2   Primary radiolysis processes

Due to their high initial energy, each radiation particle undergoes many collisions while it loses its energy and eventually becomes "thermalized". The multiple interactions are not selective (dependent on the atomic nature of the target matter) and instead depend only

on the relative abundance of electrons in the interacting matter. This is important when irradiating dilute solutions. The total mass of the solutes in such solutions is very much less than the mass of the surrounding water. Hence, the probability of an incident electron interacting with solute impurities is very small compared to the probability of interacting with the bulk water phase. For this reason, chemical processes induced by low LET radiation are often referred to as solvent-oriented processes. The amount of low LET energy absorbed by a solution depends primarily on mass and hence is expressed in units of energy absorbed per mass, the Gray (Gy), where $1 \text{ Gy} = 1 \text{ J·kg}^{-1}$.

The average energy transferred from a radiation particle to a water molecule, per collision, typically ranges from 60 to 100 eV ($1 \text{ eV} \approx 1.6 \times 10^{-19}$ J)[24,27,28]. This amount of energy is a small fraction of the initial radiation particle energy (on the order of 1 MeV), so the collisions neither slow the particle nor change the direction of the radiation path appreciably (except at the very end of the path). The radiation particle moves in a straight line that is designated a radiation track. The initial consequence of each energy transfer collision is ionization or electronic excitation of a water molecule. The result is creation of ion pairs (H_2O^+ and e^-_{hot}) or electronically excited water molecules (H_2O^*) along the radiation track. The electron of this ion pair is labelled as 'hot' because it has a kinetic energy that is sufficiently high to excite or ionize one or more neighbouring water molecules (the 60 - 100 eV transferred in a collision is well in excess of the ionization energy of a water molecule (12.6 eV)) [29]. Secondary (or the tertiary) ionization caused by this 'hot' electron will occur very near the first ionization that created the 'hot' electron, resulting in a cluster of 2-3 ion pairs (or excited water molecules) near the radiation track. This cluster is referred to

as a "spur", see Figure 2.6 [24,27,28]. Any electronically excited water molecules that arise as a result of a hot electron impact have the option of being stabilized (by de-excitation collisions with other water molecules), dissociating into an ion pair (with a low energy electron), or separating into free radical fragments (such as •OH and •H).
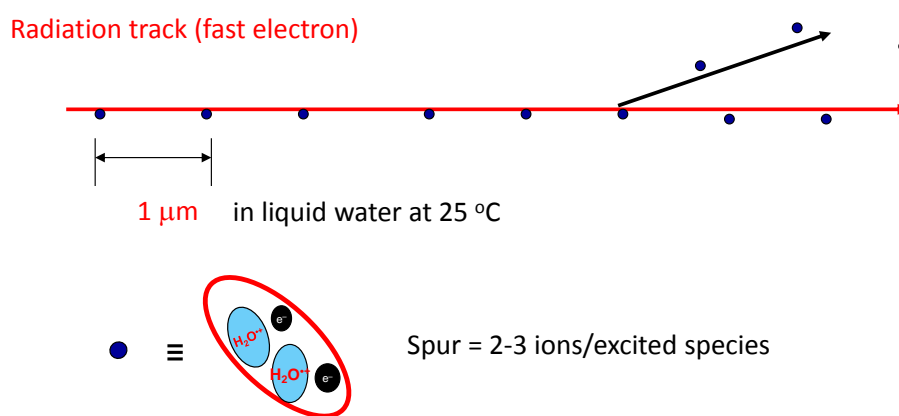
Figure 2.6: The radiation track of a fast electron (spur size not to scale).

The density of spurs along a radiation track is an important parameter in determining the chemical yields of radiolysis products. The spur density depends mainly on the collision rate of the radiation particle with the bound electrons in the water molecules. If the spurs are close enough together, the ions and radicals in a spur can interact with those of an adjacent spur before they diffuse into the bulk water phase. If the spur density is sufficiently high, these interactions can lead to a lower net decomposition rate of water (per absorbed energy unit) and a higher ratio of molecular to radical primary radiolysis products. For the low LET radiation, the inelastic collision mean free path of the radiation (the primary electron) in

liquid water at 25 °C is about 1 μm, while the spur size is about 20 nm (see Figure 2.6) [27,28]. This is not the case for high LET α-radiation, where the spurs overlap considerably. The effect of spur density can be most appreciated by comparing the G-values obtained for high LET α-radiation and those of the low LET γ-radiation (see Table 2.1). The large distance between the spurs for low LET radiation in liquid water means that spur interactions will be even less likely in lower density SCW.

Table 2.1: Primary radiolysis yields* in liquid water at 25 °C [24].

Radiation	H_2O	$\bullet e_{aq}^-$	H^+	$\bullet OH$	$\bullet H$	$\bullet HO_2$	H_2	H_2O_2
γ	− 0.41	0.26	0.26	0.27	0.06	0	0.04	0.07
α	− 0.26	0.02	0.02	0.02	0.01	0.008	0.12	0.11

- The G-values are in units of $\mu mol \cdot J^{-1}$.

The electrons formed in a spur will typically have sufficient kinetic energy to move away from their counter H_2O^+ cations. This process is referred to as expansion of the spur. As the spur is expanding, the 'dry' electrons that arose from the water molecule ionization will be solvated and become hydrated electrons ($\bullet e_{aq}^-$), a well-known species. The water cations and any excited water molecules in the spur will interact with neighbouring water molecules.

2.3.1.3   Dependences of Primary Radiolysis Yields on Water Properties

For a given solvent medium, the yields of the primary radiolysis products (G-values) depend mainly on the amount of energy absorbed by the medium and the chemical nature of the medium. They are nearly independent of the rate of energy absorption for radiation with an energy in the range of 0.1 to 5 MeV [23]. Since the amount of energy absorbed depends primarily on the mass of the solvent, the density of the solvent medium will affect the linear rate of energy transfer (or absorption). However, the primary radiolysis yields per unit absorbed energy are nearly independent of the rate of energy absorption and hence, the primary yields are nearly independent of the density of the medium. The density of the solvent medium also has little impact on the spur density along the radiation track for low LET radiation. Without significant overlap between spurs, the density of the solvent medium alone has very little effect on the chemistry occurring inside the spurs. Consequently, the G-values of steam radiolysis do not vary with temperature or the steam density at low pressures [24].

Water properties that can influence the Coulombic attraction between the ion pairs and radicals and their mobility inside the spurs can have a more significant effect. The influence of these solvent properties on the primary radiolysis yields can be appreciated from a comparison of the G-values for liquid water and water vapour (Table 2.2). The G-values for vapour water are independent of the steam density. The comparison shows that the G-value for water decomposition and the ratio of radical to molecular yields are higher for water

vapour than liquid water. Understanding the reason for this behaviour can provide a technical basis for estimation of G-values for supercritical water.

Table 2.2: Primary γ-radiolysis yields[1] in liquid water and water vapour at 25 °C [30,31].

Water phase	H_2O	$\bullet e_{aq}^-$	H^+	$\bullet OH$	$\bullet H$	H_2	O	H_2O_2
Liquid	− 0.41	0.26	0.26	0.27	0.06	0.04	0.0	0.07
Vapour	− 0.74	0.0	0.0	0.63	0.74	0.05	0.11	0.0

1. G-values in units of $\mu mol \cdot J^{-1}$.

The differences in the G-values for liquid and vapour water arise from other properties of water (such as the dielectric constant, ε_r, the viscosity, η, and the ionic product) and not directly from differences in density. As discussed above, one of the features that controls the yields of primary radiolysis products is interaction within spurs. The probability with which electrons, ions and radicals avoid geminate recombination is related to the rate at which electrons are solvated and/or diffuse away from counter ions. This probability is referred to as the escape probability, P_{esc}, and is determined by:

$$P_{esc} \propto exp\left(-{r_c}/{r}\right) \tag{2.3}$$

where r is the separation distance between an electron and a cation. In this equation, r_c is the Onsager radius, the distance between an electron and its counter ion at which the Coulombic

potential between them equals the average thermal kinetic energy of the particles in the solvent system [32].

$$r_c = \frac{e^2}{4\pi\varepsilon_r\varepsilon_0 k_B T} \tag{2.4}$$

where e is the electron charge, ε_r is the dielectric permittivity of the medium, ε_o is the dielectric constant of permittivity in a vacuum (unitless), k_B is the Boltzmann constant, and T is the temperature (K) ($k_B T$ is the average thermal kinetic energy of a system). This equation shows that the escape probability increases exponentially with the dielectric constant of the solvent medium. As a result the G-values, which are chemical yields, should decrease with decreasing dielectric constant.

The escape probability also increases exponentially with the distance, r, which is the average distance traveled by the electron away from its partner cation before it becomes thermalized. This distance depends on the mobility of the electron (or counter ion) in the solvent medium. The ion or electron mobility, μ, in turn is inversely proportional to the viscosity, η, of the medium [33]. The electron mobility is also very dependent on the extent of solvation. In a low dielectric medium, where the Onsagar radius is large, the speed at which an electron can move beyond the Coulombic attraction range becomes important. Thus, in a low dielectric medium the solvent viscosity that influences the electron mobility becomes a more important parameter than the dielectric constant in determining the G-values. The G-values increase with decreasing viscosity.

The effects of dielectric constant and viscosity can be seen in the different radiolytic yields (G-values) for free ions (equivalent to the G-value of solvent decomposition) observed for different organic solvents, listed in Table 2.3. Comparison of the G-values for water, methanol and benzene, solvents that have similar densities and viscosities but significantly different dielectric constants, shows that a decrease in dielectric constant decreases the G-value. Comparison of benzene, cyclohexane and neopentane, solvents that have similar low dielectric constants but different viscosities, shows that a decrease in viscosity increases the G-value.

Table 2.3: Dielectric constants, viscosities, Onsager radii and free ion yields [33].

Liquid	Density $(kg \cdot m^{-3})$	Viscosity (centipoise)	Dielectric Constant	r_c (nm)	G (free ions) $(\mu mol \cdot J^{-1})$
Neopentane	586	0.007	1.86	32	0.09 – 0.11
Cyclohexane	779	0.297	2.02	28	0.016 – 0.02
Benzene	876.5	0.601	2.27	25	0.005 – 0.008
Methanol	791.80	0.56	32.7	2.3	0.20
Water	1000	0.89	80.1	0.7	0.28

The effect of viscosity on G-values becomes more prominent in a low dielectric medium. The effect of viscosity can be also seen in the difference in the G-values for water decomposition of liquid water and water vapour (listed in Table 2.2). In addition the vapour phase favours radical production over ion production. This is attributed to the difference in

the ionic product, K_W, of the two phases. It can be noted that G-values for irradiation of water vapour are reported to be independent of the steam density, as expected [24].

The data in Table 2.3 clearly demonstrate the importance of the nature of the water phase in determining the primary chemical yields per unit absorbed energy. Since the water solvation properties of SCW are close to those of water vapour, the primary G-values observed for water near critical temperatures may approach those seen for water vapour at room temperature.

In an equilibrium system, the average kinetic energy of a particle is proportional to the absolute temperature ($E_{KE} \propto \frac{1}{2} k_B T$). Hence, an increase in water temperature from 25 °C to 325 °C will only increase the average energy of a particle by a factor of two. This results in only a small change in particle collision energies when compared to the energy required for ionization or electronic state excitation ($E_{KE, 25 °C} = 0.013$ eV vs. 1 - 12 eV). Hence we would not expect to see a significant change in primary radiolysis yields as a function of temperature over this range. Intramolecular energy transfer between different energy states of water cations or electronically excited water molecules is already fast at 25 °C and temperature change alone has no significant effect on ionization efficiency. As well, in liquid water the dipole moment orientation around a thermal electron e^-_{th} and hence the rate of solvation is also fast. Thus, temperature has only a small effect on spur or track chemistry. However, the water temperature can affect the G-values via its influence on the solvation properties of water (dielectric constant, viscosity and ionic product).

The electrons, ions and radicals within a spur continually experience a Coulombic attraction with each other. This can lead to recombination of ions or radicals, thereby reducing the net chemical decomposition caused by absorption of radiation energy. This process is referred to as geminate recombination. When the water decomposition products have moved outside of the range of influence of Coulombic attraction to their counter partners (ions or radicals), it be said the radiation products are out-of-spur and they can be considered as free ions and free radicals.

The Coulombic influence of counter ions diminishes as the spur expands and the counter ions and radicals are no longer distinguishable from other ions and radicals formed in other neighbouring spurs or already present in the bulk phase. Once the system reaches this stage, the subsequent physical and chemical processes of these 'free' species can be treated as ordinary bulk phase chemistry. Figure 2.7 illustrates the time evolution of radiolysis products in a radiation track and spurs.
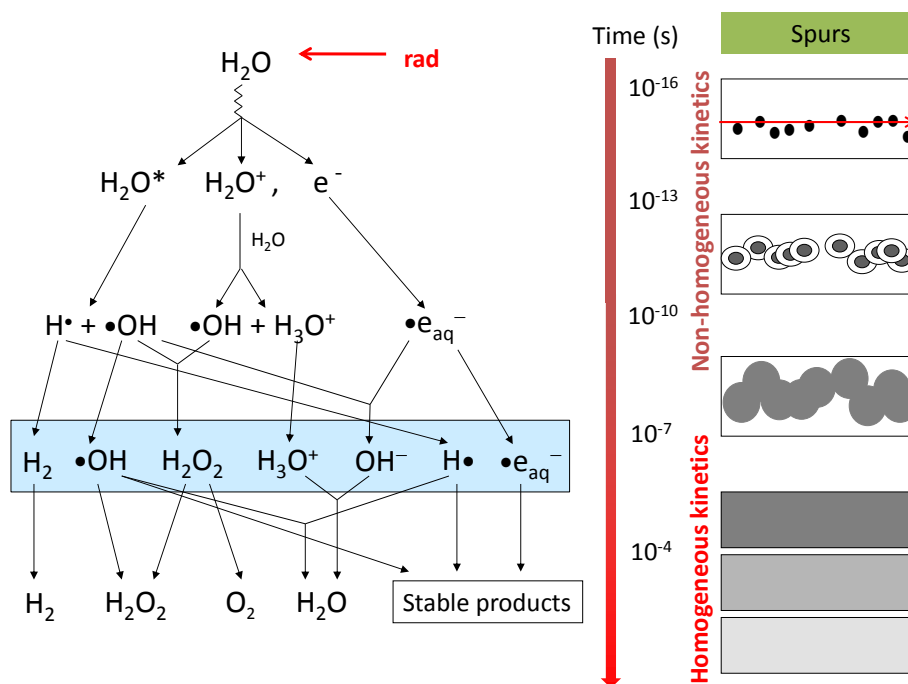
Figure 2.7: Schematic of water radiolysis as a function of time following absorption of radiation energy as a pulse. The right hand panel shows the expansion of spurs with time.

The time frame during which spur expansion occurs is approximately 100 ns in liquid water at 25 °C, Figure 2.7. The species present at the end of this stage (blue box in Figure 2.7) are normally referred to as 'primary' radiolysis products and their concentrations per absorbed energy are primary radiolysis yields. In this sense 'primary' does not refer to the first species created upon interaction of a radiation particle with a water molecule but rather to the starting point for the chemical evolution of an irradiated system.

2.3.1.4   Aqueous Reactions of Radiolysis Products

After primary radiolysis products are formed and have migrated into the bulk phase, they will undergo homogeneous chemical reactions. These will include reactions with other water radiolysis products, water molecules, water dissociation ions (H^+ and OH^-), and any solute species that may be present (such as O_2 from air in contact with the water, or dissolved metal ions). These reactions can be described very effectively using simple, classical rate equations. Nevertheless, the chemical kinetics is complex because, even for a simple system containing only water (H and O), there are a surprisingly large number of species (molecules, ions and radicals) present. They require a quite large set of closely coupled reactions to model the chemical system (as schematically shown in Figure 2.8). About 50 elementary reactions are required to describe the radiolysis kinetics of a pure water system.

With a continuous, steady state radiation flux, water molecules are continuously interacting with radiation particles to form primary radiolysis products. After the start of irradiation, the concentrations of water radiolysis products increase rapidly. However these species also rapidly begin to react with each other and other species in the system and the chemical system reaches a pseudo-steady-state on a time scale that is on the order of minutes (quite long in comparison to the time scale in which primary radiolysis products are formed (~ 1 μs after deposition of a particle's energy)). It is the pseudo-steady-state concentrations of reactive species and not the primary radiolytic yields of reactive species that are crucial in evaluating the effects of irradiation on corrosion. In reaching steady state the back reactions of acid-base equilibria become important and some cyclic (autocatalytic) reaction sequences

can be established. The steady-state concentrations of reactive species arising from radiolysis cannot be easily predicted by a simple assessment of individual reactions and their reaction rates [27]. However, the complex reaction kinetics can be followed through the use of a computer program that solves the problem of the set of coupled stiff differential equations that describe the individual reactions. To perform this modelling analysis, a set of rate constants for the individual reactions is required. These are well established for water up to 200 °C.
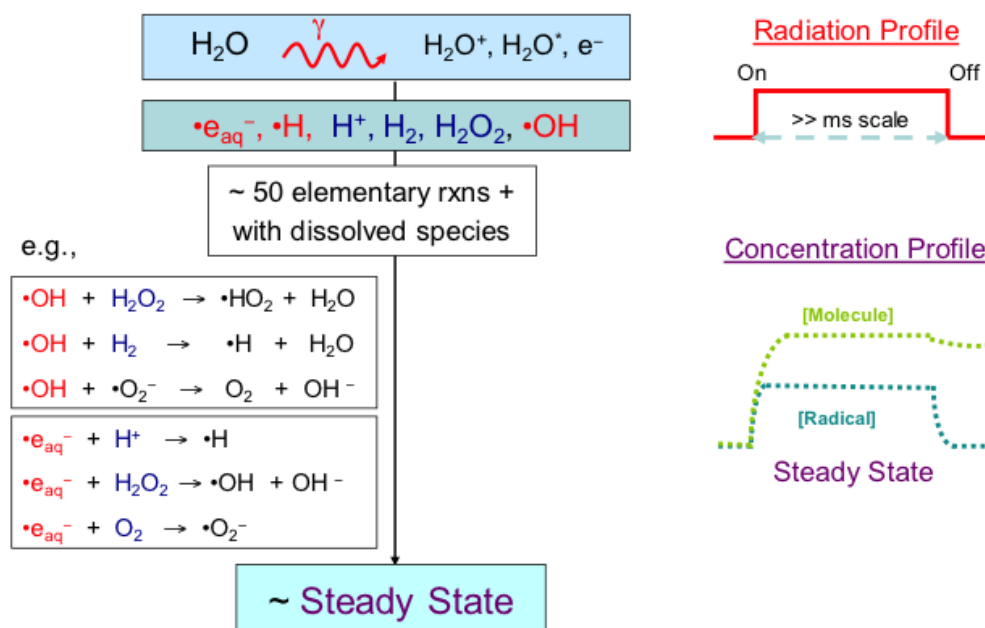
Figure 2.8: Schematic of water reactions under long-term (> ms) continuous irradiation.

The rate constants for most chemical reactions in supercritical water are not available. However, the rate constants for reactions in liquid water and vapour water at high temperatures below the critical point are reasonably well established [31]. For chemical reactions with an activation energy associated with it, the rate constants generally have Arrhenius temperature dependence at ambient temperatures. This makes it possible to extrapolate rate constants to high temperatures. However, at high temperatures the reactant collision rate or diffusion rate can contribute significantly to rate determining step [34–37]. These mass transport processes strongly depend on the water density and the properties of water as a solvent. This means that in raising temperatures above the critical point extrapolation of the rate constants for the reactions in supercritical water requires that the effects of solvent properties (such as ionic product, viscosity, diffusivity and dielectric constant) must be taken into account.

2.4   References

[1]   "A Technology Roadmap for Generation IV Nuclear Energy Systems", U.S. DOE Nuclear Energy research Advisory Committee and the Generation IV International Forum, publisher, Dec. 2002.

[2]   P.E. Macdonald, "Supercritical Water Reactor", INEEL/EXT-03-01210, US, 2003.

[3]   D.A. Guzonas, F. Brosseau, P. Tremaine, J. Meesungnoen, "Water Chemistry in a Supercritical Water-Cooled Pressure Tube Reactor", *Journal of Nuclear Technology*, 179, 2012, 205.

[4]   C.W. Kern, M. Karplus, F. Franks, "In Water: a Comprehensive Treatise", Plenum Press, New York, 1972.

[5]   T.J. Bruno, J.F. Ely, "Supercritical Fluid Technology", 3rd ed., CRC Press, Boca Raton, 1991.

[6]   J. Cline, K. Takahashi, T.W. Marin, C.D. Jonah, D.M. Bartels, "Pulse Radiolysis of Supercritical Water. 1. Reactions Between Hydrophobic and Anionic Species", *Journal of Physical Chemistry A,* 106, 2002, 12260.

[7]   M. Watanabe, T. Sato, H. Inomata, R.L. Smith, K. Arai, A. Kruse, E. Dinjus,

"Chemical Reactions of C_1 Compounds in Near-Critical and Supercritical Water", *Chemical Reviews,* 104, 2004, 5803.

[8]   P.E. Savage, "Organic Chemical Reactions in Supercritical Water", *Chemical Reviews*, 99, 1999, 603.

[9]   N. Akiya, P.E. Savage, "Roles of Water for Chemical Reactions in High-Temperature Water", *Chemical Reviews*, 102, 2002, 2725.

[10]   F.H. Stillinger, "Water Revisited", *Science*, 209, 1980, 451.

[11]   B.D. Bursulaya, H.J. Kim, "Molecular Dynamics Simulation Study of Water Near Critical Conditions. II. Dynamics and Spectroscopy", *The Journal of Chemical Physics,* 110, 1999, 9656.

[12]   M.C. Bellissent-Funel, J.C. Dore, "Hydrogen Bond Networks", Springer Netherlands, Dordrecht, 1994.

[13]   H. Weingärtner, E.U. Franck, "Supercritical Water as a Solvent", *Angewandte Chemie Journal*, 44, 2005, 2672.

[14]   J.H. Park, S.D. Park, "Kinetics of Cellobiose Decomposition Under Subcritical and Supercritical Water in Continuous Flow System", *Korean Jornal of Chemical Engineering,* 19, 2002, 960.

[15]   A. Loppinet-Serani, "Supercritical Water for Environmental Technologies", *Journal of Chemical Technology and Biotechnology*, 85, 2010, 583.

[16]   W. Wahyudiono, S. Machmudah, M. Goto, "Utilization of Sub and Supercritical Water Reactions in Resource Recovery of Biomass Wastes", *Engineering Journal*, 17, 2013, 1.

[17]   W.L. Marshall, E.U. Franck, " Ion Product of Water Substance, 0–1000 °C, 1–10,000 bars, New International Formulation and its Background", *Journal of Physical Chemistry Reference Data*, 10, 1981, 295.

[18]   W.J. Lamb, "Self-diffusion in Compressed Supercritical Water", *Journal of Physical Chemistry*, 74, 1981, 6875.

[19]   J.G. Kirkwood, "The Dielectric Polarization of Polar Liquids", *Journal of Physical Chemistry,* 7, 1939, 911.

[20]   E.U. Franck, S. Rosenzweig, M. Christoforakos, "Calculation of the Dielectric Constant of Water to 1000 °C and Very High Pressures", *Berichte Der Bunsengesellschaft Für Physikalische Chemie,* 94, 1990, 199.

[21]   K. Heger, M. Uematsu, E.U. Franck, "The Static Dielectric Constant of Water at High Pressures and Temperatures to 500 MPa and 550 °C", *Berichte Der Bunsengesellschaft Für Physikalische Chemie*, 84, 1980, 758.

[22]   R. Deul, E.U. Franck, "The Static Dielectric Constant of the Water-Benzene Mixture System to 400 °C and 2800 bar", *Berichte Der Bunsengesellschaft Für Physikalische Chemie,* 95, 1991, 847.

[23]   CRC Handbook of Radiation Chemistry, CRC Press, 1991.

[24]   J.W.T. Spinks, R.J. Woods, "An Introduction to Radiation Chemistry", 3rd ed., Wiley-Interscience, New York, 1990.

[25]   J.H. O'Donnell, D.F. Sangster "Principles of Radiation Chemistry", Elsevier, New York, 1970.

[26] Z.D. Draganić, I.G. Draganić, "The Radiation Chemistry of Water", Academic Press, New York, 1971.

[27] J.C. Wren, "Steady-State Radiolysis: Effects of Dissolved Additives", ACS symposium series, in: Nuclear Energy and The Environment, American Chemical Society, Washington, D.C, 2010, 271.

[28] G.V. Buxton, "Radiation Chemistry", EDP Sciences, France, 2008.

[29] L. Wojnarovits., "Radio Chemistry and Nuclear Chemistry", Kluwer Academic Publishers, Amsterdam, 2003 (e-Book).

[30] A.J. Elliot, D.M. Bartel, AECL Report-11073, Chalk River, Canada, 2009.

[31] O.P. Arkhipov et al., "Development and Verification of a Mathematical Model of the Radiolysis of Water Vapor", *Atomic Energy*, 103, 2007, 870.

[32] J.F. Wishart, "Photochemistry and Radiation Chemistry: a Perspective", American Chemical Society, Washington, 1998.

[33] G.R. Choppin, J.O. Liljenzin, J. Rydberg, "Radiochemistry and Nuclearchemistry", 3rd ed., Elsevier, New York, 2002.

[34] D. Swiatla-Wojcik, G. V. Buxton, "Modeling of Radiation Spur Processes in Water at Temperatures up to 300 degree", *Journal of Physical Chemistry*, 99, 1995, 11464.

[35] G.V. Buxton, "Radiation Chemistry. Present Status and Future Trends", Elsevier, Amsterdam, 2001.

[36] A.J. Elliot et al., "Estimation of Rate Constants for Near-Diffusion-Controlled Reactions in Water at High Temperatures", *Journal of the Chemical Society, Faraday Transactions*, 86, 1990, 1539.

[37] D. Swiatla-Wojcik, G.V. Buxton, "On the Possible Role of the Reaction H$\bullet$ + H$_2$O $\rightarrow$H$_2$ + $\bullet$OH in the Radiolysis of Water at High Temperatures", *Radiation Physics and Chemistry*, 74, 2005, 210.

CHAPTER 3

Experimental Principles and Details

The experiments performed for this thesis involved the irradiation of water samples using a high flux gamma cell. In this chapter, information regarding the experimental equipment, the experimental procedure and analytical techniques that were used is provided.

3.1   Solution preparation

All experimental solutions were prepared daily using water from a NANOpure Diamond UV system from Barnstead International, with a resistivity of 18.2 MΩ.cm in order to eliminate organic and inorganic impurities in the water. The experiments were performed at pHs of 7.0 and 10.6. The pH was adjusted to 10.6 by dropwise addition of 1 M sodium hydroxide for room temperature studies and of 10^{-3} M lithium hydroxide for higher temperatures studies. The solution pH was measured both before and after an irradiation test using an electronic pH meter (Accumet) that was calibrated with reference solutions.

3.2   Aeration

After pH adjustment, solutions were deaerated. The deaerated solutions were prepared by purging with ultra high purity argon (Praxair, impurity 0.001%) for one hour. The bulk solution was then transferred into an argon-filled glove box and consequently into radiolysis cells. The oxygen concentration in the glove box was kept below a 1000 ppm

threshold for O_2, as verified by gas chromatographic analysis of the glove box air composition.

3.3   Gold Plating of Radiolysis Cell

A major focus of this research was the study of water radiolysis at supercritical water conditions. At these very high temperatures, reactions of water and water radiolysis products with metallic cell wall materials can be accelerated [1]. It is necessary to use metal alloys for the cell walls to obtain the strength required at the test temperatures and pressures. Hence much of the effort in this thesis was devoted to the development and testing of an appropriate test cell.

Stainless steel was the material of choice for a radiolysis cell because of its strength and relatively low corrosion rate. However, even low corrosion rate is enough to influence the concentrations of radiolysis products at high temperatures, so gold plating was applied to the inner cell surfaces. Gold was used because it is known to be very inert to both oxidizing and reducing reactions of water and water radicals, even at high temperatures.

The gold plating was applied using an electroplating method. Electro-deposition of an adherent metallic coating upon a metal electrode for the purpose of securing a surface with properties or dimensions different from those of the base metal is defined as electroplating. The physical embodiment of an electroplating process consists of four parts: (1) the external circuit, (2) a negative electrode or cathode (material to be plated), (3) the plating solution,

containing a compound of the metal to be deposited, and (4) a positive electrode, a conducting material that serves solely to complete the circuit [2].

The material to be plated is immersed in the plating solution (the bath) containing the plating metal in an oxidized form. The metal in solution migrates toward the negatively charged cathode. Once the metallic ion has reached the cathode it is reduced and is deposited as a neutral metal atom onto the element being plated (Figure 3.1). The amount of metal deposited is a product of time, the total current flowing through the solution, and the bath efficiency, also called the cathode efficiency. Faraday's laws of electrolysis govern the amount of metal deposited; for each Faraday of electricity that flows through the cathode, one mole of metal will be deposited on the cathode.

Gold plating of stainless steel in our laboratory was done using a 24K (karat) Bright gold plating solution supplied by Gold Plating Services. The solution contains 25 grams fine gold per litre and a small amount of cobalt, and the solution is acidic. Gold plating using a Bright solution yields a relatively low stress, fine-grained deposit of gold with a hardness in the range of 130-200 Knoop. This solution produces 99.7% purity hardened gold plating.

We performed the plating in two sequential steps to obtain a gold coating with a finer grain. The first step was the deposition of an initial layer of gold. This step started with immersion the stainless steel part in the Bright solution and stripping the existing chromium oxide from the surface by acid in the solution. Based on the recommended procedure for plating with this solution, the temperature was increased to 38 ℃ with continuous stirring. The required current was calculated using the surface area of stainless steel part. A current

density of 64.6 amp/m^2 will result in the deposition of a 1micron thick layer of gold in 8 min. In the next step in order to make the gold layer thicker and compact, a current density of 32.3 A/m^2 for 13 min was applied to deposit 2.5 microns of gold. The temperature of the solution at this stage was increased to 55 ℃ based on the recommended procedure.
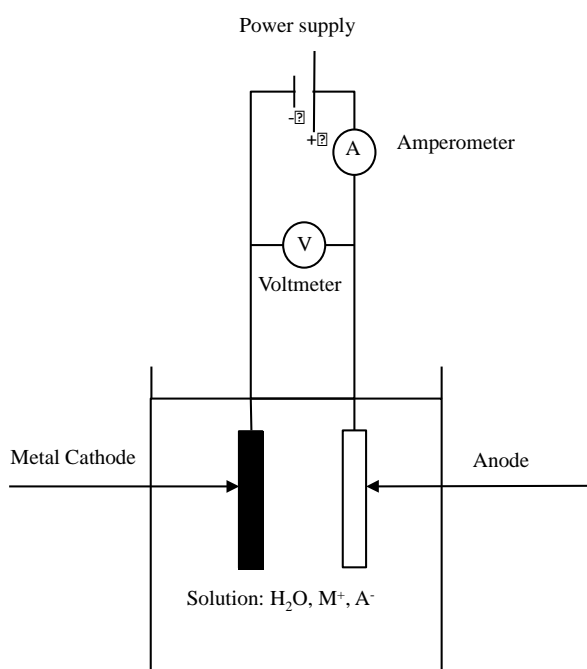
Figure 3.1: Schematic of an electroplating setup.

3.4   Sealing

The radiolysis cells were designed to minimize the leakage of the gasses formed inside the cell or any air ingress during sampling. Based on the radiolysis cell design and experimental conditions (pressure and temperature) different sealing strategies were chosen.

A proven quartz cell design was used for tests up to 150 °C. At these low temperatures and pressures, a metal cell was not necessary. For the quartz cell a PTFE (polytetrafluoroethylene) silicon septum was used to seal the cap (Figure 3.2). For the gold-plated stainless steel cell, a piece of gold foil, which completely covered the surface area of the opening, was placed on top of the cell opening. A cell closure before adding the screw on gold-plated cell closure (Figure 3.3 - note the flats on the sides of the top for wrench mating). An additional PTFE silicon septum is placed over the stainless steel cell during sampling, see Figure 3.4.
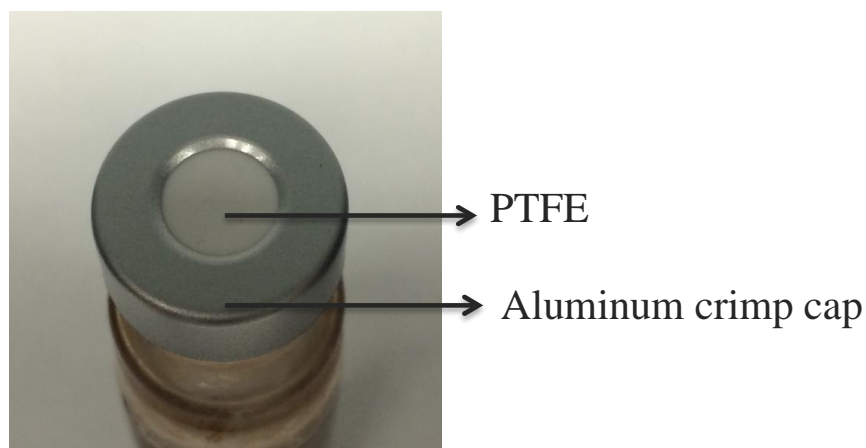
Figure 3.2: Quartz cell cap with PTFE silicon septum.

Gold foil on top

Figure 3.3: Gold-plated stainless steel cell cap showing gold foil in the center.

PTFE silicon septum

Figure 3.4: PTFE silicon septum placed over the stainless steel cell during sampling.

3.5   Pressure and Temperature Control

For high temperature tests, the radiolysis test cells and vials were placed inside an autoclave (pressure vessel) with an external electrical heating coil (Figure 3.5). The temperature inside the autoclave was monitored with a Type J thermocouple (iron constantan, supplied by Parr Instrument Company) that is well suited to the operating temperature range of the autoclave. The autoclave, which was a N4760 model pressure vessel supplied by Parr Instruments, had a 300-ml volume (6.5-cm inside diameter, 10-cm inside depth) and a 4-kg weight. The maximum pressure and temperature that this autoclave can withstand are respectively, 350 °C and 20 MPa. The cross-section of the autoclave and the assembled autoclave with plug and rupture disc are illustrated in Figures 3.6 and 3.7.
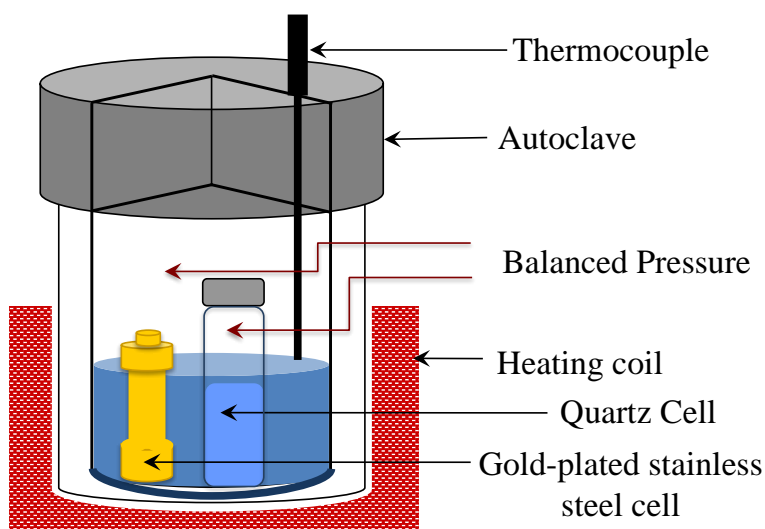
Figure 3.5: Schematic of an autoclave containing radiolysis cells.
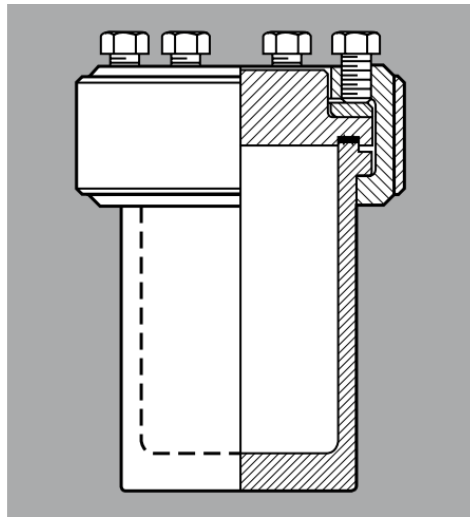
Figure 3.6: Schematic of the autoclave's cross-section.

Figure 3.7: Assembled autoclave with plug and rupture disc.

In a test, power was supplied to the heating coil with a variable power supply set a desired voltage that was based on experience. This caused the temperature inside the cell to rise to the desired temperature after it was placed inside the gamma cell. It required approximately 30 min to reach 150 °C and 45 min to reach 250 °C. To maintain a pressure balance on the inside and outside of the radiolysis cells, the cells were placed in water in the autoclave. The ratio of water to gas volume in both the cells and autoclave were approximately the same (1:2). At the end of an experiment, the heating coil power was shut off and the autoclave was removed from the gamma cell. It took approximately 40 min for the temperature of the autoclave to decrease to a level at which it could be easily handled and disassembled for removal of the test cells.

3.6 γ- Irradiation

Our experiments involved the γ-irradiation of small samples of water. The irradiation source was an industrial gamma cell irradiator, MDS Nordion model 220 (Figure 3.8). This gamma cell contains ^{60}Co doubly encapsulated in aluminum and stainless steel tubes (Figure 3.9), and fixed within a lead shield to supply the γ-radiation (1.33 and 1.13 MeV γ-rays). The gamma cell exposure chamber has a cylindrical geometry, 20.3 cm high and 7.5 cm in radius [3].

The exposure chamber is accessed by a vertical lift in the center of the gamma cell. Experimental samples were encased in an autoclave that is sized to fit the exposure chamber. The autoclave is positioned on the top of a lift and then lowered into the gamma cell to start

the irradiation. When the desired period of irradiation was complete, the autoclave was removed from the exposure chamber.

Figure 3.8: Nordion Gamma Cell 220.

Source Cage

Double encapsulated sources in position
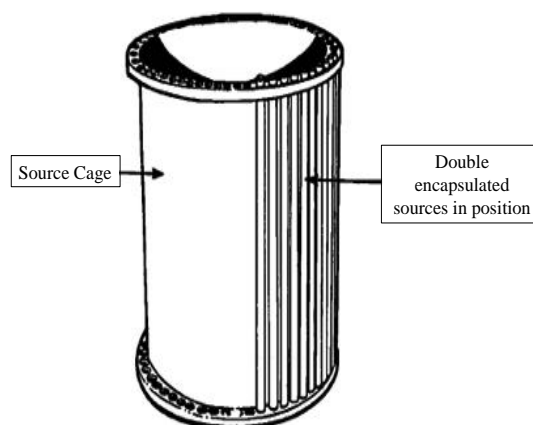
Figure 3.9: Arrangement of ^{60}Co source tubes in the gamma cell.

A typical absorbed dose distribution within the gamma cell exposure chamber is illustrated in Figure 3.10 [3,4]. The dose is relatively uniform over the central volume of the exposure chamber where our test samples were located. This justifies the use of a single value for the absorbed dose rate in our experimental analyses. The dose rate of the gamma cell that was used, was determined using Fricke dosimetry [4,5]. Fricke dosimetry uses an aqueous solution of sulfuric acid and ferrous sulfate in the following composition: 1 mM $FeSO_4$ + 0.8 N H_2SO_4 + 1 mM NaCl. Irradiation of the Fricke solution causes radiolysis of water and the radiolysis product H_2O_2 oxidizes the ferrous ions to ferric ions. The ferric ions have a strong optical absorption coefficient with peaks at wavelengths 224 nm and 304 nm [6], and the concentration of the ferric ions that are produced during an irradiation period is determined by UV-visible spectrophotometry of the solution. The dose rate is then calculated using the known G-value for the production of H_2O_2 by water radiolysis.

The gamma source is ^{60}Co which has a half-life of 5.27 a, hence, the dose rate within the gamma cell appreciably decreases within the time scale of these studies. Fricke dosimetry measurements were carried out by members of the research team using the cell periodically to confirm the dose rate as a function of time. During the period in which the experiments documented in this thesis were performed, the dose rate varied from 4.5 kGy·h^{-1} to 4 kGy·h^{-1}.
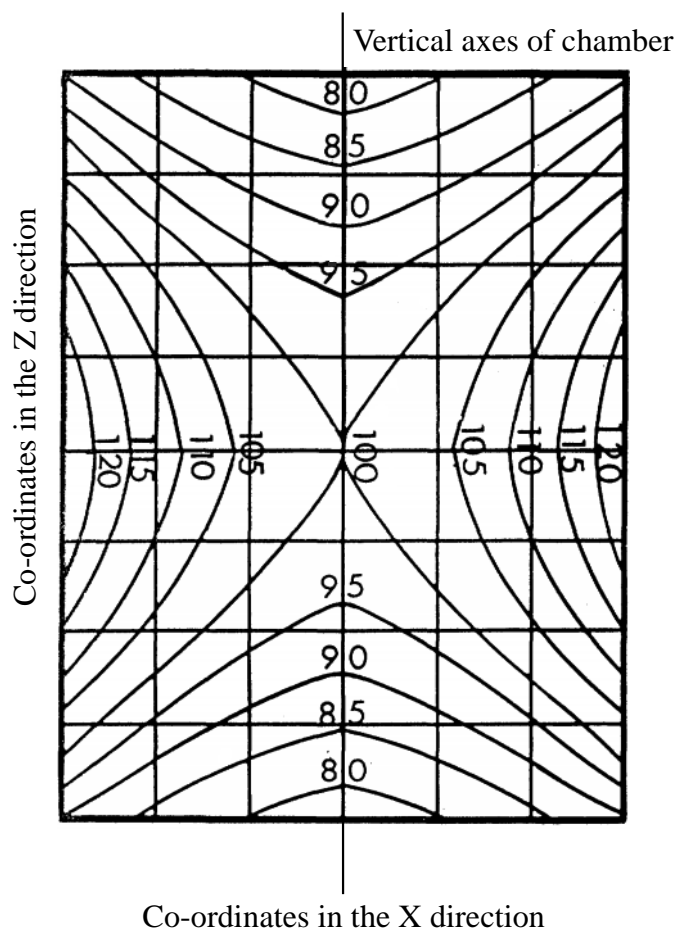
Figure 3.10: A typical isodose curves for a vertical cross sectional plane through the central axis of a gamma cell.

3.7   Sample Analysis

Upon the termination of irradiation the autoclave is taken out of the gamma irradiator. The radiolysis cell is allowed to cool down to around room temperature and then analyses of the aqueous and gaseous phases were performed.

3.7.1   Gas Chromatography

The H_2 and O_2 concentrations in the headspace of a radiolysis cell were determined using gas chromatography. A gas sample was extracted from the radiolysis cell headspace using a gas-tight syringe with a Luer lock (Agilent Technologies) and injected into a GC system (GC-MS, 6580 Agilent Technologies) through a gas-tight septum.

Gas chromatography is an analytical technique used for the separation, identification and quantitative determination of volatile compounds. In gas chromatography, separation of the components is achieved by their distribution between two phases. One is a stationary phase with large surface area and the other is a mobile phase (gas) that is in contact with the stationary phase [7]. A normal gas chromatograph has the solid phase on the walls of a small diameter column and the mobile phase moves through the column (Figure 3.11). Due to differential partitioning between the mobile phase and the stationary phase on the walls of the column, the components of the gas phase are separated in time. Transport of the gas to be analyzed through the column is achieved by the flow of an inert carrier gas [8].

We used a gas chromatograph with a 60-m long GS-GASPRO column (diameter 0.32 μm) connected to a micro-fluid three-way splitter to allow simultaneous analysis by different detectors.
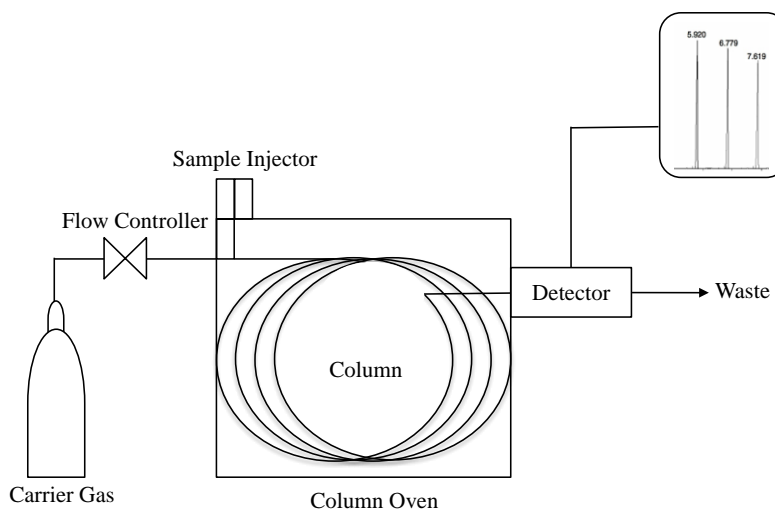
Figure 3.11: Schematic of gas chromatography.

A variety of detectors are available for use with the gas chromatograph column. The detectors use some physical or chemical property of the vapours that are to be identified. The H_2 concentration was determined using a thermal conductivity detector (TCD) [9]. The TCD compares the thermal conductivities of two gas flows, carrier gas that bypasses the separation column (reference) and carrier gas that has passed through the column (column effluent).

The sensitivity for a compound increases when there is a larger difference in thermal conductivities of the carrier gas and that particular compound. Typically, helium is used as the carrier gas because of the large difference in thermal conductivity of He compared to most compounds. But, because the thermal conductivities of He and H_2 are close, a TCD is not very sensitive to H_2 when using a helium carrier gas. Therefore, for hydrogen analysis with a thermal conductivity detector, argon is the recommended carrier gas. Another alternative for the carrier gas is N_2, which we have used for our detection.

The thermal conductivity detector holds a filament that is heated electrically. The filament temperature is kept constant while alternate streams of carrier gas and column effluent pass over it (Figure 3.12). When there is another component in the effluent gas, the thermal conductivity of the gas is different and power required keep the filament temperature constant changes. The power differences are measured and recorded and the output of a TCD is a number spikes for these differences as a function of time after the sample was introduced into the column (Figure 3.13). The elution times correspond to the different volatile components of the sample. Elution times are not uniquely associated with a particular species and the GC must be calibrated with known gas samples to identify a particular species. The TCD detector in our lab was calibrated by injecting certified gas mixtures with concentrations of 0.1%, 1%, 3% and 5% hydrogen gas in helium supplied by Praxair. The area under the curve of a GC spike can be related to the quantity of the species in the original sample.
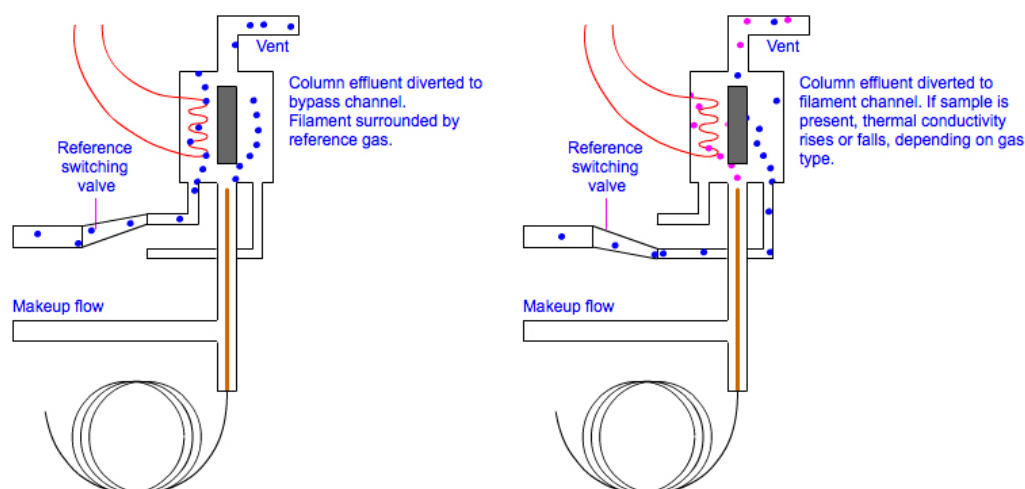
Figure 3.12: TCD - conceptual diagram.
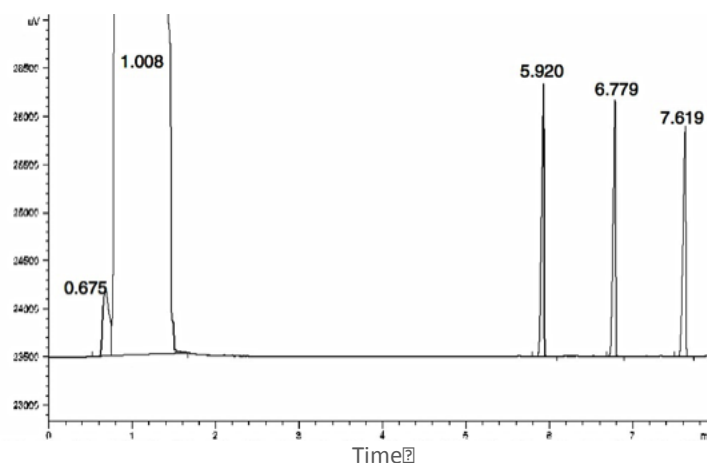
Figure 3.13: Typical TCD chromatogram.

The detector used for O_2 in the gas chromatography was micro cell electron capture detector (μ-ECD). This type of detector is commonly used for components with high electronegativity. It contains a cell plated with ^{63}Ni, a radioactive isotope. The ^{63}Ni releases β particles that collide with carrier gas molecules to produce low-energy electrons. The free electrons produce a small current (reference or standing current) that is measured by applying a pulsed voltage across the flow path through the cell (Figure 3.14).

When a sample component molecule comes into contact with the free electrons, they may capture an electron. The result heavy ions are not deflected by the applied cell voltage and are swept out of the cell vent with the carrier gas. This results in a change in the current across the cell electrodes compared to a reference current. The pulse rate is adjusted to maintain a constant cell current. The fewer the number of electrons that are captured, the lower the pulse frequency that is required to match the reference current. When a compound that captures electrons passes through the cell, the pulse rate rises. This pulse rate is

converted to a voltage and recorded [10]. The calibration of the µ-ECD was carried out by injecting gas mixtures of 2%, 5%, 10% and 35% oxygen in argon, supplied by Praxair.
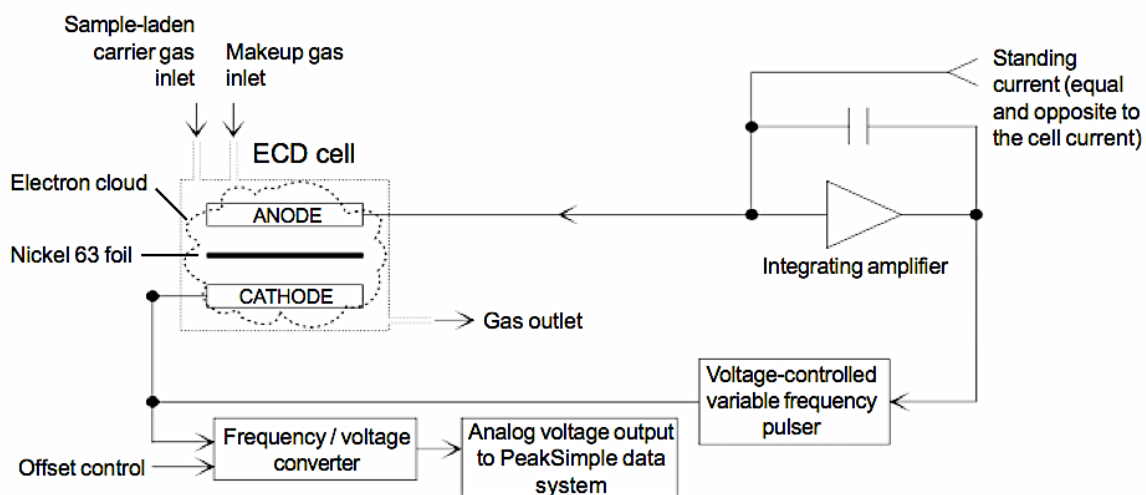
Figure 3.14: Micro-cell electron capture detector operational diagram.
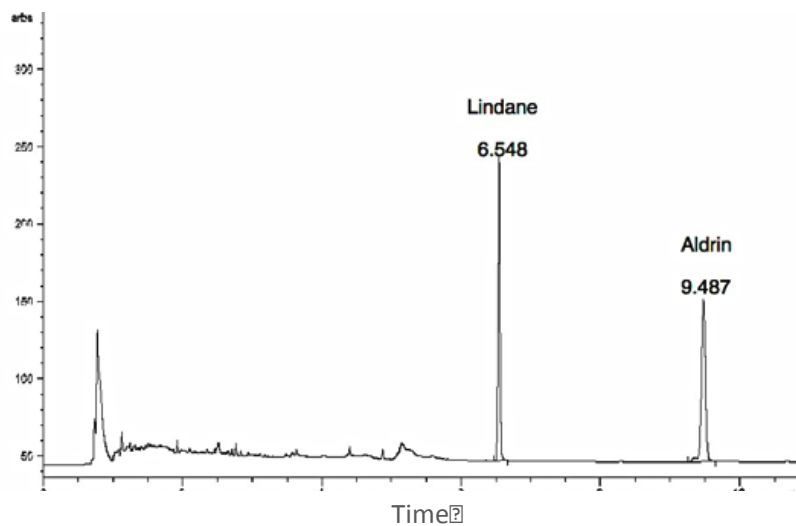
Figure 3.15: Typical µ-ECD chromatogram.

3.7.2 UV-Visible Spectrophotometry

The aqueous phase was analyzed using UV spectrophotometry to detect the presence of hydrogen peroxide. The hydrogen peroxide analysis was performed as soon as possible after the termination of irradiation in order to minimize any thermal decomposition of hydrogen peroxide in the radiolysis cell. In our tests the time interval was usually approximately 30 minutes.

UV-Visible spectrophotometry has been used widely for the quantitative determination of substances. The criterion for the analysis of a compound by this method is that the compound or its derivatives should obey Beer's law (3.1) in the range of concentrations to be measured [11].

$$log\left(\frac{I_0}{I}\right) = A = \varepsilon \ell c \tag{3.1}$$

where I_0 is the intensity of the incident light, I is the intensity of emergent light, A is the absorbance, ε is the absorptivity of the target compound at the incident light frequency, ℓ is the cell light path-length, and c is the concentration of the absorbing species. In some cases where the absorbance is not proportional to concentration, i.e. when Beer's law is invalid, analysis by spectrophotometry is still possible but it requires the use of a calibration curve.

The concentration of a particular absorbing compound in a mixture is easily determined if a wavelength can be chosen at which the desired compound is the only absorbing species. In this case the absorbance of the mixture, A_m, is compared with the absorbance, A_0, of the target compound at a known concentration, c_0, at the characteristic

absorption wavelength and the concentration of the target compound in the mixture, c_m, can readily be calculated [12].

All spectrophotometric measurements were performed using a diode array UV spectrophotometer (BioLogic Science Instruments). A diode array is an assembly of individual detector elements in linear or matrix form that, in a spectrophotometer, can be mounted so that the complete spectrum is focused on an array of appropriate size. No wavelength change mechanism is required and output presentation is virtually instantaneous. Diode array instruments typically are less complex and have fewer optical surfaces than conventional ones. As a result, light throughput is higher and noise levels are lower.

The concentrations of hydrogen peroxide in aqueous samples were determined using the Ghormley tri-iodide method [13,14]. An iodide reagent was prepared immediately before using by mixing 2.5 ml of two solutions containing: (a) 5 g potassium hydrogen phthalate in 250 ml of water and (b) 0.5 g NaOH, 0.05 g $(NH_4)_6 Mo_7O_{24}.4H_2O$, and 16.5 g KI in 250 ml of water. In the presence of an ammonium molybdate catalyst, I^- is rapidly oxidized to I_3^- by H_2O_2. To measure the H_2O_2 in a sample, 1 ml of the sample was diluted in 5 ml of distilled water. To that, 2.5 ml each of the reagent solutions were mixed few drops of ammonium molybdate as a catalyst. Absorbance was measured at 350 nm (the wavelength of maximum absorption for I_3^-). The molar extinction coefficient of I_3^- at 350 nm was taken as 25500 M^{-1} cm^{-1} [15]. The concentration of H_2O_2 in the sample was then calculated from the measured absorbance of I_3^-.

3.8   References

[1]   S.R.J. Saunders, M. Monteiro, F. Rizzo, "The Oxidation Behaviour of Metals and Alloys at High Temperatures in Atmospheres Containing Water Vapour: A review", *Progress in Materials Science,* 53, 2008, 775.

[2]   F.A. Lowenheim, "Electroplating", McGraw Hill, New York, 1978.

[3]   R.R. Rodrigues, S.E. Grynberg, A.V. Ferreira, L.C.M. Belo, P.L. Squair, "Retrieval of Gamma Cell 220 Irradiator Isodose Curves with MCNP Simulations and Experimental Measurements", *Brazilian Journal of Physics*, 40, 2010, 120.

[4]   S.N. Upadhyay, N.K. Ray, H.C. Goel, "Dose Distribution Inside Gamma Cell 5000", *Indian Journal of Nuclear Medicine*, 17, 2002, 35.

[5]   Y. Katsumura, G. Wu, M. Lin, Y. Muroya, T. Morioka, Y. Terada, X. Li, "Observation of Hydrated Electron, $(SCN)_2^{\bullet-}$ and $CO_3^{\bullet-}$ Radical in High Temperature and Supercritical Water", *Research on Chemical Intermediates*, 27, 2001, 755.

[6]   M.A. Ribeiro, A.V. Ferreira, L.C. Meira-Belo, S.E. Grynberg, "Use of FRICKE Dosimeters for the Evaluation of Gamma Fields", International Nuclear Atlantic Conference, location date 2009.

[7]   A.I.M. Keulemans, "Gas Chromatography", 2nd ed., Reinhold, New York, 1966.

[8]   D.A. Skoog, F.J. Holler, S.R. Crouch, "Principles of Instrumental Analysis", 6th ed., Thomson Brooks Cole, Belmont, 2007.

[9]   A.B. Littlewood, "Gas Chromatography: Principles, Techniques, and Applications", 2nd ed., Academic Press, New York, 1970.

[10]   Agilent technologies, "A Guide to Interpreting Detector Specifications for Gas Chromatography", www.agilent.com/chem.

[11]   C.N.R. Rao, "Ultra-violet and Visible Spectroscopy: Chemical Applications", Plenum, New York, 1967.

[12]   H.H. Jaffé, M. Orchin, "Theory and Applications of Ultraviolet Spectroscopy", Wiley, New York, 1962.

[13]   J.A. Ghormley, A.C. Stewart, "Effects of γ-radiation on Ice[1]", *Journal of the American Chemical Society*, 78, 1956, 2934.

[14]   C.J. Hochanadel, "Effects of Cobalt γ-Radiation on Water and Aqueous Solutions", *Journal of Physical Chemistry*, 56, 1952, 587.

[15]   O. Roth, J.A. LaVerne, "Effect of pH on H_2O_2 Production in the Radiolysis of Water", *Journal of Physical Chemistry A,* 115, 2011, 700.

CHAPTER 4

DEVELOPMENT OF RADIOLYSIS TEST CELL

4.1   Introduction

The design and construction of a radiolysis test cell for SCW radiolysis studies (up to 450 ºC) poses serious challenges. The test cell must withstand the high temperatures and pressures required for supercritical water conditions and it must maintain this integrity while exposed to γ-irradiation. Reliable sampling of gaseous and aqueous phase products must be possible following completion of the experiment. Moreover, in order to obtain data that reflects the speciation of radiolysis products from water chemistry alone, the cell materials must be inert to any surface reactions that might influence the experimental yields of redox active species, such as H_2, O_2 or H_2O_2, produced during radiolysis. The last point is perhaps the most overlooked in current SCW radiolysis studies. Many experimental setups use flow systems that can tremendously simplify the attainment of supercritical conditions and facilitate product-sampling [1]. However, such flow systems employ long lengths of metallic tubing whose surfaces can participate in corrosion reactions that consume oxidizing species (O_2 and H_2O_2) and generate H_2. Thus, the corrosion of the tubing material can significantly affect the measured concentrations of radiolytically-produced O_2 and H_2O_2. Furthermore, corrosion products released into the aqueous phase can quickly react with radiolytically-generated radicals [2]. As a result, even small amounts of dissolved corrosion products can have a considerable impact on the concentrations of the radiolysis products and change the

solution redox conditions. One of our goals was to develop a cell for operation in stagnant solution conditions with minimal material interferences.

The work started with the development of a new radiolysis test cell for experiments at temperatures up to 450 ^{o}C. Based on past achievements in our laboratory, we were expecting to succeed in developing a new radiolysis cell and test protocol, but substantial time was required for the development task due to the care that must be taken during experiments and the long times required to reach supercritical conditions in a cell. This chapter documents the different cell designs that we developed and tested.

4.2   Quartz Vial

Initially, we tried a handmade half silicate and half quartz radiolysis test cell (Figure 4.1) that could withstand the required high temperature and radiation field. We had successfully used a variant of this cell design for lower temperature studies. We did not expect the design to be successful at supercritical conditions but we wanted to explore the failure modes. Although materials used for this radiolysis cell were satisfactory for moderately high temperature studies, disintegration of the PTFE (polytetrafluoroethylene) silicon septa used for the sealing vial (Figure 4.2) limited its use to 150 ^{o}C and short exposure times. The septum material is gamma compatible for low doses (up to 5 kGy), but at higher doses it breaks down and liberates fluorine gas. Excessive irradiation triggers brittleness [3] and this can lead to a loss of integrity of the gas seal.
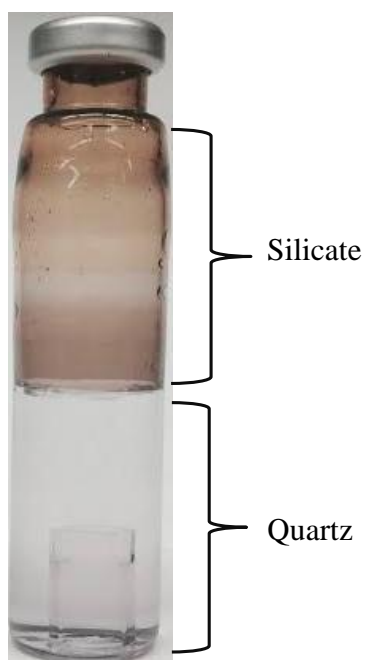
Figure 4.1: Half/half silicate quartz radiolysis vial (discoloration of the silicate half is due to irradiation).
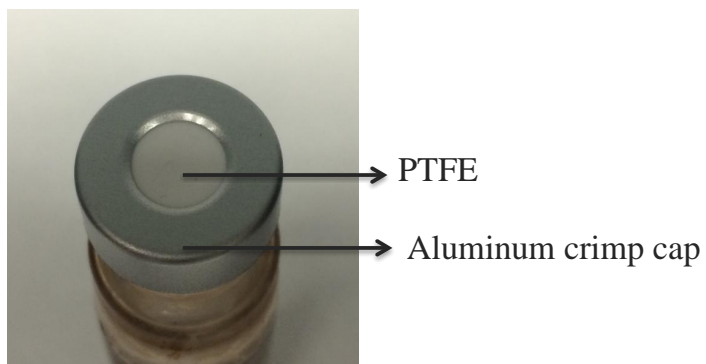
Figure 4.2: Aluminum crimp cap with PTFE silicon septum.

4.3   Gold Bag

An alternative to the glass vial was a steel cell with an inert gold bag that contained the target solution. Gold is a promising design option because gold is known to be highly inert with respect to oxidation and a thin gold foil tube can be readily fabricated into a foil bag that isolates its contents (water and radiolysis products) during and after irradiation. A 99.95% pure gold tube was purchased from Goodfellow Inc. It had a 0.1-mm wall thickness, 7.8-mm inside diameter, and 8-mm outside diameter. In our design approach, a 35-mm length of gold tubing was cut to turn into a gold bag. In order to remove dirt and impurities from gold foil, it was cleaned in boiling (6%) hydrochloric acid for about 10 minutes. The next step was annealing of the gold tube inside a Thermolyne furnace (type 47900). The gold tube was placed inside a crucible and then inside the furnace for 15 minutes at 600 °C, as illustrated in Figure 4.3.
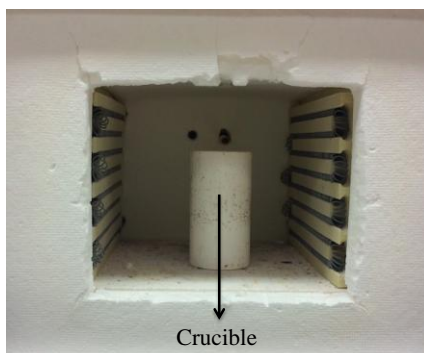
Crucible

Figure 4.3: Crucible contained gold tube inside the furnace.

Afterwards, the gold tube was welded using a micro-spot-welder, supplied by Lampert Co. (model PUK[3] Professional), to shut one flattened end of the gold tube. The

PUK[3] welder was equipped with a microscope (MEZZO) to allow the user to observe the welding process and thereby ensure the proper fusing of end of the tube with no gaps, Figure 4.4. There are a set of large capacitors inside the PUK[3] unit that charge up, and then liberate their energy in a pulse when the welder fires. This creates an arc of plasma between the tip of the tungsten electrode in the PUK[3] hand piece and the gold piece that is being welded. The heat of the plasma melts a small spot of gold, which fuses two parts together, Figure 4.5. The PUK[3] used high-purity argon to avoid oxidation and porosity during welding. In order to start the plasma firing sequence, the tip needed to be in contact with the target. You use sequential welding pulses to get a running seam weld as shown in Figure 4.5. The PUK[3] power and impulse duration was adjusted by trial and error to obtain conditions suitable for welding our gold material (25% power and 7 ms impulse).

The volume of the closed gold bag was estimated to be about 1.5 ml. After adding the solution inside the gold bag, the open end of gold bag welded shut using the same technique described above (Figure 4.6). The sealed gold bag mass was measured at this stage for later comparison with the mass of gold bag after an experiment to see if there was any leakage during a test.

For irradiation tests, the sealed gold bag was placed inside an autoclave. Water was added to autoclave with the same ratio of solution to headspace to match the contents of the gold bag (1:2) to provide a pressure balance. Irradiation was done for 2 hours at 150 °C and then the gold bag was taken out and allowed to cool down. At this stage, the gold bag was weighted to see if there was any leakage from inside or outside. In all of our experiments, the

mass of a gold bag before and after irradiation was the same indicating that the welds were leak tight and stayed intact. Sampling was carried out after a test by piercing the gold bag with a leak-tight syringe.

Figure 4.4: PUK³ welder equipped with a microscope.
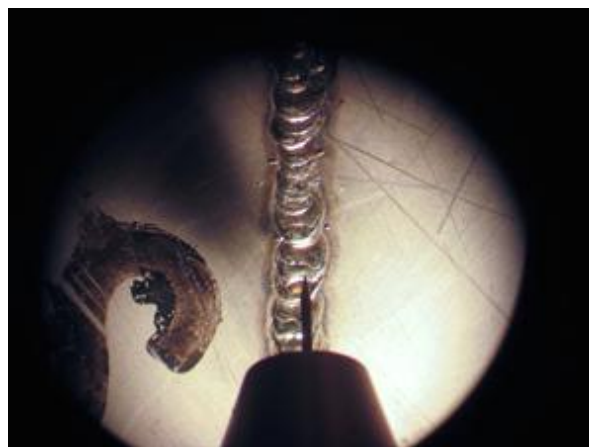
Figure 4.5: The view of Tungsten electrode tip fusing metal under microscope.

Figure 4.6: Welded gold bag.

4.4   Stainless-Steel Radiolysis Cell with a Gold Liner

The gold bag design is fragile and difficult to assemble. As an alternative, we designed a stainless steel cell into which we could place a gold liner. The stainless steel cell was designed by Dr. A.Y. Musa who is a qualified engineer. He designed the cell to meet appropriate rules for a pressure vessel that could be used to contain supercritical water. The design meets ASME (American Society of Mechanical Engineers) meets Section VIII (Rules for Construction of Pressure Vessels) and Section III (Rules for Construction of Nuclear Facility Components) of the ASME Boiler and Pressure Vessel Code (BPVC) and B 31.1 (Rules of Power Piping) and B 31.3 (Radioactive Fluid Services) codes. The result was a 3-ml stainless steel radiolysis pressure cell with five removable parts (Figure 4.7) that can withstand temperatures as high to 420 °C and pressures up to 25 MPa. We designated this as our Mark I SCW test cell.

Figure 4.7: Stainless-steel radiolysis cell.

The cell was comprised of a number of individual components that could be screwed together as shown in Figure 4.8. Each component of the cell has a specific purpose. Part IV essentially acts as a container for the solution when the whole cell is assembled. Part V, screws onto the bottom of part IV and, when closed properly, provides a sealing at the bottom. After screwing parts V and IV together, a test solution can be poured inside the cell. Part III sits on top of part IV. This part provides a solid surface to retain the top of a gold foil liner for the cell (see later). Part II screws onto Part IV and provides pressure on Part III to seal the cylinder. Part II and part III have a small cylindrical hole in the centre to allow for syringe insertion for post-test sample removal. Part I screws into the hole in Part II and can be removed separately at the end of the test. This allows gaseous sampling without the removal of part II and III, which would have, break the seal of the cell.
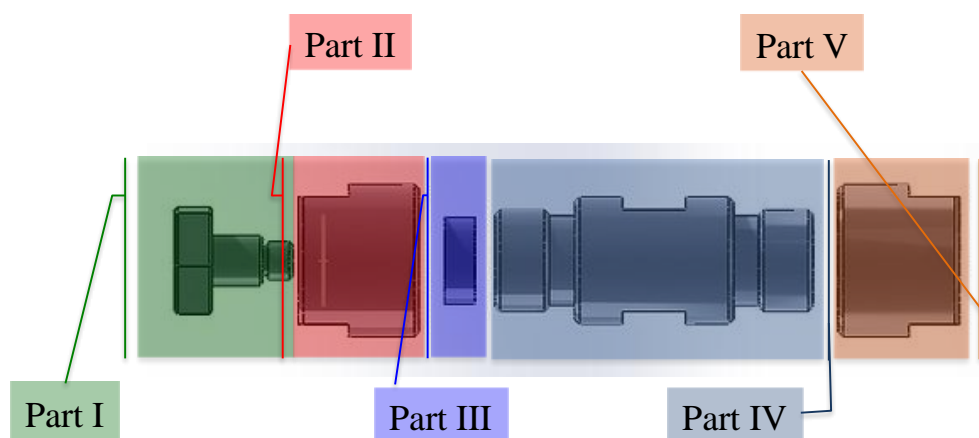
Figure 4.8: Exploded view of the components of the Mark I stainless-steel radiolysis cell.

We used the stainless steel cell with a gold-liner. Prior to inserting a gold liner, the Mark I cell components were gold plated using electroplating technique described in Chapter 3. This was an 'insurance' step in case of any leaks in the gold liner. A gold foil cylinder (0.1 mm wall thickness) with a diameter slightly smaller than the inside diameter of Part IV was placed inside the cylinder with the help of mechanical experts. This task was carried out such that there would be minimum possible gap between cylinder walls and gold liner. The gold foil cylinder extended a small distance beyond both ends of Part IV. The extra foil was mechanically folded onto the ends of Part IV to provide a sealing surface with flat discs of gold foil (with diameters equal to the outer diameter of Part IV) that were placed on the top and bottom of Part IV. The discs were held in place by Part V at the bottom and Parts II and III at the top. Pressure was applied to the joints of the gold foil at top and bottom when screwing the parts together. It has hoped that the combination of the sealing pressure and the

malleability of the thin gold foil would provide a leak-tight seal. The gold-plating of the cell components provided an inert 'outer' container in case the seals were not perfect.

Before any experiments we tested the cell for leakage. In these tests, we put 1 ml water inside the cell (leaving a 2 ml gas head-space). The gold-lined cell then was placed inside an autoclave which had the same ratio of liquid water to gas (1:2) and heated to 250 °C. After 3 hours the gold-lined cell was taken out and cooled down to measure the volume of the water inside using a micro pipet. If the cell was leaking there could have been a change in water volume. In the tests the cells contained exact the same volume of water that was originally placed in the cells. Since the water in the autoclave provided a pressure balance, these tests were not an extreme test of the cell leak-tightness, but provided good evidence that the sealing system was adequate.

To extract a gas sample from the gold-lined cell, the top fitting (part I) was removed and replaced with an alternative piece that contained a PTFE silicon septum. This created a new, leak tight seal on the top of the cell. Then, a gas sample was extracted using our standard technique with a leak-tight syringe that penetrated through both the septum and the gold foil on the top of the cell liner (Figure 4.9). This method prevents gas in-leakage or loss during sampling.

Figure 4.9: Sampling procedure using a leak-tight syringe.

To verify the acceptability of the gold-lined cell design a couple of trial water radiolysis tests were performed to see if we could reproduce the results that were previously obtained for irradiation of pH 10.6 water in a quartz cell at 150 °C in our laboratory. In this trial a quartz cell and a gold-lined cell where tested together in an autoclave. This assures that experimental conditions are the same for both cells.

Unfortunately we were not able to reproduce results seen in the quartz cell with the gold-lined cell design. In particular we saw no gas phase irradiation products formed in the gold-lined cell. We do not understand the reason for this failure. The problem may have been due to the difference in the absolute volumes of water in the two cell designs (8-9 ml for the quartz cell and only 1 ml for the gold-lined cell).

Despite the failures of the gold-lined cell design to duplicate quartz cell results, the absence of radiolysis products may indicate that the cell met the design requirement for inertness. If there have been significant reaction of oxidizing radiolysis products with the cell walls (e.g., by penetrating the gold liner and reacting with the SS cell material) we might have expected to see a net change in the chemistry in the cell water and an unexpectedly high level of H_2 in the cover gas. To address the limitation in the cell volume, the test cell was redesigned.

4.5   Gold Plated Stainless-Steel Radiolysis Cell

The next design was designated the gold-plated SS cell. This cell design was conceptually the same as the gold-lined cell design, with the same component arrangement, but the dimensions were changed and the gold foil liner was eliminated. The central cell component was a 52-mm tall cylinder with 17-mm inner diameter and a 12-ml volume. The internal cell volume was now close to the internal volume of the quartz cells used for other studies in our laboratory (20 ml). With no gold liner, there was a higher requirement for the integrity of the interior gold plating of the cell. While, we had acquired experience in gold plating of the gold-lined cell, we were not confident that the thickness of the gold layer that we had achieved would be protective enough. Hence, the Precision Plating Company was contracted to gold plate the cylinder part of the cell with a 1.2-µm gold coating. It was not essential to do as thick a gold plating on other parts of the cell since two gold foils were still used at the top and bottom of the cylinder and there was no direct contact between the cell solution and other parts of the cell.

Tests of the gold-plated cell were performed with no radiation at 250 °C to verify the adequacy of the design of the new cell. All tests were carried out using pure water at neutral pH. We transferred 4 ml pure water into the cell (leaving an 8-ml headspace). Then, the cell was sealed and put inside an autoclave which contained same ratio of the water to headspace (1:2). The cell loading and sealing was done in an Ar-filled glove box with an O_2 concentration below 1000 ppm). The autoclave was heated for 3 hours at 250 °C.

Since, all these tests were done with no radiation field, we anticipated no hydrogen production inside the cell unless there was a corrosion of the underlying SS cell material. Unfortunately the results of GC analysis of gas from the headspace showed the presence of hydrogen at a concentration of ~ 3×10^{-5} mol·l^{-1}. In comparison, tests under the same conditions with a quartz cell yielded no detectable hydrogen. The presence of H_2 in the gold-plated cell indicates that there is some corrosion of the underlying SS cell material occurring. The gold plating was not sufficiently protective, or cracks at joints in the cell components were allowing water to contact the SS material.

4.6   Gold-Plated Stainless-Steel Radiolysis Cell with Quartz Container

In order to combat the problem of corrosion in the gold-plated cell, we decided to try a cell design with an alternative inert liner. Quartz was chosen for the fabrication of a container that could fit inside the gold-plated SS radiolysis cell. The quartz container was a cylinder with one end. Its dimensions were 30-mm inside depth, 14-mm inner diameter and 4.6-ml volume. There was now no need for a gold foil seal at the bottom of the cell when

assembled. However the top of the quartz container was still sealed by a disc of gold foil that was held in place by Parts II and III.

As for the other cell designs, tests were performed to verify the performance of this cell design. The quartz container was placed inside the gold-plated cell and filled with 4-ml water. Then the cell was sealed, placed in an autoclave in a manner similar to that described above and heated for 3 h at 250 °C. A GC analysis of the headspace gas in the cell after a test found no detectable hydrogen. This cell design appears to meet design requirements. It is expected that a series of tests on the radiolysis of sub- and supercritical water will be performed in the future using this cell design.

4.7   Conclusion

The fabrication of a radiolysis test cell for water radiolysis studies at high temperatures (up to 450 °C) is a challenging task. We have developed few design options for a test cell that can be used for the study of radiolysis kinetics of high-temperature liquid water and steam, subcritical and supercritical water. All the designs have been tested and the final design, gold-plated SS radiolysis cell with quartz container, have successfully conducted radiolysis kinetic tests at temperatures up to 250 °C. The cell design modification will be continued in the future studies.

4.8   References

[1]   G. Wu, Y. Katsumura, Y. Muroya, X. Li, Y. Terada, "Pulse Radiolysis of High Temperature and Supercritical Water : Experimental Setup and e^-_{aq} Observation", *Journal of Radiation Physics And Chemistry,* 60, 2001, 395.

[2]   R.J. Reda, S.L. Akers, J.L. Kelly, "Radiation-enhanced corrosion of mild steel", Transactions of the American Nuclear Society, 53, 1986, 224.

[3]   L.A. Wall, R.E. Florin, "Polytetrafluoroethylene - A Radiation-Resistant Polymer", *Journal of Applied Polymer Science*, 2, 1959, 251.

CHAPTER 5

Gamma-Radiolysis Kinetics of Liquid Water: The Model and the Model Predictions as a Function of pH and Temperature

5.1   Introduction

One of the research objectives was to develop a radiolysis kinetic model for supercritical water that can predict the concentrations of oxidants important for corrosion of in-core materials under the proposed supercritical water reactor (SCWR) coolant conditions. Corrosion of alloys involves surface reactions and interfacial charge and mass transfer between solid metal and water phases, and, if present, through solid oxide [1] and hence is typically much slower than homogeneous aqueous phase reactions. Thus, it is the concentrations of radiolytic water decomposition products on a chemical reaction scale (> ms) that are crucial in determining the corrosion behaviour of in-core materials.

As described in Chapter 2, the radiation of concern in assessing the concentrations of oxidants in the coolant is γ-radiation emitted from radioactive nuclides with exposure time typically longer than a few seconds. In this time scale, the water decomposition products that are formed continuously by radiolytic processes can undergo homogeneous aqueous phase reactions with each other, solvent water molecules and their dissociated ions, and, if present, dissolved species. As the secondary or intermediate radiolysis products accumulate their reactions become also more important. Some of these chemical reactions establish a catalytic cycle. Nevertheless, due to the chemically reactive nature of radiolytic decomposition

products of water the concentrations of redox active species (such as $\bullet OH$, H_2O_2, O_2, $\bullet O_2^-$) reach pseudo-steady state within the water phase on a relatively short time scale (short for solution reactions) [2,3]. It should be noted that the steady state is not a thermodynamic equilibrium state but is a kinetic balance between production and decomposition reactions of the radiolysis products. The rate of a chemical reaction depends on the concentration of the reactants at a given time and not the overall amount of the reactants. Thus, it is the concentrations at pseudo-steady state, not the radiolytic yields that are critical in determining corrosion rates of SCWR in-core materials.

Our current understanding of chemical reaction kinetics in sub-critical and supercritical water is not sufficient to construct a fully validated model for the γ-radiolysis of SCW under continuous (> ms) irradiation. In particular the effects of the changing water properties in the sub- and supercritical regimes are not fully understood. Thus, we are using a two-pronged approach to the kinetics modeling coming from high density (liquid) and low-density (vapour) perspectives and hence creating two models: (1) a liquid radiolysis model (LRM) and (2) a vapour radiolysis model (VRM) for the continuous radiolysis of sub-critical and supercritical water. Our aim is to have the models converge as they mature. Chapter 8 describes the rationales behind the approach, the two models, assignment of the kinetic parameters (G-values and rate constants) at the SCW temperatures and pressures, and the analysis of the model results.

The two models, LRM and VRM, are based on an existing liquid water radiolysis model [4–8] and an existing water vapour radiolysis model [9]. To extend the application of

these models to SCW conditions with any confidence, the radiolysis kinetics of liquid water and water vapour as a function of temperature and pressure should be well understood. Thus, the liquid water radiolysis kinetics as a function of pH and temperature is examined in detail in this chapter and the kinetics of vapour radiolysis in Chapter 6. Chapter 5 presents the model simulations of radiolysis experiments of liquid water in contact with saturated water performed at 25 °C, 150 °C and 250 °C.

We have previously reported on a chemical kinetic model for liquid water radiolysis that was developed to determine the concentrations of radiolysis products as a function of time under continuous irradiation of γ-radiation [4,6]. This model has successfully simulated the observed time-dependent concentrations of molecular products, H_2 and H_2O_2, as a function of pH and dissolved oxygen concentration during γ-irradiation of single phase liquid water [6] and a biphasic liquid water and gas system [8] at room temperature. The model with the addition of the reactions of nitrogen/oxygen species with the radiolytic water decomposition products was also successfully applied to the radiolysis of aqueous solutions containing nitrate and nitrite ions [7]. The successful simulations of experimental results obtained in tests with a range of different radiolysis and solution conditions demonstrate the robustness of the model at room temperature.

Although it has not been validated extensively at higher temperatures the model has the capability to predict the kinetic behaviour of liquid water radiolysis as a function temperature. The model includes through the temperature dependences of its rate parameters such as rate constants and the density of water. In this chapter, we present a brief description

of the model and the model parameters, and model calculation results as a function of pH and temperature. The computational results are further analysed to identify the key reactions and reaction parameters that are important in determining the effect of temperature and pH on the net radiolytic production of H_2, O_2 and H_2O_2. We also establish the relationships between the measurable quantities (concentrations of the molecular products) and non-measurable quantities (the concentrations of radical species).

5.2 Liquid Water Radiolysis Model

5.2.1 Model description

In construction of a kinetics model, it is essential that all the relevant reactions are included in the model and that the rate constants of the individual reactions are accurate enough for the intended applications of the modelling results. The radiolysis kinetic model for liquid water consists of ~40 elementary homogeneous reactions (Table 5.1), including primary radiolytic production of water decomposition products and the aqueous phase reactions of the radiolysis products with each other and with solvent water molecules, and their acid–base equilibria (Table 5.3).

Table 5.1: Reactions and their rate constants included in the model[1].

ID#	Primary Radiolysis	Rate Constants[2] ($M \cdot s^{-1}$)
G1	$H_2O \rightarrow \bullet e_{aq}^-$	$10^{-6} \cdot G_{\bullet e}(T) \cdot \rho(T) \cdot D_R$
G2	$H_2O \rightarrow H^+$	$10^{-6} \cdot G_H(T) \cdot \rho(T) \cdot D_R$
G3	$H_2O \rightarrow \bullet H$	$10^{-6} \cdot G_{\bullet H}(T) \cdot \rho(T) \cdot D_R$

G4	$H_2O \rightarrow •OH$	$10^{-6} \cdot G_{•OH}(T) \cdot \rho(T) \cdot D_R$
G5	$H_2O \rightarrow H_2$	$10^{-6} \cdot G_{H2}(T) \cdot \rho(T) \cdot D_R$
G6	$H_2O \rightarrow H_2O_2$	$10^{-6} \cdot G_{H2O2}(T) \cdot \rho(T) \cdot D_R$
	Aqueous Phase Reactions	**Rate Constants[3] ($M^{-1} \cdot s^{-1}$ or s^{-1})**
R1	$•e_{aq}^- + •e_{aq}^- + 2\,H_2O$ $\rightarrow H_2 + 2\,OH^-$	**(T ≤150 °C)** $10@\,[12.28 - (3.76 \times 10^2 / T) - (6.67 \times 10^4/(T)^2) - (1.07 \times 10^7/(T)^3)]$ **(T>150 °C)** $10@\,[-47.53 + (4.92 \times 10^4 / T) - (1.03 \times 10^7/(T)^2]$
R2	$•e_{aq}^- + •H + H_2O$ $\rightarrow H_2 + OH^-$	$1.14 \times 10^{13} \times \exp(-1795.7 \times T)$
R3	$•e_{aq}^- + •OH \rightarrow OH^-$	$10@\,[13.12 - (1.02 \times 10^3 / T) + (7.63 \times 10^4/(T)^2]$
R4	$•e_{aq}^- + O_2 \rightarrow •O_2^-$	$2.52 \times 10^{12} \times \exp(-1401.5 \times T)$
R5	$•e_{aq}^- + H_2O_2 \rightarrow OH^- + •OH$	$7.7 \times 10^{12} \times \exp(-1889.6 \times T)$
R6	$•e_{aq}^- + HO_2• \rightarrow HO_2^-$	$2.46 \times 10^{12} \times \exp(-1563.6 \times T)$
R7	$•e_{aq}^- + HO_2^- \rightarrow •O^- + OH^-$	$3.51 \times 10^9 \times \exp(15400 \times T_F)$
R8	$•e_{aq}^- + •O^- + H_2O \rightarrow OH^- + OH^-$	$2.31 \times 10^{10} \times \exp(7900 \times T_F)$
R9	$•H + •OH \rightarrow H_2O$	$4.26 \times 10^{11} \times \exp(-1091.9 \times T)$
R10	$•H + •H \rightarrow H_2$	$2.7 \times 10^{12} \times \exp(-1867.5 \times T)$
R11	$•H + O_2 \rightarrow HO_2•$	$10@\,[10.70 + (2.84 \times 10^2 / T) - (1.36 \times 10^5/(T)^2]$
R12	$•H + HO_2• \rightarrow H_2O_2$	$5.17 \times 10^{12} \times \exp(-1824.2 \times T)$
R13	$•H + H_2O_2 \rightarrow •OH + H_2O$	$1.79 \times 10^{11} \times \exp(-2533.6 \times T)$
R14	$•H + •O_2^- \rightarrow HO_2^-$	$5.17 \times 10^{12} \times \exp(-1824.2 \times T)$
R15[*]	$•H + H_2O \rightarrow H_2 + •OH$	$10@\,[9.40 - (2.82 \times 10^3 / T) - (3.79 \times$

		$10^5/(T)^2]$
R16	$\cdot OH + \cdot OH \rightarrow H_2O_2$	$10@ [8.054 + (2.19 \times 10^3 / T) - (7.39 \times 10^5/(T)^2) + (6.87 \times 10^7/(T)^3)]$
R17	$\cdot OH + H_2O_2 \rightarrow HO_2\cdot + H_2O$	$7.68 \times 10^9 \times \exp(-1661.4 \times T)$
R18	$\cdot OH + H_2 \rightarrow OH^- + O_2$	$10@ [-11.55+(3.25 \times 10^4/T) - (1.86 \times 10^7/(T)^2) + (4.55 \times 10^9/(T)^3) - (4.13 \times 10^{11}/(T)^4)]$
R19	$\cdot OH + \cdot O_2^- \rightarrow OH^- + O_2$	$8.77 \times 10^{11} \times \exp(-1306.2 \times T)$
R20	$\cdot OH + HO_2\cdot \rightarrow H_2O + O_2$	$1.29 \times 10^{11} \times \exp(-799.2 \times T)$
R21	$\cdot OH + HO_2^- \rightarrow HO_2\cdot + OH^-$	$1.0 \times 10^{12} \times \exp(-1434.6 \times T)$
R22	$\cdot OH + \cdot O^- \rightarrow HO_2^-$	$1.0 \times 10^{12} \times \exp(-1434.6 \times T)$
R23	$\cdot O^- + H_2O_2 \rightarrow \cdot O_2^- + H_2O$	$5.0 \times 10^8 \times \exp(15600 \times T_F)$
R24	$\cdot O^- + H_2 \rightarrow H\cdot + OH^-$	$2.32 \times 10^{10} \times \exp(1550.5 \times T)$
R25	$\cdot O^- + HO_2^- \rightarrow \cdot O_2^- + OH^-$	$1.45 \times 10^{13} \times \exp(-2928.5 \times T)$
R26	$\cdot O^- + \cdot O_2^- \rightarrow 2 OH^- + O_2$	$6.0 \times 10^8 \times E_a$
R27	$\cdot O^- + O_2 \rightarrow \cdot O_3^-$	$3.41 \times 10^{11} \times \exp(-1344.9 \times T)$
R28	$\cdot O_3^- \rightarrow O_2 + \cdot O^-$	$3.2 \times 10^{11} \times \exp(-5552.1 \times T)$
R29	$\cdot O_3^- + H_2O_2 \rightarrow \cdot O_2^- + O_2 + H_2O$	$1.6 \times 10^6 \times E_a$
R30	$\cdot O_3^- + HO_2^- \rightarrow \cdot O_2^- + O_2 + OH^-$	$8.9 \times 10^5 \times E_a$
R31	$\cdot O_3^- + H_2 \rightarrow O_2 + H\cdot + OH^-$	$2.5 \times 10^5 \times E_a$
R32	$HO_2\cdot + \cdot O_2^- \rightarrow HO_2^- + O_2$	$2.63 \times 10^9 \times \exp(-974.3 \times T)$
R33	$HO_2\cdot + HO_2\cdot \rightarrow H_2O_2 + O_2$	$2.78 \times 10^9 \times \exp(-2416.4 \times T)$
R34[*]	$H_2O_2 \rightarrow \cdot OH + \cdot OH$	$2.3 \times 10^{-7} \times \exp(71000 \times T_F)$
R35f	$H^+ + OH^- \rightarrow H_2O$	$10@ [20.934 - (12360/T_C) + (6364000/ T_C^2) - (14.75 \times 10^8 / T_C^3) + (12.37 \times 10^{10} / T_C^4)$
R35b	$H_2O \rightarrow H^+ + OH^-$	$k_{35f} \times K_W$
R36f		$(7.22 \times 10^9) + (1.62 \times 10^8 \times T_C) + (2.4 \times 10^6 \times$

	$H^+ + HO_2^- \rightarrow H_2O_2$	$T_C{}^2) - (7.81 \times 10^3 \times T_C{}^3) + (10.6 \times T_C{}^4)$
R36b	$H_2O_2 \rightarrow H^+ + HO_2^-$	k_{36f}/K_{H2O2}
R37f	$H^+ + \bullet O_2^- \rightarrow HO_2\bullet$	$(7.22 \times 10^9) + (1.62 \times 10^8 \times T_C) + (2.4 \times 10^6 \times T_C{}^2) - (7.81 \times 10^3 \times T_C{}^3) + (10.6 \times T_C{}^4)$
R37b	$HO_2\bullet \rightarrow H^+ + \bullet O_2^-$	$k_{37f} / K_{\bullet HO2}$
R38f	$H^+ + \bullet O^- \rightarrow \bullet OH$	$(7.22 \times 10^9) + (1.62 \times 10^8 \times T_C) + (2.4 \times 10^6 \times T_C{}^2) - (7.81 \times 10^3 \times T_C{}^3) + (10.6 \times T_C{}^4)$
R38b	$\bullet OH \rightarrow H^+ + \bullet O^-$	$k_{38f} / K_{\bullet OH}$
R39f	$H^+ + \bullet e_{aq}^- \rightarrow \bullet H$	$1.33 \times 10^{14} \times \exp(-38380/(8.314 \times T)$
R39b	$\bullet H \rightarrow H^+ + \bullet e_{aq}^-$	$k_{39f} / K_{\bullet H}$

1   Temperature T is in K, $T_F = [(1/298.15)-(1/T)]/R$ and T_C is in °C
2   The G-values and water density ($\rho(T)$) as a function of temperature are presented in Tables 5.2 and 5.3, respectively.
3   The rate constants for the elementary reactions are 2nd order rate constants ($M^{-1} \cdot s^{-1}$) except for reactions denoted with * (R15 and R34). For the reactions involving H_2O the concentration of H_2O is included in the rate constant.
4   The rate constants (k_b) for the reverse reactions are calculated from the forward rate constants (k_f) and the corresponding equilibrium constants (K). The equilibrium constants as a function of temperature are presented in Table 5.3.

In our model the primary radiolytic processes occurring at short times (< 0.1 μs), from the interaction of a high energy photon or electron with a water molecule to the attainment of homogeneous (or out-of-spur) distribution of water decomposition products along the track (see Chapter 2), are not modelled in detail. Instead, the radiolysis is modelled using the homogeneous primary radiolysis yields per absorbed energy or G-values and the rate of radiation energy deposition into water. That is, the rate of production of species i (in units of $M \cdot s^{-1}$) by primary radiolysis processes is defined as

$$\frac{d[i]}{dt} = 10^{-6} \cdot G_i(T) \cdot \rho(T) \cdot D_R \tag{5.1}$$

where $G_i(T)$ is the G-value for species i at temperature T in units of $\mu mol\cdot J^{-1}$, D_R is the absorbed radiation dose rate in units of $Gy\cdot s^{-1}$ ($J\cdot kg^{-1}\cdot s^{-1}$), and $\rho(T)$ is the density of water at T in units of $kg\cdot dm^{-3}$ (the factor of 10^{-6} provides for unit conversion). The dose rate is normally expressed as the rate of absorbed radiation energy per unit mass of the solvent medium that is irradiated (Chapter 2). Since the rate of a chemical reaction depends on molarity, not molality, the rate of energy absorption per unit mass is converted to the rate of energy absorption per unit volume by multiplying it with the density of water.

The rate of change in the concentration of a chemical species, i, due to aqueous phase reactions is described by the classical chemical reaction rate equation. For a bimolecular reaction:

$$\frac{d[i]}{dt} = \sum_{l,m \to i} k_{lm}(T) \cdot [l] \cdot [m] - \sum_j k_{ij}(T) \cdot [j] \cdot [i] \tag{5.2}$$

where $k_{lm}(T)$ is the 2nd order rate constant at temperature T for the reaction of species l and m producing species i in units of $M^{-1}\cdot s^{-1}$, and $k_{ij}(T)$ is the 2nd order rate constant at T for the reaction of species i and j in units of $M^{-1}\cdot s^{-1}$. The reactions involving water molecule are treated as pseudo-first-order reactions with a first-order rate constant ($k_{i\text{-}H2O}(T)\cdot[H_2O]$) in unit of s^{-1}. For a given species the overall rate law is then

$$\frac{d[i]}{dt} = 10^{-6} \cdot G_i(T) \cdot \rho(T) \cdot D_R + \sum_{l,m \to i} k_{lm}(T) \cdot [l] \cdot [m] - \sum_j k_{ij}(T) \cdot [l] \cdot [m] \tag{5.3}$$

With a set of elementary reactions and their rate constants, the time evolution of the concentrations of radiolysis products can be followed by constructing the rate equations for

individual species and solving the coupled time-dependent rate equations using commercial software (the FACSIMILIE code).

The effect of temperature on the overall radiolysis kinetics is modelled through the temperature dependences of the G-values and the rate constants of the individual elementary reactions and water density. The temperature dependences of these model parameters are described below.

5.2.2 Model Parameters

The homogeneous G-values for the primary radiolysis products in liquid water are well established over a wide range of temperatures. Elliot and Bartels conducted an extensive review of the G-values reported for the range of 25 °C to 300 °C and recommended polynomial formulae for the G-values as a function of temperature [10]. In our radiolysis kinetic model, we have used their formulae to calculate G-values as a function of temperature except for the G-value for H_2O_2. For kinetic modeling mass balance must be strictly observed. Thus, the G-value for H_2O_2 at any T was obtained from charge and mass balance requirements that the atomic ratio of $\bullet e_{aq}^-$ to H^+ in the sum of the water decomposition product yields must be equal and the atomic ratio of H to O must be 2 to 1:

$$G_{H+}(T) \ = G_{\bullet e\,(aq)}(T) \tag{5.4}$$

$$G_{H2O2}(T) = [G_{\bullet H}(T) \ + 2\ G_{H2}(T) \ + G_{\bullet e\,(aq)}(T) - G_{\bullet OH}(T)]/2 \tag{5.5}$$

The temperature-dependences of the G-values used in the model are presented in Table 5.2.

Table 5.2: Temperature dependences of the homogeneous primary
radiolysis yields (G-values in units of μmol·J^{-1}) [11].

G-value	Temperature Dependence
G ($\bullet e_{aq}^{-}$)	$1.036 \times [2.641 + (4.16 \times 10^{-3} \times T) + (9.09 \times 10^{-6} \times T^2) - (4.72 \times 10^{-8} \times T^3)]$
G (H$_2$)	$1.036 \times [0.419 + (8.72 \times 10^{-4} \times T) - (4.79 \times 10^{-6} \times T^2) + (1.50 \times 10^{-8} \times T^3)]$
G ($\bullet$OH)	$1.036 \times [2.531 + (1.13 \times 10^{-2} \times T) - (1.26 \times 10^{-5} \times T^2) + (3.51 \times 10^{-8} \times T^3)]$
G (H+)	$1.036 \times [2.641 + (4.16 \times 10^{-3} \times T) + (9.09 \times 10^{-6} \times T^2) - (4.72 \times 10^{-8} \times T^3)]$
G ($\bullet$H)	$1.036 \times [0.556 + (2.19 \times 10^{-3} \times T) - (1.18 \times 10^{-5} \times T^2) + (5.22 \times 10^{-8} \times T^3)]$
G (H$_2$O$_2$)	$[G (\bullet H) + 2\, G (H_2) + G (H^+) - G (OH)]/2$

* Temperature in ^{o}C

The temperature dependence of a homogeneous chemical reaction rate constant arises from the activation energy and the pre-exponential factor according to the Arrhenius equation:

$$k_{ij}(T) = A_{ij}(T) \cdot \exp\left(-\frac{E_A}{RT}\right) \tag{5.6}$$

where E_A is the activation energy for the reaction and R is the gas constant. The exponential component is a measure of the fraction of collisions between the reactants that have sufficient energy to overcome the activation energy barrier of the reaction. The pre-exponential factor, $A_{ij}(T)$, is an effective collision frequency for the reactants, since not all collisions with sufficient energy will lead to chemical reaction.

In the model the temperature-dependences of the rate constants are expressed using the Arrhenius equation. The activation energy and the temperature dependence of the pre-

exponential factor, A_{ij} (T), are those provided by Elliot and Bartels [10] and are listed in Table 5.1. The temperature dependences of the equilibrium constants for the acid-base equilibria of the radicals and water dissociation are also well established (Table 5.2) [12–15]. For these equilibrium reactions, the rate constants for the forward bimolecular reactions (Table 5.1) are diffusion limited and the rate constants of the reverse reactions are obtained from the corresponding equilibrium constants.

In addition to the kinetic parameters the density of water is an important parameter in the model. The temperature dependence of the density of water is given in Table 5.3 and taken from Reference [16]:

Table 5.3: Equilibrium rate constants and density as a function of temperature (°C) in the liquid model [11].

ID #	Reaction	Equilibrium Rate Constants $(M^{-1} \cdot s^{-1})$
R35f/R35b	$H_2O \leftrightarrows H^+ + OH^-$	$pK_w = 14.95 - (4.27 \times 10^{-2} \times T) + (21.15 \times 10^{-5} \times T^2) - (57.86 \times 10^{-8} \times T^3) + (75.92 \times 10^{-11} \times T^4)$
R36f/R36b	$H^+ + HO_2^- \leftrightarrows H_2O_2$	$pK (H_2O_2) = 12.5 - (3.31 \times 10^{-2} \times T) + (1.96 \times 10^{-4} \times T^2) - (6.19 \times 10^{-7} \times T^3) + (8.24 \times 10^{-10} \times T^4)$
R37f/R37b	$H^+ + \bullet O_2^- \leftrightarrows HO_2\bullet$	$pK (HO_2\bullet) = 4.917 - (3.81 \times 10^{-3} \times T) + (8.77 \times 10^{-7} \times T^2) - (2.17 \times 10^{-7} \times T^3) + (4.00 \times 10^{-10} \times T^4)$
R38f/R38b	$H^+ + \bullet O^- \leftrightarrows \bullet OH$	$pK (\bullet OH) = 12.5 - (3.31 \times 10^{-2} \times T) + (1.96 \times 10^{-4} \times T^2) - (6.19 \times 10^{-7} \times T^3) + (8.24 \times 10^{-10} \times T^4)$
R39f/R39b	$H^+ + \bullet e_{aq}^- \leftrightarrows \bullet H$	$pK (H) = 10.49 - (4.10 \times 10^{-2} \times T) + (1.44 \times 10^{-4} \times T^2) - (2.32 \times 10^{-7}$

		$\times\,\mathrm{T}^3) + (2.0 \times 10^{-10} \times \mathrm{T}^4)$
Water Density (kg^{-1}·L^{-1})		
ρ (T)	$0.999 + (1.094 \times 10^{-4} \times \mathrm{T}) - (7.397 \times 10^{-6} \times \mathrm{T}^2) + (2.693 \times 10^{-8} \times \mathrm{T}^3) - (4.714 \times 10^{-11} \times \mathrm{T}^4)$	

5.3 Model Results

We have performed a series of model calculations to identify the key reactions and reaction parameters that are important in determining the effect of pH, temperature and dose rate on the net radiolytic production of H_2, O_2 and H_2O_2, and to establish the relationships between the measurable quantities (concentrations of the molecular products) and non-measurable quantities (the concentrations of radical species).

5.3.1 Time Evolution of Radiolysis Product Concentrations

For a given set of conditions (pH, temperature and dose rate) the concentrations of radiolysis products show distinct time dependences over different periods. For example, the model results obtained for γ-radiolysis at 4.5 kGy·h^{-1}, pH 6.0 and 25 °C are presented in Figure 5.1. The concentration of each species shows three distinct periods over the time span of 10^4 s (~ 3 h), as indicated in Figure 5.1. In Stage I, the concentrations of the primary radiolysis products increase linearly but no secondary products are yet formed. In Stage II, the radical primary products reach steady state while the concentrations of the molecular primary products continue to increase and secondary products start being produced at fast

rates. In Stage III, the concentrations of all the radiolysis products are at steady state. (Note that in Figure 5.1 the results are plotted in log [i] vs log t, and not log [i] vs t.)
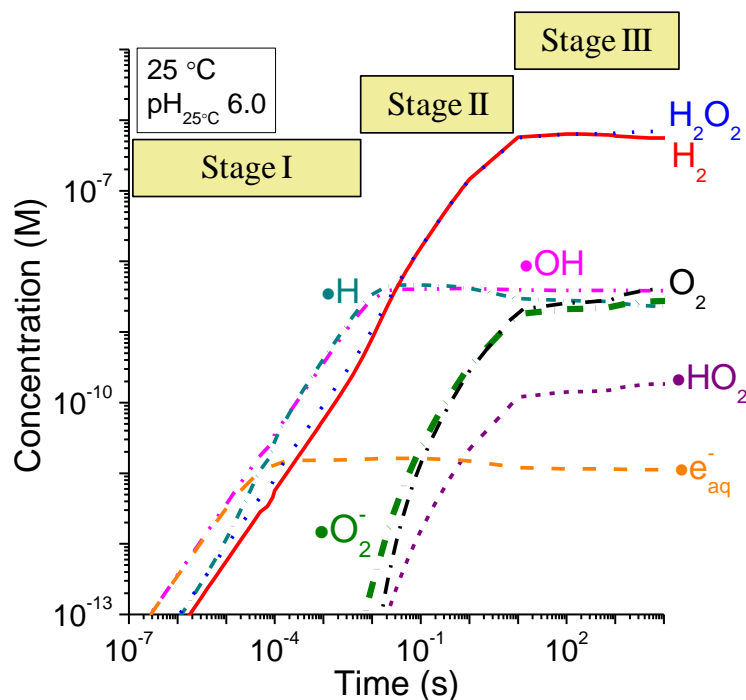
Figure 5.1: The concentration of water radiolysis products as a function of irradiation time at pH 6.0 in deaerated water at 25 ^{o}C and a dose rate of 4.5 kGy·h^{-1}.

In Stage I, the log [i] vs. log t plots for the primary radiolysis products show slopes of 1.0 and their intercepts are proportional to $log(G_i(T))$, except for $\bullet e_{aq}^-$ and $\bullet$H. That is, the concentration of a radiolysis product increases at a rate determined only by the primary radiolytic production processes:

$$[i] \approx 10^{-6} \cdot G_i(T) \cdot \rho(T) \cdot D_R \cdot t \tag{5.7a}$$

$$log\ [i] \approx log(10^{-6} \cdot G_i(T) \cdot \rho(T) \cdot D_R) + log\ t \tag{5.7b}$$

The time for the concentration of a species to reach a steady state depends on the chemical reactivity of the species. The most reactive $\bullet e_{aq}^-$ reaches steady state in ~10 μs at pH 6.0. This suggests that the rate of decomposition of $\bullet e_{aq}^-$ has already approached its radiolytic production rate within this short time. During this time, the net production rate of $\bullet H$ is greater than the radiolysis production rate alone (slope>1) indicating that the removal path for $\bullet e_{aq}^-$ is R39f in Table 5.1

$$\bullet e_{aq}^- + H^+ \rightarrow \bullet H \tag{5.8}$$

Since this reaction produces $\bullet H$, the net rate of $\bullet H$ production in this stage is the sum of the primary radiolytic production (G3 in Table 5.1) and the rate of the decomposition reaction of $\bullet e_{aq}^-$ (R39f in Table 5.1). Since the latter rate is the same as the radiolytic production rate for $\bullet e_{aq}^-$, the net rate of $\bullet H$ production in this stage is:

$$[\bullet H] \approx 10^{-6} \cdot \left(G_{\bullet H}(T) + G_{\bullet e}(T)\right) \cdot \rho(T) \cdot D_R \cdot t \tag{5.9}$$

Near the end of Stage I the concentrations of $\bullet OH$ and $\bullet H$ increase to sufficiently high levels that they start to react at substantial rates with each other and with the molecular species present through a series of reactions:

$$\bullet OH + \bullet OH \rightarrow H_2O_2 \tag{5.10}$$

$$\bullet H + \bullet H \rightarrow H_2 \tag{5.11}$$

$$\bullet OH + H_2 \rightarrow \bullet H + H_2O \tag{5.12}$$

$$\bullet OH + H_2O_2 \rightarrow \bullet HO_2 + H_2O \qquad (5.13)$$

$$\bullet HO_2 + \bullet HO_2 \rightarrow H_2O_2 + O_2 \qquad (5.14)$$

$$\bullet HO_2 + \bullet O_2^- \rightarrow HO_2^- + O_2 \qquad (5.15)$$

$$\bullet HO_2 \leftrightarrows H^+ + \bullet O_2^- \qquad (5.16)$$

The net effect is slow conversion of more reactive chemical species, $\bullet OH$ and $\bullet H$, to less reactive species, $\bullet HO_2$ and $\bullet O_2^-$, and to H_2O_2, O_2 and H_2.

As the concentrations of the molecular primary products and the secondary products increase, the rates of the decomposition reactions of $\bullet OH$ and $\bullet H$ via reactions (5.10) to (5.16) increase and quickly approach those of their radiolytic production:

$$10^{-6} \cdot G_{\bullet OH}(T) \cdot \rho(T) \cdot D_R \approx \sum_j k_{\bullet OH-j}(T) \cdot [\bullet OH] \cdot [j] \qquad (5.17)$$

$$10^{-6} \cdot G_{\bullet H}(T) \cdot \rho(T) \cdot D_R \approx \sum_j k_{\bullet H-j}(T) \cdot [\bullet H] \cdot [j] \qquad (5.18)$$

The concentrations of $\bullet OH$ and $\bullet H$ reach near steady state in Stage II. In Stage II, the concentrations of H_2O_2 and H_2 and those of the main secondary products increase linearly with time (i.e., the slopes of log [i] vs log t are ~ 1); the rates of net production of H_2O_2 and H_2 are nearly constant. However, these rate constants are larger than their primary radiolytic production rate constants ($10^{-6} \cdot G_i(T) \cdot \rho(T) \cdot D_R$) due to the additional production of these species by the aqueous phase reactions of $\bullet OH$ and $\bullet H$ (reactions 5.10 and 5.11). In Stage II the net decomposition rate constants of $\bullet OH$ and $\bullet H$ are the same as their primary radiolytic production rate constants (equations 5.17 and 5.18). A fraction of the net decomposition of $\bullet OH$ and $\bullet H$, f_{H2O2} and f_{H2}, results in the production of H_2O_2 and H_2, respectively. The

remaining fraction is used for producing the secondary products. Thus, the concentrations of H_2O_2 and H_2 increase linearly with time in Stage II at rates:

$$[H_2O_2] \approx 10^{-6} \cdot \left(G_{\text{H2O2}}(T) + f_{H2O2} \cdot G_{\bullet\text{OH}}(T)\right) \cdot \rho(T) \cdot D_R \cdot t \tag{5.19}$$

$$[H_2] \approx 10^{-6} \cdot \left(G_{\text{H2}}(T) + f_{H2} \cdot G_{\bullet\text{H}}(T)\right) \cdot \rho(T) \cdot D_R \cdot t \tag{5.20}$$

The fractions, f_{H2O2} and f_{H2}, depend on pH and temperature. As the concentrations of H_2O_2 and H_2 as well as the secondary products continue to increase in Stage II, the net rates of their decomposition reactions also increase and become equal to the net rates of their production rates, and the whole radiolysis system reaches near steady state (Stage III):

$$[H_2] \approx \frac{10^{-6} \cdot \left(G_{\text{H2}}(T) + f_{H2} \cdot G_{\bullet\text{H}}(T)\right) \cdot \rho(T) \cdot D_R}{k_{18}[\bullet\text{OH}]} \tag{5.21}$$

$$[H_2O_2] \approx \frac{10^{-6} \cdot \left(G_{\text{H2O2}}(T) + f_{H2O2} \cdot G_{\bullet\text{OH}}(T)\right) \cdot \rho(T) \cdot D_R}{k_{17}[\bullet\text{OH}] + k_5[\bullet\text{e}^-_{\text{aq}}]} \tag{5.22}$$

where the subscript Rn in k_{Gn} represents the rate constant of aqueous phase reaction Rn in Table 5.1. These relationships show how the molecular species reactions become progressively more important in controlling the concentrations of the radiolysis products at later stages (> ms). Because of the complexity of the processes that form and remove molecular species, their concentrations cannot be predicted based on simple competition kinetics, see further discussion.

The relationships between the molecular and radical product concentrations presented in equations (5.21) and (5.22) have many implications. Under γ-irradiation, *in-situ*

monitoring of radiolysis products, and particularly short-lived radical species, is practically impossible. Molecular products, particularly H_2 and O_2, are easier to measure than those of radical species, since they persist when irradiation ceases (e.g., when water moves out of a radiation zone). Equations (5.21) and (5.22) provide the means to extract the non-measurable quantities (the concentrations of radical species) from the measured quantities (concentrations of the molecular products) in irradiated water.

Dissolved chemical additives (such as O_2, N_2O) at small concentrations (< 1 mM) may not react directly with H_2 and H_2O_2 at a substantial rate but they can affect the net radiolytic production of H_2 and H_2O_2 indirectly by reacting with the radical products, $\cdot e_{aq}^-$ and $\cdot OH$. Similarly additives that change the pH or $[H^+]$ will have a strong impact on $[\cdot e_{aq}^-]$ (through Eq. 5.8) and consequently $[H_2]$ and $[H_2O_2]$, see further discussion in Section 5.3.2.

5.3.2   Effect of pH on Radiolysis Kinetics

The model calculation results for γ-radiolysis at pHs 3.0, 7.0 and 10.6 at 25 ^{o}C are compared in Figure 5.2. The three stages observed at pH 6.0 are also present at pH 3.0. At pH 10.6 there are only two stages seen within 10^4 s; Stage III when the whole system reaches steady stat occurs at longer times. At pH 10.6, the radiolysis behaviour in Stage II is also markedly different from those observed at the lower pHs.
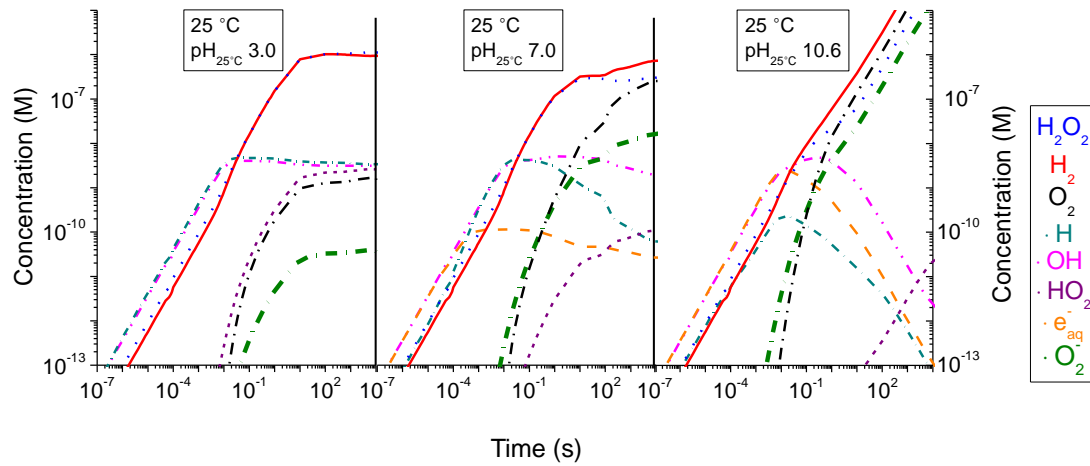
Figure 5.2: The concentration of water radiolysis products as a function of irradiation time at pH 3.0, 7.0 and 10.6 in deaerated water at   25 °C and a dose rate of 4.5 kGy·h⁻¹.

The time dependent behaviour of radiolysis products in Stage I is essentially the same at all pHs; the concentration of a radiolysis product increases linearly with time at a rate determined by primary radiolytic processes, according to Equation (5.7). In Stage I, the main effect of pH is on $[•e_{aq}^{-}]$ due to the reaction:

$$•e_{aq}^{-} + H^{+} \leftrightarrows •H \qquad\qquad pK_a \text{ of } •H = 9.6 \qquad\qquad (5.23)$$

The higher concentration of H^{+} at a lower pH increases the rate of reaction (5.23), leading to a faster attainment of steady state and a lower concentration of $•e_{aq}^{-}$ in Stages II and III. At pH 3.0 $[•e_{aq}^{-}]$ in fact is never higher than 10^{-13} M and the rate of increase in $[•H]$ in Stage I is proportional to the sum of $G_{•e}$ and $G_{•H}$ and not just $G_{•H}$:

$$[• H] \approx 10^{-6} \cdot \left(G_{•H}(T) + G_{•e}(T)\right) \cdot \rho(T) \cdot D_R \cdot t \qquad\qquad (5.24)$$

At pH 7.0 [$\bullet e_{aq}^-$] reaches steady state at a later time and a higher level but this level is still low (about 10^{-11} M). The rate of increase in [$\bullet$H] is initially proportional to $G_{\bullet H}$ before [$\bullet e_{aq}^-$] reaches steady state but then becomes proportional to the sum of $G_{\bullet e}$ and $G_{\bullet H}$. At pHs > 6.0, the steady-state concentration of $\bullet e_{aq}^-$ is not negligible. At pH 10.6 reaction (5.23) is very slow and [$\bullet e_{aq}^-$] increases linearly at a rate proportional to $G_{\bullet e}$ for a long time (up to ~ ms) and [$\bullet$H] also increases nearly linear at a rate proportional to $G_{\bullet H}$.

Except for affecting the concentrations of $\bullet e_{aq}^-$ and $\bullet$H, pH has a negligible effect on the production rates of other radiolysis products in Stage I. The levels of [$\bullet$OH] and the sum of ([$\bullet e_{aq}^-$] + [$\bullet$H]) reached near the end of Stage I when the secondary products, O_2, $\bullet O_2^-$ and $\bullet HO_2$, start to form (at~10^{-13} M) are nearly independent of pH. The concentrations of H_2O_2 and H_2 reached are also independent of pH.

At pH 3.0 [$\bullet$OH] and [$\bullet$H] quickly reach constant levels and remain at the steady state values in Stage II. The main difference in radiolysis products between pH 3.0 and 7.0 is the ratio of [$\bullet O_2^-$] to [$\bullet HO_2$] due to the fact that these pHs lie either side of the pKa of ($\bullet O_2^-$ + $H^+ \leftrightarrows \bullet HO_2$) (4.5 at 25 ^{o}C). This results in a very small decrease in [$\bullet$H], [H_2] and [H_2O_2] and a very small increase in [O_2] but negligible effect on [$\bullet$OH] in Stage II.

In Stage II the sums of the concentrations of acid-base pairs of the radicals, ([$\bullet e_{aq}^-$] + [$\bullet$H]) and ([$\bullet O_2^-$] + [$\bullet HO_2$]), are the same at pH 3.0 and 7.0. These results further confirm that at pH << pKa of $\bullet$H the net rates of the decomposition reactions of $\bullet$OH and $\bullet$H in Stage II quickly reach the net rates of their radiolytic production, according to equations (5.17 and 5.18). In turn, the rate of the decomposition of $\bullet$OH and $\bullet$H controls the rate of secondary

products and additional production of H_2O_2 and H_2 (equations 5.21 and 5.22). Thus, pH has a negligible effect on the overall radiolysis behaviour at pH < pKa of •H.   Similarly, the differences in Stage III between the radiolysis product concentrations at pH 3.0 and 7.0 are negligible.

At pH 10.6, by the time the secondary products start to form at a substantial rate near the end of Stage I the concentration of $•e_{aq}^-$ reaches a much higher level (nearly the same level as that of •OH). This has a significant consequence. At the onset of Stage II when the concentrations of the secondary products start to increase rapidly $[•e_{aq}^-]$ and [•H] start to decrease and [•OH] initially reaches steady state but then quickly starts to decrease. The decrease in the concentrations of $•e_{aq}^-$ and •OH accompanies increases in the concentrations of both the primary molecular products (H_2 and H_2O_2) and the secondary products (O_2 and $•O_2^-$). These behaviours are the result of a catalytic cycle:

$$O_2 \ + \ •e_{aq}^- \ \rightarrow \ •O_2^- \tag{5.25}$$

$$•OH \ + \ •O_2^- \ \rightarrow \ O_2 + \ OH^- \tag{5.26}$$

These cyclic reactions regenerate O_2 while continuously removing $•e_{aq}^-$ ($+ \ H^+ \leftrightarrows •H$) and •OH. Since the secondary products are produced by the reactions of •H and •OH (reactions 5.10 to 5.16), the net effect is a steady conversion of reactive radical species, $•e_{aq}^-$ ($+ \ H^+ \leftrightarrows •H$) and •OH to less reactive H_2, O_2 (and $•O_2^-$) and H_2O_2. The negative slopes in the log [i] vs log t for $•e_{aq}^-$ and •OH at longer times are the same as the positive slopes for H_2, O_2 (and $•O_2^-$) and H_2O_2. The absolute values of these slopes are slightly less than 1.0. Eventually the radiolysis system at pH 10.6 also reaches steady state, but this occurs at a

much later time than at lower pHs due to the slow reactions of the more stable molecular products. At pH 7.0, the cyclic reactions do not progress as effectively and the changes occur more slowly.

The effect of pH on the radiolysis product behaviour at 25 $^{\circ}$C is summarized in Figure 5.3 at three different times 1 ms, 1 s and 100 s. The concentrations of radiolysis products (or sum of $[\bullet H] + [\bullet e_{aq}^{-}]$ for $\bullet H$ and $\bullet e_{aq}^{-}$) observed at 1 ms are nearly independent of pH. The pH starts to affect the concentrations of radiolysis products in Stage II when the secondary product concentrations are significant. At pHs > pK_a of $\bullet H$ at 25 $^{\circ}$C, the cyclic reactions between the primary radiolysis products and secondary products accelerate the removal of $\bullet OH$ and $\bullet e_{aq}^{-}$ without affecting O_2. The changes in $[\bullet OH]$ and $[\bullet e_{aq}^{-}]$, in turn, affect the concentrations of the molecular radiolysis products, H_2O_2, O_2 and H_2. Due to the catalytic cycles, the rates of increase in the concentrations of radiolysis products do not have simple time dependences (or reaction order) at longer times. Nevertheless, the concentrations of the molecular primary products are inversely related to those of the radical primary products at longer times independent of pH.
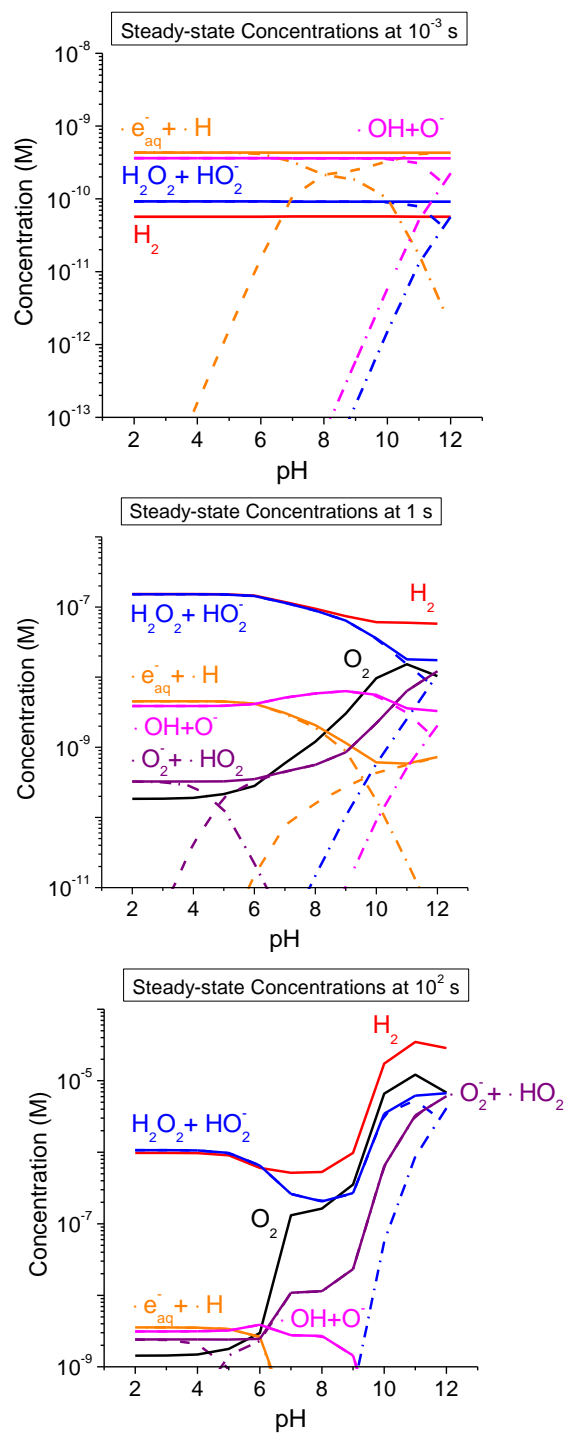
Figure 5.3: The concentrations of water radiolysis products obtained at three different times as a function of pH in deaerated water at 25 °C and at dose rate of 4.5 kGy·h^{-1}.

5.3.3   Effect of Temperature (T ≤ 250 ºC)

The effect of temperature on the radiolysis kinetics was examined at different $pH_{25^{o}C}$ values where $pH_{25^{o}C}$ is the pH value measured at 25 °C. As temperature increases the pH value (or $[H^+]$) at a given T changes due to the temperature dependence of the water dissociation constant (see $pK_w(T)$ in Table 5.1). The corresponding pH_T values as a function of temperature for various $pH_{25^{o}C}$ values are listed in Table 5.4.

Table 5.4: The equivalent pH values at different temperatures [13].

Temperature (^{o}C)	$pH_{25^{o}C}$ 3.0	$pH_{25^{o}C}$ 7.0	$pH_{25^{o}C}$ 10.6
25	3.0	7.00	10.6
75	3.0	6.30	9.3
100	3.0	6.10	8.85
150	3.0	5.82	8.24
200	3.0	5.65	7.91
250	3.0	5.60	7.8
300	3.0	5.67	7.94
350	3.0	5.96	8.52

The time-dependent behaviour of radiolysis product concentrations at $pH_{25^{o}C}$ 7.0 at 25, 150 and 250 °C are shown in Figure 5.4. The three radiolysis kinetic stages observed at 25 °C are all present at the higher temperatures.
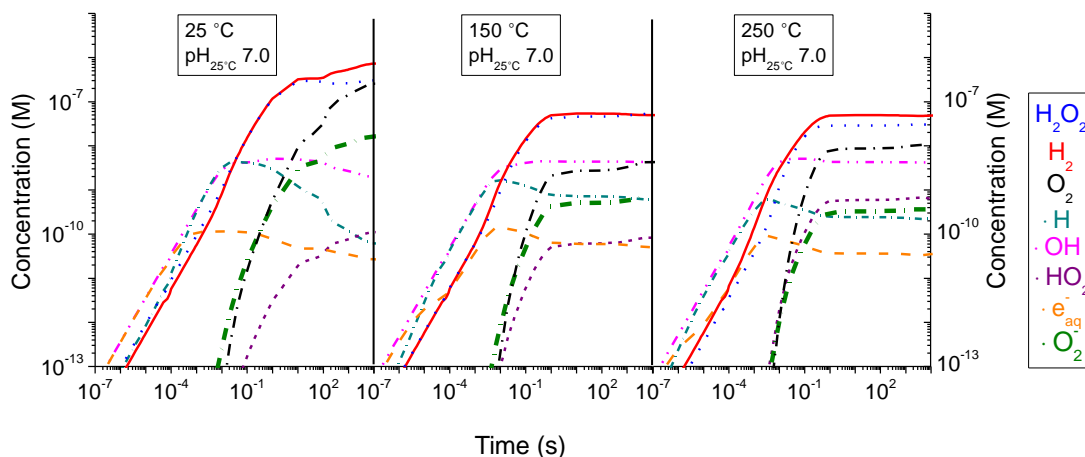
Figure 5.4: Time-dependent behaviour of radiolysis product concentrations at pH$_{25}^{o}$C 7.0 at 25, 150 and 250 °C.

At all temperatures the concentrations of the primary radiolysis products (except for •e$_{aq}^-$ and •H, see discussion below) increase linearly with time in Stage I, according to equation (5.7). The results show that temperature affects the radiolysis kinetics in Stage I through its effect on the primary G-values and water density. The primary radiolytic production rate constants $(10^{-6} \cdot G_i(T) \cdot \rho(T) \cdot D_R)$ are plotted as a function of temperature in Figure 5.6. The figure shows that temperature has negligible effect on the radiolytic production rate constants except for that of H$_2$O$_2$ and, hence, the time dependent behaviour of the radiolysis products in Stage I. For H$_2$O$_2$ the radiolytic production rate constant decreases by a factor of 3 when temperature increases from 25 ^{o}C to 300 ^{o}C.

Another influence of temperature in Stage I is its effect on the forward reaction of •e$_{aq}^-$ + H$^+$ ⇆ •H. This reaction occurs at a faster rate at a higher temperature and this results in an increase in [•H] at an earlier time. Thus, the net production rate of •H becomes closer

to the sum of the primary radiolytic production rates of $\bullet e_{aq}^-$ and $\bullet H$ at an earlier time, according to equation (5.24).

The sum of the primary radiolytic production rate constants for $\bullet e_{aq}^-$ and $\bullet H$ is also illustrated in Figure 5.5. At sufficiently high temperatures where the rate of the reverse reaction is also very fast, the acid-base equilibrium of ($\bullet e_{aq}^- + H^+ \leftrightarrows \bullet H$) is established very quickly. The ratio of the net production of $\bullet e_{aq}^-$ and $\bullet H$ is determined by the product of the equilibrium constant, pH and the sum of $\left(G_{\bullet H}(T) + G_{\bullet e}(T)\right)$:

$$\frac{d[\bullet H]}{dt} \approx 10^{-6} \cdot \left(\frac{K_{eq} \cdot [H^+]}{1 + K_{eq} \cdot [H^+]}\right) \cdot \left(G_{\bullet H}(T) + G_{\bullet e}(T)\right) \cdot \rho(T) \cdot D_R \tag{5.27}$$

$$\frac{d[\bullet e]}{dt} \approx 10^{-6} \cdot \left(\frac{1}{1 + K_{eq} \cdot [H^+]}\right) \cdot \left(G_{\bullet H}(T) + G_{\bullet e}(T)\right) \cdot \rho(T) \cdot D_R \tag{5.28}$$

The relationship between the $\left(G_i(T) \cdot \rho(T)\right)$ and the production rate of a species in Stage I can be seen from the concentrations observed at 0.1 ms (Stage I) as a function of temperature in Figure 5.6. The concentrations show the temperature dependences expected from the primary radiolytic production rate constants. That is, the concentration of $\bullet H$ at 0.1 ms has the same temperature dependence as the sum of the rate constants for the primary production of ($\bullet e_{aq}^- + \bullet H$) as discussed above. The concentrations of other species have the same temperature dependences as their respective production rate constants.
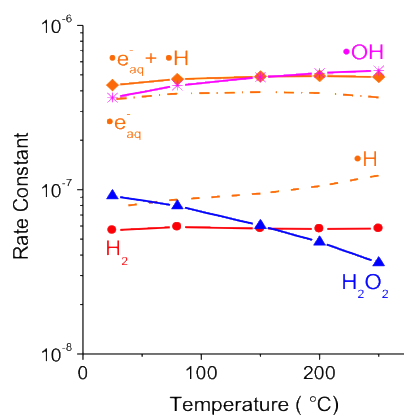
Figure 5.5: The primary radiolytic production rate constants
$(10^{-6} \cdot G_i(T) \cdot \rho(T) \cdot D_R)$ **as a function of temperature at a dose rate of**
4.5 kGy·h^{-1}.
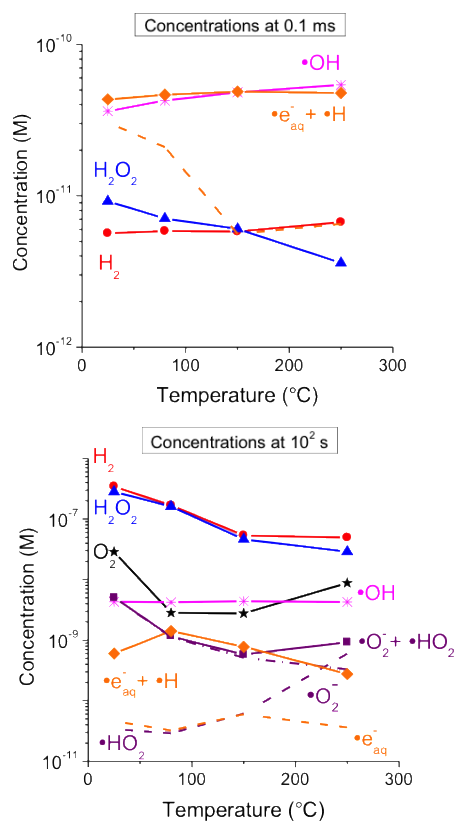
Figure 5.6: The production rate of species in Stage I (0.1 ms) and Stage II
(100 s), as a function of temperature at a dose rate of 4.5 kGy·h^{-1} at
neutral pH.

As the concentration of •H increases with time in Stage I, the rate of the removal reaction of •H (•H + •H $\leftrightarrows$ H$_2$) increases and approaches that of its production rate. As described earlier, this reaction results in the production of H$_2$ temporarily. The concentrations of •OH, H$_2$O$_2$ and H$_2$ all reach sufficiently high levels at the end of Stage I such that their reactions with each other produce the secondary products, •O$_2^-$, •HO$_2$ and O$_2$ via reactions of (5.10) to (5.16) at substantial rates. The more reactive radical, •H, reaches a steady state slightly faster than the less reactive •OH, and this difference is more pronounced at a higher temperature. This difference affects the kinetic behaviour of the secondary products at the beginning of Stage II and hence the overall radiolysis behaviour at longer times.

In Stage II when [•OH] is near steady state, [H$_2$] and [H$_2$O$_2$] continue to increase at all temperatures. In Stage II the concentration of •OH is nearly independent of temperature and constant with time, while [•H] is lower at a higher temperature and decreases with time. The temperature dependence of [•H] and [•OH], in turn, affects the net production rates of the secondary products •O$_2^-$, •HO$_2$ and O$_2$. The concentrations of the secondary products increase at faster rates at a higher T, and consequently the whole system reaches steady state (Stage III) faster at a higher T. At T $\geq$ 150 °C the system reaches steady state in less than 1 s.

The effect of temperature on the steady-state concentrations reached at 100 s (Stage III) at pH$_{25^\circ C}$ 7.0 are shown in Figure 5.6. Temperature affects the rates of many aqueous phase reactions and the net effect on the steady-state concentrations of individual species in Stage III is not easily formulated. Nevertheless, we can see that the steady-state concentrations of the primary radicals, [•OH] and ([•e$_{aq}^-$] + [•H]) are nearly independent of

temperature. The concentrations of the secondary radical products ($[\bullet O_2^-] + [\bullet HO_2]$) decrease slightly, by a factor of 2 when temperature increases from 25 °C to 250 °C. Temperature has the most effect on the molecular products. The concentration of H_2O_2 decreases steadily with increasing temperature (by an order of magnitude when temperature increases from 25 °C to 250 °C). The concentrations of H_2 and O_2 also decreases steadily with increasing temperature up to 150 °C, after which $[H_2]$ remains nearly constant with temperature whereas $[O_2]$ increases rapidly with temperature.

The model calculation results on the effect of temperature at $pH_{25°C}$ 10.6 are shown in Figure 5.7, and those on the effect of pH at 150 °C and 250 °C is shown in Figure 5.8. These results show that the effect of pH diminishes as temperature increases. The results obtained at $pH_{25°C}$ 7.0 (Figure 5.2) and at $pH_{25°C}$ 10.6 (Figure 5.7) show that at a given $pH_{25°C}$, at the onset of Stage II when the secondary product concentrations are significant the ratio of $[\bullet OH]$ and $[\bullet e_{aq}^-]$ increases with temperature. As this ratio increases it is more difficult to establish the cyclic reactions (reactions 5.24 and 5.25) that accelerate the removal $\bullet OH$ and $\bullet e_{aq}^-$ without affecting O_2 even at pHs > pK_a of $\bullet H$. Thus, the cyclic reactions that we see at pH 10.6 at room temperature are no longer established at temperatures $\geq$ 150 °C. At high temperatures, the main effect of pH is still via the acid-base equilibrium of $\bullet e_{aq}^- + H^+ \leftrightarrows \bullet H$, but all the aqueous phase reactions become faster and the whole radiolysis system reaches steady state before the catalytic cycle is established.
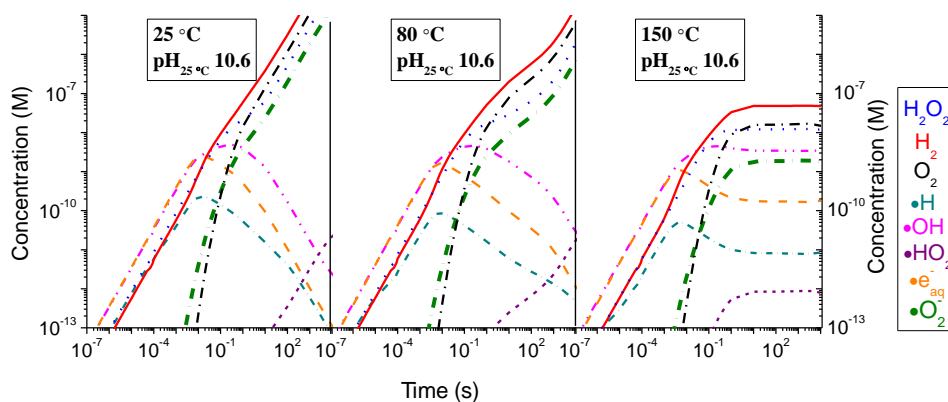
Figure 5.7: Time-dependent behaviour of radiolysis product concentrations at pH$_{25\,°C}$ 10.6 at 25 °C, 80 °C and 150 °C.
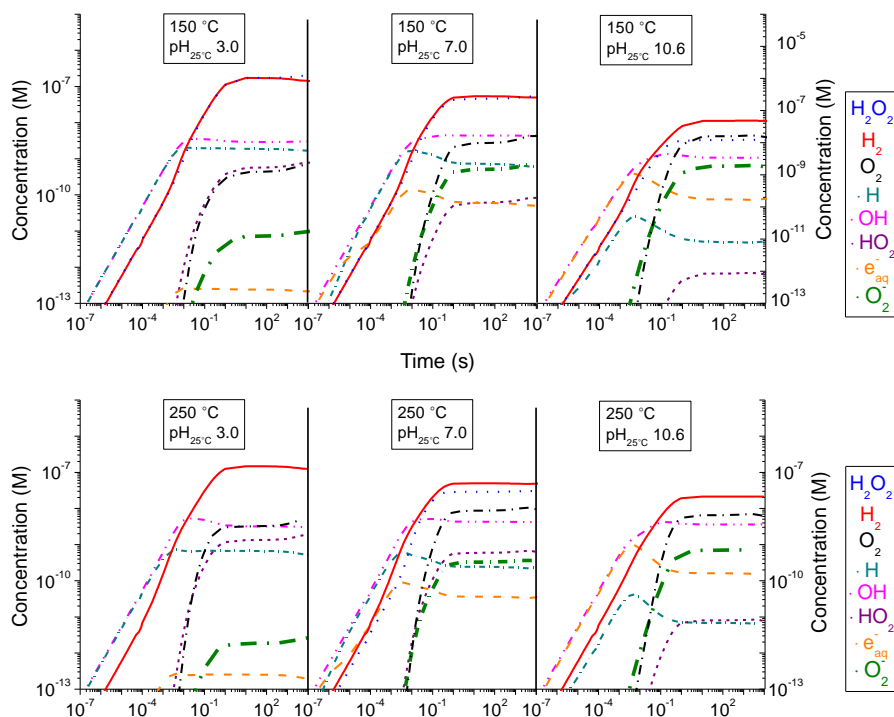
Figure 5.8: The concentration of water radiolysis products as a function of irradiation time at pH$_{25\,°C}$ 3.0, 7.0 and 10.6 in deaerated water at 150 °C and 250 °C and at a dose rate of 4.5 kGy·h^{-1}.

5.4　Conclusion

The γ-radiolysis of liquid water for a given set of conditions (pH, temperature and dose rate) the concentrations of radiolysis products show three distinct stages over the time span of 0 to 10^4 s. In Stage I (< 1 ms), in all cases, the concentration of a radiolysis product increases linearly with time at a rate determined by primary radiolytic processes, except for $\bullet e_{aq}^-$. The concentrations of the less reactive radicals, $\bullet H$ and $\bullet OH$, increase for a longer time before they reach steady state in Stage II. In Stage II, concentrations of the secondary products, $\bullet O_2^-$, $\bullet HO_2$ and O_2, start to accumulate at very fast rates and the concentrations of the primary molecular products, H_2 and H_2O_2, continue to grow almost linearly with time at this stage. The whole radiolysis system approaches steady state (Stage III) when the net rate of H_2O_2 and H_2 decomposition reactions become equal to the net rates of their production.

We have presented that for γ-radiolysis of liquid water, the net production rates of radiolyis products in Stage I depend mainly on their primary radiolytic production rates. In this regard, the production rates of $\bullet e_{aq}^-$ and $\bullet H$ should be considered together due to the fast forward reaction between them. We have shown that temperature has negligible effect on the primary radiolytic production rates; the greatest change occurs for H_2O_2 but even then, the rate decreases only by a factor of 2 when the temperature increases from 25 °C to 300 °C. However, at later stages (> ms) as the concentrations of the primary molecular species and the secondary products increase their reactions become progressively more important in controlling the concentrations of the radiolysis products. At higher temperatures, the whole radiolysis system reaches steady state at a slightly faster rate due to an increase in chemical

reaction rates.

The pH affects the $[\bullet e_{aq}^-]$ and $[\bullet H]$ at very early times in Stage I via the acid-base equilibrium of $\bullet e_{aq}^- + H^+ \leftrightarrows \bullet H$. At a $pH_{25^oC} > pKa$ of $\bullet H$, at temperatures below ≤ 80 °C, $[\bullet e_{aq}^-]$ increases to a level similar to that of $[\bullet OH]$ by the time when the secondary products are formed at substantial levels. At such conditions cyclic reactions between $\bullet e_{aq}^-$ and $\bullet OH$, and secondary products can accelerate the removal of $\bullet e_{aq}^-$ and $\bullet OH$ without affecting the secondary products. Due to the catalytic cycles, pH can have significant effect on the behaviour of radiolysis products in Stage II and Stage III. Thus, at temperatures ≤ 80 °C, the radiolysis kinetics behaviour in Stage II at pH 10.6 is markedly different from the behaviour observed at lower pHs and steady-state is reached at a longer time. Nevertheless, the effect of pH becomes less significant as temperature increases.

5.5   References

[1]   S. Leistikow, "Isothermal Steam Corrosion of Commercial Grade Austenitic Stainless Steels and Nickel Base Alloys in Two Technical Surface Conditions", Proceedings of the Fourth International Congress on Metallic Corrosion, Amsterdam, Netherlands, September 7-14, 1969.

[2]   J.W.T. Spinks, R.J. Woods, "An Introduction to Radiation Chemistry", 3rd Ed., Wiley-Interscience, New York, 1990.

[3]   J.C. Wren, Steady-State Radiolysis: Effects of Dissolved Additives, ACS symposium series, Nuclear Energy and Environment, American Chemical Society, Washington, DC, 2010, 271.

[4]   J.C. Wren, G.A. Glowa, "A Simplified Kinetic Model for the Degradation Of 2-Butanone in Aerated Aqueous Solutions Under Steady-State Gamma-Radiolysis", *Radiation Physics and Chemistry*, 58, 2000, 341.

[5]   J.C. Wren, J.M. Ball, "LIRIC 3.2 an Updated Model for Iodine Behaviour in the Presence of Organic Impurities", *Journal of Radiation Physics and Chemistry,* 60, 2001, 577.

[6] J. M. Joseph, B.S. Choi, P.A. Yakabuskie, J.C. Wren, "A Combined Experimental and Model Analysis on the Effect of pH and O_2(aq) on γ-radiolytically Produced H_2 and H_2O_2, *Radiation Physics and Chemistry*, 77, 2008, 1009.

[7] P.A. Yakabuskie, J.M. Joseph, C.R. Stuart, J.C. Wren "Long-term γ-radiolysis Kinetics of NO_3^- and NO_2^- Solutions", *Journal of Physical Chemistry A,* 115, 2011, 4270.

[8] P.A. Yakabuskie, J.M. Joseph, J.C. Wren, "The Effect of Interfacial Mass Transfer on Steady-state Water Radiolysis", *Journal of Radiation Physics and Chemistry*, 79, 2010, 777.

[9] O.P. Arkhipov, A.O. Verkhovskaya, S.A. Kabakchi, A.N. Ermakov, "Development and Verification of a Mathematical Model of the Radiolysis of Water Vapor", *Atomic Energy*, 103, 2007, 870.

[10] G.V. Buxton et al., "Critical Review of Rate Constants for Reactions of Hydrated Electrons, Hydrogen Atoms and Hydroxyl Radicals •OH/•O$^-$ in Aqueous Solution", *Journal of Physical and Chemical Reference Data*, 17, 1988, 513.

[11] A.J. Elliot, "The Temperature Dependence of the Rate Constants and Yields for the Simulation of the Radiolysis of Heavy Water", AECL Report-11073, Chalk River, Canada, 1994.

[12] G.A. Poskrebyshev, P. Neta, and R.E. Huie, "Temperature Dependence of the Acid Dissociation Constant of the Hydroxyl Radical", J. Phys. Chem. A, 106, 2005, 11488.

[13] A.V. Bandura, S.N. Lvov, "The Ionization Constant of Water over Wide Ranges of Temperature and Density", *Journal of Physical and Chemical Reference Data,* 35, 2006, 15.

[14] G.V. Buxton,N.D. Wood,S. Dyster, "Ionisation Constants of OH and HO_2 in Aqueous Solutions up to 200 °C", *Journal of Chemical Society, Faraday Transactions* I, 84, 1988, 1113.

[15] H. Shiraishi, G.R. Sunaryo, K. Ishigure, "Temperature Dependence of the Equilibrium and Rate Constants of Reactions Inducing the Conversion Between the Hydrated Electron and Atomic Hydrogen", Journal of Physical Chemistry, 98, 1994, 5164.

[16] T.F. Irvine, J.P. Hartnett, "Steam and Air Tables in SI Units", McGraw-Hill, Hemisphere, Washington, DC, 1976.

CHAPTER 6

Gamma-Radiolysis Kinetics of Water Vapour: The Model and the Model Predictions as a Function of Temperature and Pressure

6.1   Introduction

As described in earlier chapters, one of the research objectives was to develop a radiolysis kinetic model for supercritical water that can predict the concentrations of oxidants important for corrosion of in-core materials under the proposed supercritical water reactor (SCWR) coolant conditions. Our current understanding of chemical reaction kinetics in sub-critical and supercritical water is, however, not sufficient to construct a fully validated model for the radiolysis of SCW under continuous irradiation. Thus, we are approaching the modelling effort from two directions. We are developing models based on an existing liquid water radiolysis model [1–6] and an existing water vapour radiolysis model [7]. However, to extend the application of these models to SCW conditions with any confidence, the radiolysis kinetics of liquid water and water vapour as a function of temperature and pressure should be well understood. In Chapter 5, we have discussed the liquid water radiolysis model and presented model calculation results that examine how pH and temperature affect the liquid water radiolysis kinetics. In this chapter we present the water vapour radiolysis model and the model calculation results that examine how temperature and pressure affect the vapour water radiolysis kinetics.

6.2   Water Vapour Radiolysis Model

The model was constructed based on the reaction set used by Arkhipov et al. to determine water vapour chemistry under different types of radiation, from γ-irradiation to the fission products of uranium nuclei, at high temperatures (625 ℃) [7]. Similar to the liquid water radiolysis model, the water vapour radiolysis model contains the primary radiolytic production of water decomposition products and the vapour phase reactions of the radiolysis products with each other. The reactions and the rate constants included in the water vapour radiolysis model are listed in Table 6.1. The number of reactions in the model is significantly smaller than the number included in the liquid water radiolysis model since ionic species are not stable in the dilute vapour phase. Hence the reactions of those species are not included in the water vapour model. However, the oxygen atom is more stable in the vapour phase and hence the reactions of oxygen atom are added to the water vapour model.

Table 6.1: Reactions and their rate constants[1] as a function of temperature included in the water vapour radiolysis model.

ID#	Primary Radiolysis	Rate Constant[2] ($M \cdot s^{-1}$)
G1	$H_2O \rightarrow \bullet H$	$10^{-6} \cdot G_{\bullet H} \cdot \rho\,(T) \cdot D_R$
G2	$H_2O \rightarrow \bullet OH$	$10^{-6} \cdot G_{\bullet OH} \cdot \rho\,(T) \cdot D_R$
G3	$H_2O \rightarrow H_2$	$10^{-6} \cdot G_{H2} \cdot \rho(T) \cdot D_R$
G4	$H_2O \rightarrow \bullet O$	$10^{-6} \cdot G_{\bullet O} \cdot \rho\,(T) \cdot D_R$

	Gaseous Phase Reaction	**Rate Constant**[3]		
		$k_{ij}(T) = K_0 \cdot T^x \cdot \exp\left(-E_a/T\right)$		
		K_0	x	E_a
R1	$\bullet H + \bullet H + H_2O \rightarrow H_2O + H_2$	1.0×10^{13}	-1	0
R2	$\bullet H + \bullet OH + H_2O \rightarrow H_2O + H_2O$	1.4×10^{17}	-2	0
R3	$\bullet OH + \bullet OH + H_2O \rightarrow H_2O_2 +$ H_2O	6.0×10^{16}	-2	0
R4	$\bullet O + \bullet OH \rightarrow O_2 + \bullet H$	8.9×10^{9}	0	2.5×10^{2}
R5	$\bullet H + O_2 + H_2O \rightarrow H_2O + HO_2$	1.5×10^{12}	-0.8	0
R6	$\bullet H + \bullet HO_2 \rightarrow H_2 + O_2$	2.4×10^{10}	0.09	7.1×10^{2}
R7	$\bullet H + \bullet HO_2 \rightarrow \bullet OH + \bullet OH$	1.7×10^{11}	0	4.4×10^{2}
R8	$\bullet H + \bullet HO_2 \rightarrow H_2O + \bullet O$	2.5×10^{10}	0	7.0×10^{2}
R9	$\bullet HO_2 + \bullet HO_2 \rightarrow H_2O_2 + O_2$	1.8×10^{9}	0	0
R10	$\bullet H + \bullet O + H_2O \rightarrow \bullet OH + H_2O$	4.7×10^{12}	-1	0
R11	$\bullet H + H_2O_2 \rightarrow H_2O + \bullet OH$	1.0×10^{10}	0	1.8×10^{3}
R12	$\bullet OH + H_2O_2 \rightarrow H_2O + \bullet HO_2$	4.5×10^{9}	0	4.77×10^{2}
R13	$\bullet OH + H_2 \rightarrow H_2O + \bullet H$	2.5×10^{5}	0.48	1.7×10^{3}
R14	$\bullet OH + \bullet OH \rightarrow H_2O + \bullet O$	1.5×10^{6}	1.14	5.0×10^{1}
R15	$\bullet O + \bullet O + H_2O \rightarrow O_2 + H_2O$	1.9×10^{7}	0	9.0×10^{2}
R16	$\bullet O + H_2 \rightarrow \bullet OH + \bullet H$	51	2.67	3.16×10^{3}

R17	$H_2O_2 + H_2O \rightarrow \bullet OH + \bullet OH + H_2O$	2.5×10^{15}	0	2.41×10^4
R18	$\bullet H + H_2O \rightarrow H_2 + \bullet OH$	1.0×10^7	0	5.0×10^3

1 The reactions and the temperature-dependent rate constants are taken from refs [7,8].
2 The G-values and the density of water vapour at saturation ($\rho(T)$) as a function of temperature are presented in Tables 6.2 and 6.3, respectively.
3 All temperatures are in K. The bimolecular reaction rate constants are in units of $M^{-1}\cdot s^{-1}$ and the trimolecular reaction rate constants are in units of $M^{-2}\cdot s^{-1}$.

As for the liquid water model, the primary radiolytic processes occurring at short times are not modelled in detail. Instead, the radiolytic production of water decomposition products is modelled using the homogeneous primary radiolysis yields per unit absorbed energy (G-values) and the rate of radiation energy deposition into water:

$$\frac{d[i]}{dt} = 10^{-6} \cdot G_i(T) \cdot \rho(T) \cdot D_R \tag{6.1}$$

where $G_i(T)$ is the G-value for species i at temperature T in units of $\mu mol\cdot J^{-1}$, D_R is the absorbed radiation dose rate in units of $Gy\cdot s^{-1}$ ($J\cdot kg^{-1}\cdot s^{-1}$), and $\rho(T)$ is the density of water at T in units of $kg\cdot dm^{-3}$ (the factor of 10^{-6} provides for unit conversion).

The rate of change in the concentration of a chemical species, i, due to vapour phase reactions is described by the classical chemical reaction rate equation. For bimolecular reactions:

$$\frac{d[i]}{dt} = \sum_{l,m\rightarrow i} k_{lm} \cdot [l] \cdot [m] - \sum_j k_{ij} \cdot [j] \cdot [i] \tag{6.2}$$

where k_{lm} is the 2nd order rate constant for the reaction of species l and m producing species i in units of $M^{-1} \cdot s^{-1}$, and k_{ij} is the 2nd order rate constant for the reaction of species i and j in units of $M^{-1} \cdot s^{-1}$. In the vapour phase the elementary reactions can be strongly dependent on the water vapour pressure because this affects the three-body collision frequency (where the third body is normally a water molecule). We can note that in vapour phase combination reactions like R1, there must be a third body present to conserve momentum and hence the explicit recognition of the role of H_2O in the reaction. In the vapour phase the near neighbouring atoms assume this role and it is implicitly included in the bimolecular reaction rates for similar reactions. In the model this effect of water vapour pressure is incorporated in a 2nd order rate constant for the appropriate reaction. For a given species the overall rate law is then:

$$\frac{d[i]}{dt} = 10^{-6} \cdot G_i(T) \cdot \rho(T) \cdot D_R + \sum_{l,m \to i} k_{lm} \cdot [l] \cdot [m] - \sum_j k_{ij} \cdot [l] \cdot [m] \qquad (6.3)$$

The model rate parameters, the G-values and the rate constants of the vapour phase reactions are also those recommended by Arkhipov et al. [7] and are listed in Table 6.1 and 6.2. Note that the G-values for water vapour radiolysis are known to be independent of temperature and pressure (up to 1 MPa) [7,9]. In their review Arkhipov et al. provided the rate constants for the vapour phase reactions as a function of temperature using the following temperature dependence function [7]. The values of the parameters in this function are included in Table 6.1.

$$k_{ij}(T) = K_0 \cdot T^x \cdot \exp\left(\frac{-E_a}{T}\right) \qquad (6.4)$$

Table 6.2: Primary γ-radiolysis yields* of water vapour at 25-300 ^{o}C [7].

Water phase	H_2O	$\bullet e_{aq}^-$	H^+	$\bullet OH$	$\bullet H$	H_2	O	H_2O_2
Vapour	–0.74	0	0	0.63	0.74	0.055	0.11	0.0

* G-values in units of $\mu mol \cdot J^{-1}$.

6.3   Model Results

We have performed a series of model calculations to determine the effect of temperature on the net radiolytic production of H_2, O_2 and H_2O_2 using the water vapour model. These calculations were performed for saturated steam conditions and hence the density of water vapour increases with temperature. The saturation pressure and the density of water vapour as a function of temperature are listed in Table 6.3.

Table 6.3: Saturation pressure and vapour density of saturated steam as a function of temperature [10].

Temp (^{o}C)	Saturation Pressure (MPa)	Vapour Density $(g \cdot cm^{-3})$
25	0.003	2.31×10^{-5}
100	0.101	5.98×10^{-4}
150	0.476	2.55×10^{-3}
200	1.555	7.86×10^{-3}
250	3.976	1.996×10^{-2}
300	8.588	4.62×10^{-2}
350	16.529	0.114
374	22.064	0.322

6.3.1 Time Evolution of Radiolysis Product Concentrations

The model results obtained for γ-radiolysis of water vapour at 4.5 kGy·h^{-1}, at 25 °C, 150 °C and 250 °C are presented in Figure 6.1. Although the absolute concentrations of radiolysis products depend on temperature, their time-dependent behaviours are very similar at all temperatures. At a given temperature, the concentrations of the primary radiolysis products, •H, •OH, •O and H_2, all initially increase linearly with time (i.e. $[i] \propto t$) and then reach steady state. The chemically more reactive species reach steady state at earlier times. The most reactive species (•H) reaches steady state very early and its concentration is below 10^{-13} M at all temperatures studied. The less chemically reactive radicals, •OH and •O, take longer to reach steady state (< 0.1 ms and < 1 s, respectively at 150 °C), whereas the concentration of H_2 continues to increase over the 3-h period modelled.

The net rate of production of H_2 is higher than the rate of the primary radiolytic production of H_2 and close to the production rate of •H. This observation and that the early plateau of [•H] indicates that reaction R1 in Table 6.1 contributes significantly to the production of H_2:

$$\text{•H} + \text{•H} + H_2O \rightarrow H_2O + H_2 \tag{6.4}$$

At steady state, the total rate of removal reactions of •H is the same as its primary radiolytic production rate:

$$10^{-6} \cdot G_{\text{•H}}(T) \cdot \rho(T) \cdot D_R \approx \sum_j k_{\text{•H}-j}(T) \cdot [j] \cdot [\text{• H}] \tag{6.5}$$

In addition to reaction (6.4) •H is removed by other reactions (mainly with •OH (R2 in Table 6.2). Thus, not all, but a fraction, f_{H2}, of the •H formed by primary radiolytic processes will be used in producing H_2 via reaction (6.4). Since H_2 is chemically not very reactive, the net rate of its production can be approximated by the sum of the primary radiolytic production rate of H_2 and a fraction arising from •H:

$$[H_2] \approx 10^{-6} \cdot \left(G_{H2}(T) + f_{H2}(T) \cdot G_{•H}(T)\right) \cdot \rho(T) \cdot D_R \cdot t \tag{6.6}$$

The fraction, f_{H2}, depends on the rate of reaction (6.4) relative to other reactions that compete for •H, such as R2 in Table 6.1. The third body [H_2O] increases with temperature at saturation (the water density increases). This increases the rate of reaction R1 compared to other reactions that don't require a third body. Hence we see a higher [H_2] earlier at a higher temperature.

The concentrations of the secondary products, H_2O_2 and O_2, initially increase at 2nd order rates ([i] $\propto t^2$), but the rates of increase switch to linear rate ([i] $\propto t$) at longer times. At high temperatures ($\geq$ 150 °C) the times that these switches occur coincide with the times when the primary radicals, •OH and •O, reach steady state. This is because those radicals are the primary precursors to those molecular species. For example, for H_2O_2:

$$•OH + •OH + H_2O \rightarrow H_2O_2 + H_2O \tag{6.7}$$

The rate of H_2O_2 production from this reaction will be 1st order when [•OH] is at steady state, but higher order prior to the steady state. We can apply the same kinetic

analysis that was done for H_2 above to approximate $[H_2O_2]$ when $[\bullet OH]$ is at steady state. We then obtain,

$$10^{-6} \cdot G_{\bullet OH}(T) \cdot \rho(T) \cdot D_R \approx \sum_j k_{\bullet OH-j}(T) \cdot [\bullet OH] \cdot [j] \tag{6.8}$$

$$[H_2O_2] \approx 10^{-6} \cdot \left(f_{H2O2}(T) \cdot G_{\bullet OH}(T) \right) \cdot \rho(T) \cdot D_R \cdot t \tag{6.9}$$

where the fraction, f_{H2O2}, depends on the rate of reaction (6.7) relative to the rates of other competing reactions for $\bullet OH$, such as R2 in Table 6.1. Equation 6.9 explains the calculation results; $[H_2O_2]$ is higher at a higher temperature and at a given temperature $[H_2O_2]$ increases linearly with time except at very early times (Figure 6.1). We can apply a similar analysis for the net production for O_2.
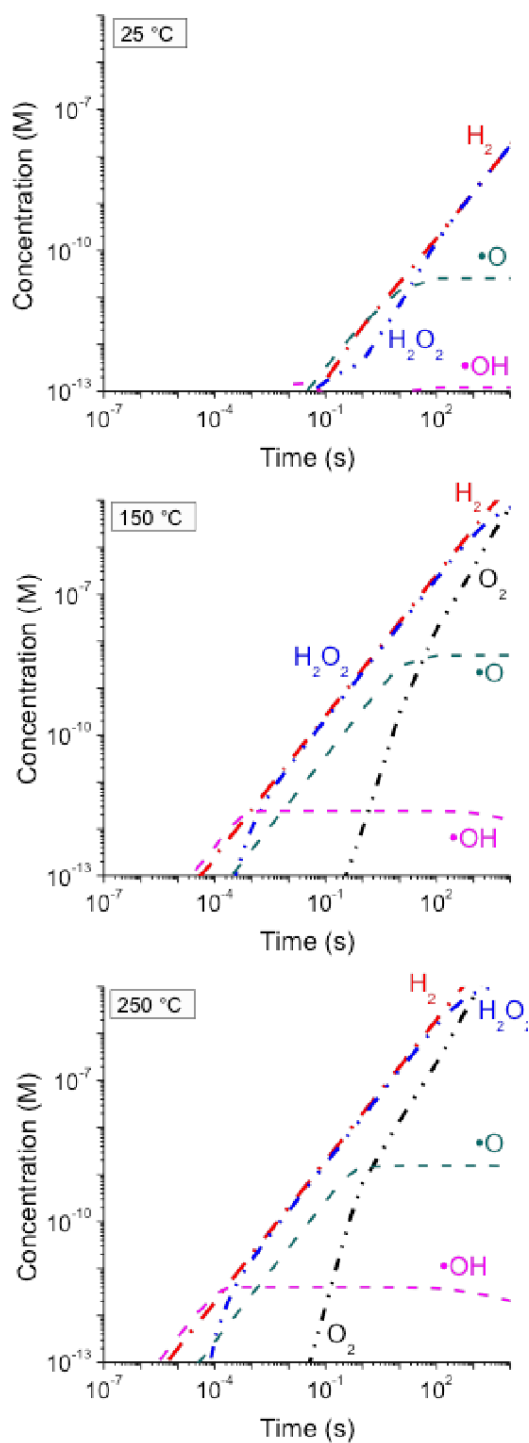
Figure 6.1: Time evolution of radiolysis product concentrations predicted by the vapor model at 25 °C, 150 °C and 250 °C at dose rate 4.5 kGy·h⁻¹.

6.3.2   Temperature Dependences Predicted by Vapor Radiolysis Model

Since the concentrations of different radiolysis products evolve at different rates with time, the effect of temperature is examined by comparing model predictions at two different times, 1 s and 1 h, in Figures 6.2 and 6.3. The water vapour model predicts the temperature dependence of the radiolysis product concentrations to be more noticeable at lower temperatures ($<$ 150 °C). The concentrations of all the molecular species plotted increase with temperature, but the increase is greatest a lower temperatures.

As temperature increases the concentrations of the reactive radicals reach steady state at earlier times. Consequently the concentrations of the less reactive molecular species start to increase at a linear rate at earlier time stages, and their concentrations can be approximated by equations (6.6) and (6.9). The net consequence of the increases in both the radiolytic production and gas phase reaction rates is that the concentrations of molecular species, H_2O_2, H_2, and O_2, all increase proportionally with $\rho(T) \cdot D_R$ when the temperature increases from 100 °C to 400 °C. At the lower temperatures the concentrations of the molecular species do not follow the simple linear dependence on $\rho(T) \cdot D_R$.

The concentration of H_2O_2 follows the same behaviour as [H_2] at short times for all temperatures, but deviates at longer times and higher temperatures. This is because the concentration of H_2O_2 is affected by its rate of thermal decomposition (a problem it does not share with H_2). Hence [H_2O_2] at 1 h does not follow the simple linear dependence on $\rho(T) \cdot D_R$.
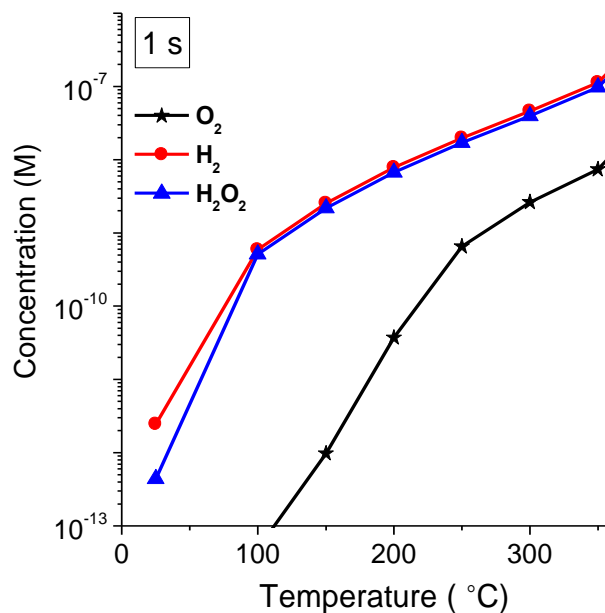
Figure 6.2: Radiolysis product concentrations as a function of temperature after 1 s of irradiation at a dose rate of 4.5 kGy·h^{-1}.
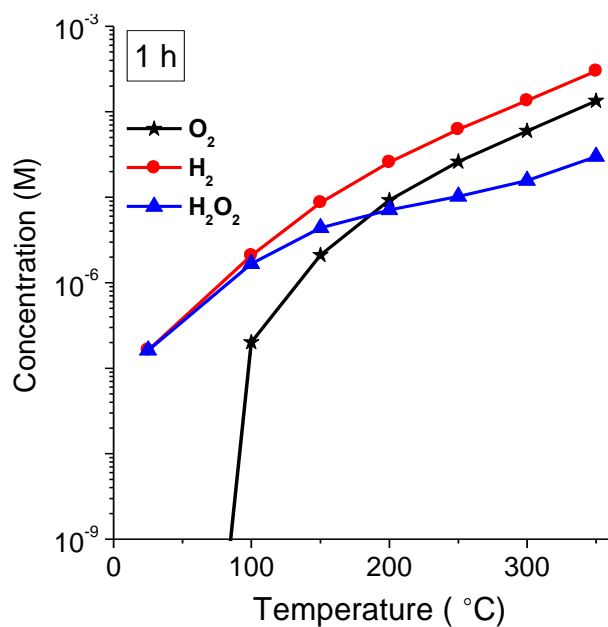
Figure 6.3: Radiolysis product concentrations as a function of temperature after 1 hour of irradiation at a dose rate of 4.5 kGy·h^{-1}.

6.3.3 Pressure Dependence of the Radiolysis of Vapor

The effect of water vapour density on the radiolysis kinetics was further investigated by performing the model calculations at 250 °C with different steam pressures (from 0.5 to 20 MPa), Figure 6.4. (Note that the saturation pressure at 250 °C is ≈ 4 MPa, so that the pressures > 4 MPa are hypothetical scenarios.) As discussed above, in the concentrations of the molecular products, H_2, O_2 and H_2O_2 increase nearly linearly with the water vapour density (note the logarithmic scale of the plot). On the other hand, the concentrations of the radical species, •H, •OH and •O, are nearly independent of water density. The [•H] actually appears to decrease slightly with increased pressure, but the concentration is so low that it may not be appropriate, at this stage, to consider the change significant.
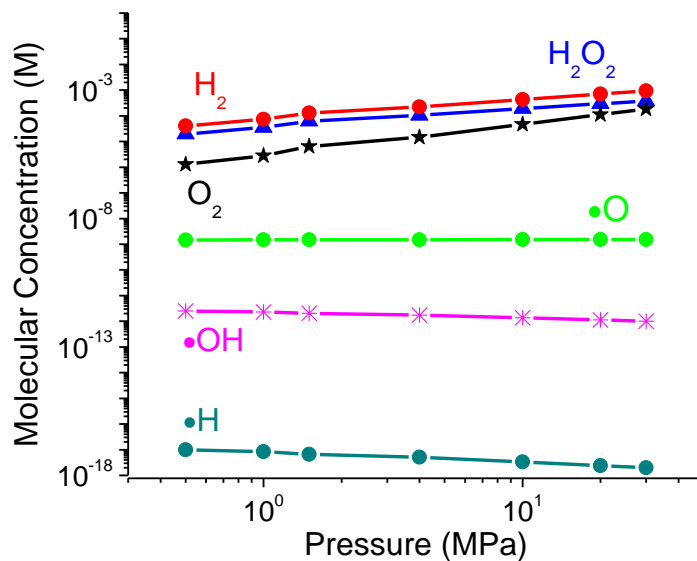
Figure 6.4: Radiolysis product concentrations as a function of pressure after 5 h of irradiation at 250 °C and at a dose rate of 4.5 kGy·h^{-1}.

6.4   Conclusion

We have performed a series of water vapour model calculations to determine the effect of temperature and pressure on the net radiolytic production of H_2, O_2 and H_2O_2. Water vapour model calculations show that while the absolute concentrations of radiolysis products depend on temperature, their time-dependent behaviours are very similar at all temperatures. At a given temperature, the concentrations of the primary radiolysis products, $\bullet H$, $\bullet OH$, $\bullet O$ and H_2, all increase linearly with time initially and then reach steady state. The chemically more reactive species (($\bullet H$) most reactive specie) reach steady state at earlier times whereas the less chemically reactive radicals, $\bullet OH$ and $\bullet O$, take longer to reach steady state.

The main production precursors of molecular products are the reactions of the primary radical species, $\bullet H$, $\bullet OH$ and $\bullet O$. Thus, the water vapour model predicts that the concentrations of H_2 and H_2O_2 start to increase at very early times at linear rates related to the G-values of the respective reactant radicals. As temperature increases the concentrations of the reactive radicals reach steady state at earlier times. Thus the concentrations of the less reactive molecular species start to increase at a linear rate at earlier times. The net consequence of the increases in both the radiolytic production and gas phase reaction rates is that the concentrations of molecular species, H_2O_2, H_2, and O_2, all increase consistently with $\rho(T) \cdot D_R$ when the temperature increases from 100 °C to 400 °C. At the lower temperatures the concentrations of the molecular species do not follow the simple linear dependence on $\rho(T) \cdot D_R$.

6.5   References

[1]   J.C. Wren, J.M. Ball, "LIRIC 3.2 an Updated Model for Iodine Behaviour in the Presence of Organic Impurities", *Journal of Radiation Physics and Chemistry,* 60, 2001, 577.

[2]   J.C. Wren, G.A. Glowa, "A Simplified Kinetic Model for the Degradation of 2-Butanone in Aerated Aqueous Solutions under Steady-State Gamma-Radiolysis", *Radiation Physics and Chemistry*, 58, 2000, 341.

[3]   J.M. Joseph, B.S. Choi, P.A. Yakabuskie, J. C. Wren, "A Combined Experimental and Model Analysis on the Effect of pH and O_2(aq) on γ-radiolytically Produced H_2 and H_2O_2, *Radiation Physics and Chemistry*, 77, 2008, 1009.

[4]   P.A. Yakabuskie, J.M. Joseph, J.C. Wren, "The Effect of Interfacial Mass Transfer on Steady-state Water Radiolysis", *Journal of Radiation Physics and Chemistry*, 79, 2010, 777.

[5]   P.A. Yakabuskie, J.M. Joseph, C.R. Stuart, J.C. Wren "Long-term γ-radiolysis Kinetics of NO_3^- and NO_2^- Solutions", *Journal of Physical Chemistry A,* 115, 2011, 4270.

[6]   A.J. Elliot, "The Temperature Dependence of the Rate Constants and Yields for the Simulation of the Radiolysis of Heavy Water", AECL Report-11073, Chalk River, Canada, 1994.

[7]   O.P. Arkhipov, A.O. Verkhovskaya, S.A. Kabakchi, A.N. Ermakov, "Development and Verification of a Mathematical Model of the Radiolysis of Water Vapor", *Atomic Energy*, 103, 2007, 870.

[8]   L.B. Ibraguimova, G.D. Smekhov, O.P. Shatalov, "Recommended Rate Constants of Chemical Reactions in an H_2 - O_2 Gas Mixture with Electronically Excited Species O_2 ($^1\Delta$), $O(^1D)$, $OH(^2\Sigma)$ Involved", Institute of Mechanics of Lomonosov Moscow State University, 2003.

[9]   J.W.T. Spinks, R.J. Woods, "An Introduction to Radiation Chemistry", 3rd ed., Wiley-Interscience, New York, 1990.

[10]   J.R. Cooper, Q. Mary, M.E. Road, S.I. Associates, Revised Release on the IAPWS Industrial Formulation 1997 for the Thermodynamic Properties of Water and Steam, The International Association for the Properties of Water and Steam, Lucerne, Switzerland, 2012.

CHAPTER 7

Radiolysis of Biphasic Liquid and Vapour Water System: Experimental and Model Simulation Studies

7.1   Introduction

The radiolysis kinetics of pure liquid water phase under γ-irradiation is difficult to study experimentally. Due to safety restrictions, *in-situ* monitoring of any radiolysis products as a function of time is practically impossible. This leaves *ex-situ* measurements of more stable products (H_2, O_2 and H_2O_2) as the only practical option. The concentrations of volatile gases such as H_2 and O_2 are more easily and more accurately determined by measuring their airborne concentrations in the gas phase than in the aqueous phase. The flow cell set up commonly used for radiolysis of liquid water using short-term pulses is also not optimum for a kinetic study, particularly at high temperatures where water radiolysis can very effectively couple with corrosion reactions of the flow tube materials. The corrosion reactions consume O_2 and H_2O_2 and produce H_2. Thus, corrosion affects their concentrations, the very parameters that we want to measure, and must be minimized. The problem becomes more significant at higher temperatures where corrosion rates are accelerated.

For this reason we have performed γ-radiolysis kinetic experiments in a static cell. Even with a static cell, the tests at high temperatures are very difficult since the surface reactions need to be minimized while leak-tight conditions during irradiation must be

maintained, and only *ex-situ* measurements can be performed with reasonable accuracies. We have described our efforts to achieve this balance in Chapter 4.

In this chapter we present the results of limited tests performed at 25 °C, 150 °C and 250 °C and model simulations of these experiments. The experiments were conducted in leak-tight cells which were partially filled with liquid water at room temperature before the cell was closed and heated to a desired temperature prior to irradiation. Thus, in our cell, liquid water is in contact with water vapour and the volume and concentration of steam in the cell is determined by the saturation pressure at the test temperature. At a given temperature, the radiolysis kinetics were studied by measuring the concentrations of H_2 present in the gas phase ($[H_2(g)]$) and the concentration of H_2O_2 present in the aqueous phase ($[H_2O_2(aq)]$) after irradiating the static radiolysis cell for different durations.

The radiolysis system consists of a liquid water and steam biphasic system in which the less reactive molecular species (H_2, O_2 and H_2O_2) can undergo liquid-gas interfacial transfer in addition to the complex radiolysis reactions in pure liquid and pure vapour phases as described in Chapters 5 and 6.

7.2   Experimental results

Gamma-radiolysis kinetic experiments were carried out at 25 °C, 150 °C and 250 °C. At 25 °C and 150 °C, the radiolysis kinetics were investigated at two $pH_{25^{o}C}$ values, 7.0 and 10.6 under deaerated conditions. For 250 °C, only the neutral pH was investigated. The experimental procedures and conditions have been described in detail in Chapter 3 and

Chapter 4. Briefly, the experiments at 25 °C and 150 °C were conducted in the leak-tight quartz cell whereas those at 250 °C were conducted in the gold-plated stainless-steel radiolysis cell designed particularly in our lab. For each experiment the radiolysis reaction cell was initially partially filled and purged with argon before the cell was sealed under a controlled environment in a glove box at room temperature. The whole radiolysis cell was heated to a desired temperature prior to the start of irradiation in the γ-cell. Upon termination of irradiation, the cell was cooled before the measurements of the concentration of H_2 in the gas phase and the concentration of H_2O_2 in the aqueous phase were performed. The concentration of H_2 was measured using gas chromatography and that of H_2O_2 was measured using the Ghormley method and UV spectrophotometry. Under a given set of pH and temperature conditions the irradiation time was varied from 30 min to 5 h. The absorption dose rate in these experiments varied during the period in which experiments were performed from 4.5 kGy·h^{-1} to 4 kGy·h^{-1}.

Tests to measure the concentrations of radiolysis products at high temperatures require that the experimental test cell includes a headspace. The measurements that can be performed are not the concentrations of radiolysis products in the liquid water phase but those of products that have become airborne during irradiation. Thus, simulation of laboratory experiments requires modeling of liquid-gas interfacial transfer of H_2 and O_2. The rate of interfacial mass transfer is easy to formulate but the rate coefficient is very specific to the thermalhydraulic condition of each system and hence the rate coefficient is normally an adjustable input parameter in a kinetic model.

Interfacial mass-transfer between the aqueous and gas phase is modelled using two fundamental parameters: k_{MT}, the overall mass transfer coefficient and H, the partition coefficient. The partition coefficient is given by the ratio of the concentration of a species in the liquid phase to the concentration in the gas phase at equilibrium at a given temperature [1]. The interfacial mass transfer rate coefficient is an input parameter in the model because of its dependence on thermalhydraulic conditions. In our model we typically use $k_{M(aq)} = 10^{-4}$ and $k_{M(g)} = 10^{-2}$ and calculate the overall mass transfer rate as

$$\frac{1}{k_{MT}} = \frac{1}{k_{M_{aq)}}} + \frac{H}{k_{M_{(g)}}} \tag{7.1}$$

where $k_{M(aq)}$ and $k_{M(g)}$ are aqueous-to-gas phase and gas-to-aqueous phase mass transfer coefficients respectively.

The partition coefficient used in the model has been defined as a function of temperature using the known thermodynamic properties of H_2 and O_2. The mass transfer rate coefficient $k_{M(aq)}$ was increased to a maximum value of 10^{-2} in some simulations (to match the reverse rate coefficient) to explore the change in the modeling predictions as a result of an increase in the $k_{M(aq)}$.

The experimental data and the model simulation results using the liquid radiolysis model (with two different values for $k_{M(aq)}$, 10^{-4} and 10^{-2}) and the water vapour radiolysis model at $pH_{25^{o}C}$ 7.0 and $pH_{25^{o}C}$ 10.6 are presented in Figure 7.1 and Figure 7.2 respectively. The liquid water radiolysis model simulates the time dependent radiolysis product behaviour

at both pHs very well at 25 °C. It also predicts the effect of pH on the radiolysis kinetics accurately.

Using the vapour model, the [H_2O_2] in the vapour phase was calculated and this was then converted to a concentration in the liquid phase using the number of moles present in the volume of the head space in the radiolysis cell at that particular temperature (0.009 L for radiolysis cell at 150 °C and 0.007 L for gold-plated radiolysis cell at 250 °C). At 150 °C, quartz radiolysis cell contains 8 ml of water at 25 °C (equals to 8.7 ml at 150 °C) and 10 ml headspace and the stainless steel gold plated radiolysis cell used for the experiments at 250 °C had 12 ml volume totally that contains 4 ml water at 25 °C (equals to 5 ml at 250 °C). At 250 °C most of the liquid water originally introduced into the test cell is present as water vapour and it is reasonable to consider the test cell volume to be largely filled with water vapour. There is actually quite good agreement between the equivalent concentrations of H_2O_2 determined by the water vapour model and the measured [$H_2O_{2(aq)}$] at both 150 °C and 250 °C.

Table 7.1: Calculated [H_2O_2] dissolved in liquid phase after radiolysis at a dose rate of 4.5 kGy·h^{-1} for 3 h (deaerated water at pH$_{25^o C}$ 7.0).

Temperature (°C)	[$H_2O_{2(aq)}$] From Vapour Model (mol·L^{-1})	Liquid Volume (L)	Vapor Volume (L)	[$H_2O_{2(aq)}$] Measured in Liquid Phase (mol·L^{-1})
150	7.27×10^{-6}	0.009	0.009	7.77×10^{-6}
250	9.73×10^{-6}	0.005	0.007	1.36×10^{-5}

The simulation results from the liquid water model start to deviate from experimental data as the temperature rises. As illustrated in Figure 7.1, experimentally measured [$H_2(g)$] and [$H_2O_2(aq)$] at 150 °C have at least one order of magnitude difference from liquid water model predictions and they become closer to vapour radiolysis model predictions as temperature increases.

The liquid model predicts [$H_2O_2(aq)$] to decrease significantly with increasing temperature and to be only 2×10^{-8} mol·L^{-1} at 250 °C. On the other hand, experimental measurements have shown an increase in [$H_2O_2(aq)$] with temperature and at 250 °C values for [$H_2O_2(aq)$], measured post-test, that are close to the detection limit have observed. This matches with the value predicted by the water vapour model at 250 °C, 1×10^{-5} mol·L^{-1}. Similar behaviour is seen for [$H_2(g)$]. Although [$H_2(g)$] experimental values for 150 °C are higher than those predicted by both water vapour and liquid water models, at 250 °C the experimental data clearly match the water vapour model predictions better. The same behaviour was seen for tests at $pH_{25^o C}$ 10.6. The liquid water model works well in predicting [$H_2(g)$] and [$H_2O_2(aq)$] at 25 °C but at 150 °C, both [$H_2(g)$] and [$H_2O_2(aq)$] are better predicted using the water vapour model.
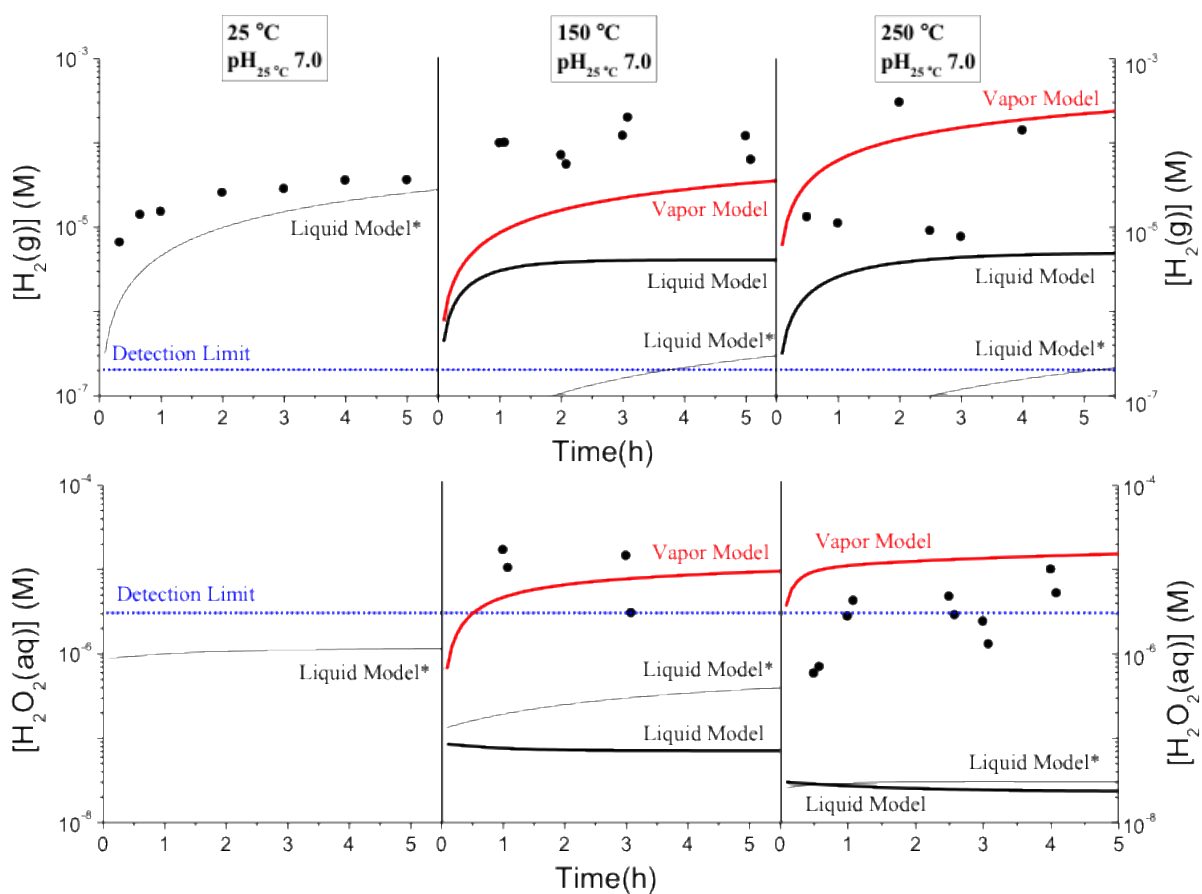
Figure 7.1: [H₂(g)] and [H₂O₂(aq)] as a function of irradiation time for deaerated water (pH 7.0) at 25 °C, 150 °C and 250 °C at a dose rate of 4.5 kGy·h⁻¹. The symbols represent the experimental data and the solid lines are model results (Liquid Model* uses $k_{M(aq)} = 10^{-4}$ and Liquid Model uses $k_{M(aq)}$ 10^{-2}).
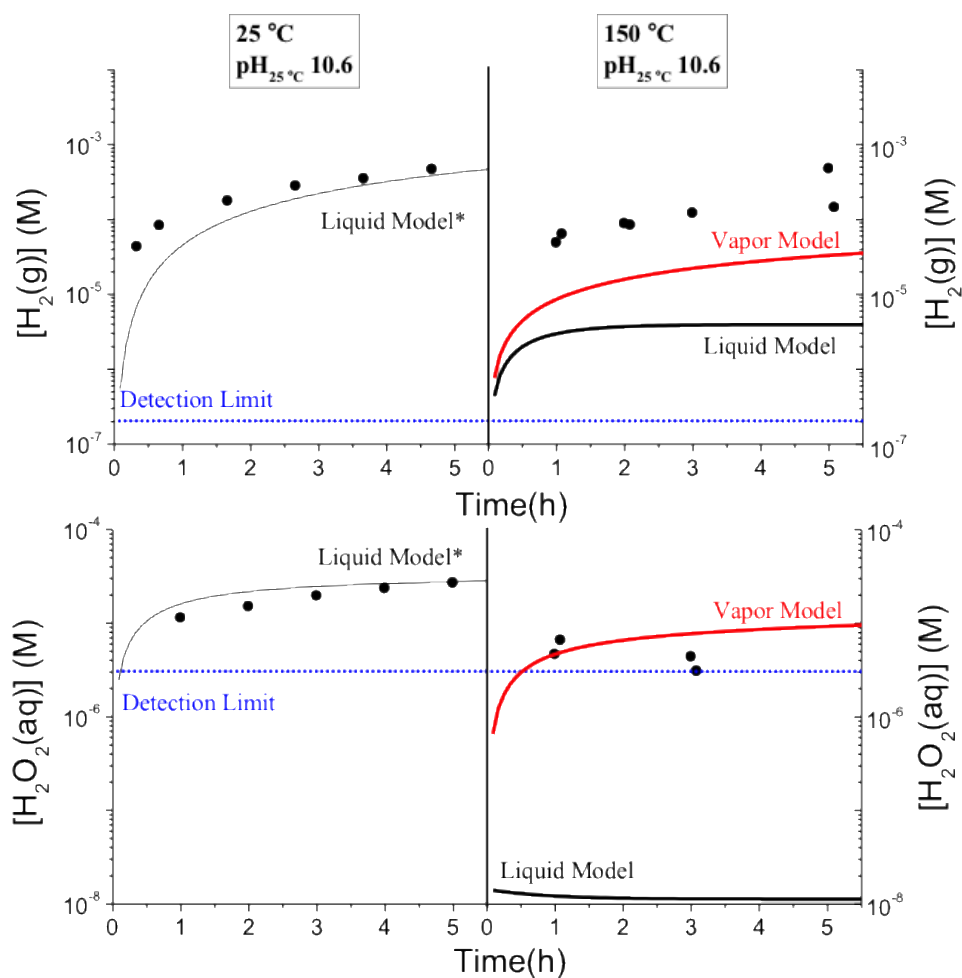
Figure 7.2: [H₂(g)] and [H₂O₂(aq)] as a function of irradiation time for deaerated water (pH 10.6) at 25 °C and 150 °C at a dose rate of 4.5 kGy·h⁻¹. The symbols represent the experimental data and solid lines are model results (Liquid Model* uses $k_{M(aq)} = 10^{-4}$ and Liquid Model uses $k_{M(aq)}$ 10^{-2})

7.3   Conclusion

In this chapter, experimental results from the radiolysis of biphasic liquid-vapour water system at 25 °C, 150 °C and 250 °C presented and compared with the model simulation results using the liquid and vapour radiolysis models. Model calculations efficiently reproduced the experimental results. As temperature increases the saturation pressure (water vapour density) in the headspace increases, and the production of the molecular radiolysis products, H_2, H_2O_2 and O_2 in the vapour phase dominates the net production in the biphasic system. The model simulation results show that the contribution from the radiolysis of liquid phase to the net production of H_2 and H_2O_2 in a leak-tight radiolysis cell is negligible at $T \geq 150$ °C. This suggests that at temperatures near critical region, when water approaches the supercritical fluid state, model predictions based on an extension to the low-pressure water vapour radiolysis model may be more useful. In the model simulations of the biphasic water system we have performed the calculations using each model individually.

7.4   References

[1]   P.A. Yakabuskie, J.M. Joseph, J.C. Wren, "The Effect of Interfacial Mass Transfer on Steady-state Water Radiolysis", *Journal of Radiation Physics and Chemistry*, 79, 2010, 777.

CHAPTER 8

Chemical Kinetics Model for the Gamma-Radiolysis of Supercritical Water

8.1   Introduction

There are plans to measure the corrosion of materials under supercritical water reactor (SCWR) conditions via in-reactor experiments [1]. Until these data are available, other approaches to predicting corrosion rates are being explored. One option is to use chemical kinetics modelling to predict the concentrations of oxidizing species in an SCWR. The model results can be used to plan out-of-reactor corrosion tests where the water chemistry is adjusted to mimic that expected in a reactor. Our current understanding of chemical reaction kinetics in sub-critical and supercritical water is not sufficient to construct a fully validated model for the radiolysis of SCW under continuous irradiation. To date, only one SCWR radiolysis model has been published. Yeh et al. [2] have modelled the radiolysis chemistry of an early SCWR conceptual design. While providing some valuable insights, their model made many simplifying assumptions that reduce its predictive value.

We have approached the modelling effort from two directions and are developing two chemical kinetics models: (1) a liquid radiolysis model (LRM) and (2) a vapour radiolysis model (VRM) for the continuous radiolysis of sub-critical and supercritical water. The liquid model (LRM) was constructed using the same reaction set used in the radiolysis model for liquid water [3–7] described in Chapter 5. The vapour model (VRM) uses the reaction set

developed by Arkhipov et al. for water vapour radiolysis [8] described in Chapter 6. However, in order to extend the applications of these models to radiolysis of sub- and supercritical water, the model rate parameters must be defined as a function of pressure and temperature in the ranges of subcritical and supercritical conditions. As discussed in Chapter 2, the solvent properties of water change rapidly with temperature and pressure in the subcritical (300 - 375 °C) and supercritical temperature regions. Solvent properties such as density, ionic product and viscosity have a considerable effect on homogeneous liquid and vapour reaction rates. Thus the changes in the solvent properties with T and P must be taken into account. Since these effects are not fully understood, we have used a two-pronged approach to the kinetics modeling coming from high density (liquid) and low-density (vapour) perspectives, and hence creating two models. Our aim is to have the models converge as they mature.

This chapter describes how the key model parameters values (G-values and rate constants) of the LRM and VRM were assigned, and presents preliminary predictions of the models for the time dependent chemistry for radiolysis at temperatures ranging from 250 °C to 400 °C. Hydrogen addition is used in conventional nuclear reactors to lower the oxidation potential of coolant water and reduce corrosion rates. Predictions of the effects of hydrogen addition on the production of oxidizing species in irradiated SCW are also presented.

8.2   SCW Radiolysis Kinetics Model

The sets of reactions in the LRM and the VRM are the same as those of the radiolysis models for liquid water and water vapour and listed in Table 5.1 in Chapter 5 and Table 6.1 in Chapter 6, respectively. To extend the application of these models to SCW conditions, the rate constants used in the models must be extrapolated from those known for low temperature liquid water (for the LRM) and from those known for steam (for the VRM).

8.2.1   Primary Radiolysis Yields, the G-values

There are few measured G-values for sub-critical and supercritical water [9] and the reported values have large uncertainties. However, examination of the G-values reported for liquid water as a function of temperature and for vapour water can provide insight into the effects of temperature and changes in the solvation properties of water on radiolysis yields. This understanding can then be used to estimate the G-values of individual species for γ-radiolysis of sub-critical and supercritical water.

Uncertainties exist for the G-values obtained for liquid water radiolysis at high temperatures owing to the challenge in making the requisite measurements. The uncertainties in the G-values of species that require indirect measurement techniques can be even greater. For the same reasons, a complete set of G-values is not available for SCW; they are often reported for the sum of radical species. For example, Katsumura et al. reported the G-value for the sum of ($\bullet e_{aq}^- + \bullet OH + \bullet H$) as a function of water density but did not give individual

radical G-values [10]. This makes it difficult to adapt the reported G-values for use in a chemical kinetics model that follows individual species.

The G-values for the radiolysis of liquid water as a function of temperature in the range from 25 °C to 350 °C have been thoroughly reviewed Elliot and Bartels [9]. In their review they also provided temperature-dependent polynomial functions for G-values that were formulated by polynomial fits to the available data in the literature. In the current version of the LRM model we have used their formulae and extrapolated their application to calculate G-values for a wider temperature range (up to 400 °C) as presented in Figure 8.1. Note that $\bullet e_{aq}^{-}$ and $\bullet H$ are in fast acid-base equilibrium and hence their individual G-values have large uncertainties. The G-values for the sum of these species combined are more reliable and hence these values are presented in Figure 8.1. The G-values of primary water radiolysis products at different temperatures are listed in Table 8.1.
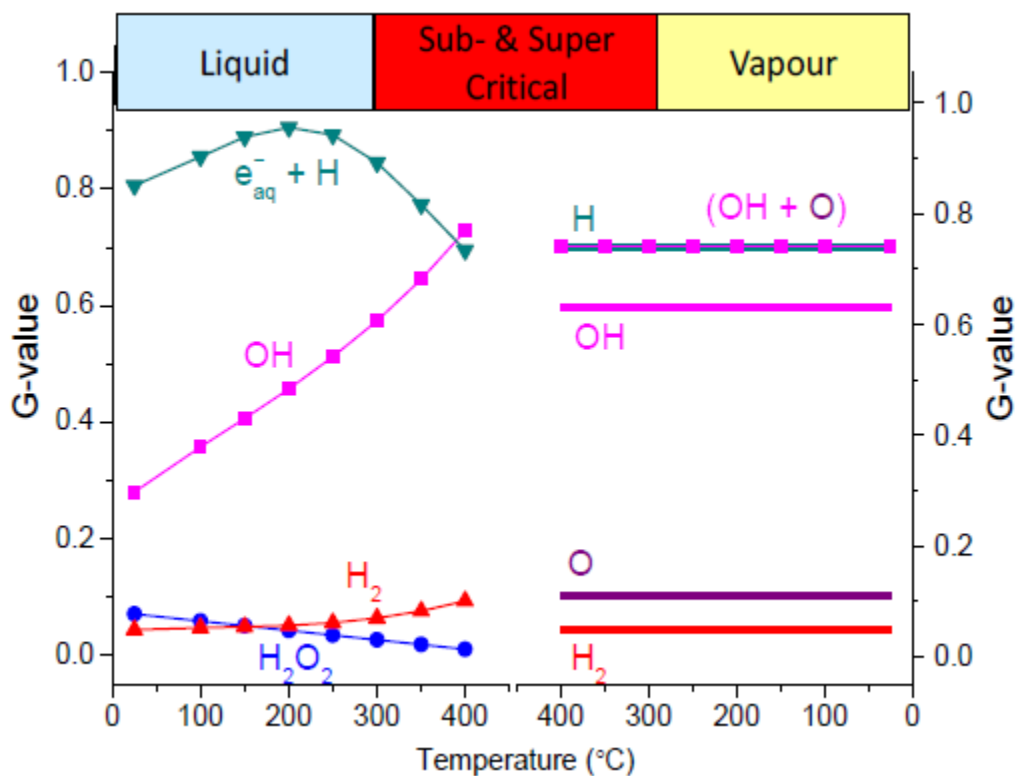
Figure 8.1: G-values as a function of temperature used in the LRM (left axis) and VRM (right axis). The temperature dependences of the G-values for the LRM were taken from ref [9]. The temperature independent G-values for the VRM were taken from ref [8].

In the first version of the VRM the G-values used by Arkhipov et al. [8] for water vapour radiolysis at low pressure were used without modification at sub-critical and supercritical temperatures, see Figure 8.1 and Table 8.1. In Figure 8.1, the sum of the G-values of •OH and •O is also shown and this sum coincides with the G-value of •H.

Table 8.1: Primary γ-radiolysis yields* as a function of temperature in LRM and VRM.

Water State	T (^{o}C)	H$_2$O	$\bullet e_{aq}^{-}$	$\bullet$H	$\bullet$OH	$\bullet$O	H$_2$	H$_2$O$_2$
LRM								
Liquid water** [9]	25	−0.41	0.26	0.06	0.27	0.0	0.04	0.07
	150	−0.51	0.33	0.08	0.41	0.0	0.05	0.05
	200	−0.54	0.35	0.09	0.46	0.0	0.05	0.04
	250	-0.58	0.35	0.12	0.51	0.0	0.06	0.035
	300	−0.61	0.34	0.15	0.57	0.0	0.06	0.02
	350	−0.69	0.32	0.21	0.65	0.0	0.08	0.02
	400	−0.75	0.27	0.29	0.73	0.0	0.09	0.01
VRM								
Vapour [8]	25 – 400	−0.74	0.0	0.74	0.63	0.11	0.05	0.0

* G-values are in units of μmol·J^{-1}.

** The G-values were calculated from the temperature-dependent formula provided in ref [9].

The G-values for liquid water radiolysis show a small dependence on temperature in the range from 25 °C to 250 °C; the G-value for water decomposition (G(−H$_2$O)) (Table 8.1) and the G-values for the production of the main decomposition products, $\bullet e_{aq}^{-}$ and $\bullet$OH, increase with temperature. This temperature dependence arises from decreases in the viscosity (η) and dielectric constant (ε_r), and an increase in the ionic product (pK$_W$) of water with temperature (See Chapter 2). The decrease in η will increase, while the decrease in ε_r will decrease, the escape probability of electrons from geminate recombination [11]. Due to

their opposite effects on the escape probability, the increase in $G(-H_2O)$ over the range from 25 °C to 250 °C is small (from 0.41 $\mu mol \cdot J^{-1}$ to 0.58 $\mu mol \cdot J^{-1}$) (Table 8.1). In comparison, the rate constant of a chemical reaction can increase by several orders of magnitude over the same temperature range. The increased rate of decomposition of H_2O results in increases in the G-values for the production of radicals ($\bullet e_{aq}^{-}$ and $\bullet OH$).

The $G(-H_2O)$ value changes more rapidly in the temperature range from 250 °C to 350 °C because the solvent properties of water change more rapidly in this range with temperature. At these temperatures ε_r is very small and ion mobility becomes the main factor affecting the rate of geminate recombination. Ion mobility increases with decreasing η and, hence, with an increase in temperature. Consequently the $G(-H_2O)$ and $G(\bullet OH)$ values continue to increase with temperature. However, the G-value for $\bullet e_{aq}^{-}$ starts to decrease for T > 200 °C because of changes in the ionic product (K_w) of water. The K_W increases (and $pK_w = -\log K_w$ decreases) slowly with increasing temperature up to 200 °C, but then decreases as the temperature rises above this point (Figure 2.1). The change in K_w with temperature becomes faster near the critical point and above the critical point the ionic product is many orders of magnitude less than the value for ambient water (10^{-23} at 375 °C and 24 MPa compared to 10^{-14} at 25 °C and 0.1 MPa) [12–14].

In using the Elliot and Bartels formulae to estimate the G-values at sub- and supercritical temperatures we have ignored the effect of this dramatic change in K_w for the model. This should lead to an overestimate of the G-value of $\bullet e_{aq}^{-}$ and an underestimate of the G-value of $\bullet H$ at temperatures near and above the critical temperature. Similarly, in

using the G-values from water vapour radiolysis for sub-critical and supercritical temperatures we have ignored the effect of changes in density near the critical temperature that lead to changes in solvent properties. The impact of such estimation errors is being explored by performing model sensitivity analyses but the results yet to be reported.

It is interesting to note that even with the known simplifications in our estimates and extrapolations, the G-values of the reducing radicals ($\bullet e_{aq}^- + \bullet H$) and the oxidizing radical $\bullet OH$ in the LRM and those of $\bullet H$ and ($\bullet OH + \bullet O$) in the VRM converge to very similar values at 400 °C (Figure 8.1). This may be fortuitous, or it may be due to the fact that, even at supercritical pressures, the density of water does not have a direct impact on the G-values for low LET γ-radiolysis. The Monte Carlo simulations performed by the Jay-Gerin group at the University of Sherbrooke also show that G-values (within 10^{-7} to 10^{-8} s) are independent of the density of SCW [15]. We can see that they change by less than a factor of 2 when the density of water changes from 2.3×10^{-5} g/cm^3 (vapour) to ~1 g/cm^3 (liquid water at 25 °C). It would appear that for pressures less than ~25 MPa, the main effect of water density on the G-values is its influence on the interaction of radiolysis product species between the spurs of a radiation track. The maximum value that G($-H_2O$) can have is 0.80 µmol·J^{-1}. This value is a limit set by the ratio of the absorbed energy per molecule to the ionization energy of a water molecule. The G($-H_2O$) value for water vapour radiolysis is close to this limit value. It is possible that water vapour at high densities and high temperatures can have some other influences on the physics and chemistry of the interaction of fast electrons with water molecules and the decay of excited species in the radiation spurs. This can be investigated in developing further generations of the VRM.

8.2.2 Homogeneous water phase reaction rate constants

As discussed in Chapter 5, a chemical reaction rate constant for a system at thermal equilibrium can normally be expressed using the Arrhenius equation:

$$k_{ij}(T) = A_{ij}(T) \cdot \exp\left(-\frac{E_A}{RT}\right) \tag{8.1}$$

where E_A is the activation energy. The activation energy should be independent of temperature over the range of temperatures of interest for our model since most species will be in ground molecular energy states. Thus, the activation energy that is known for a reaction at low temperatures should be valid at SCW temperatures. Nevertheless, to extrapolate the rate constants observed in lower temperature liquid water and water vapour, knowledge of activation energies alone is insufficient to predict rate constants as a function of temperature. We need to know the dependence of the pre-exponential factor on temperature, pressure, and solvent properties.

Excellent reviews of the rate constants are available for reactions in water vapour [8] and in liquid water [9]. These reviews provide the rate constants as a function of temperature in their respective phases, as described in Chapters 5 and 6. For the gas phase reaction rate constants, the temperature dependence was obtained from the best fit of the data using a general pre-exponential function [8] :

$$A_{ij}(T) = A_{ij}^{o} \cdot T^{n} \tag{8.2}$$

For the rate constants in the liquid phase, the temperature dependence of the pre-exponential function, A_{ij} (T), was obtained using mathematical functions provided by Elliot and Bartels [9] for a number of temperatures from 20 °C to 350 °C.

The version.0 of the models use the temperature-dependent functions of the rate constants provided by these reviews to extrapolate for rate constants at sub- and supercritical temperatures. The temperature dependences of the rate constants are empirically derived functions. In using these functions the impacts of the temperature dependent properties of water (such as viscosity) on factors such as the diffusion rate is not specifically considered. This simplification was likely to be the main source of uncertainties in calculations using the version.0 models. The uncertainties in the validity of the assumptions for the rates constants as a function of temperature is one of the driving forces for the development of parallel models starting from low and high water densities. Examination of the differences in the models and their predictions can help to identify the main sources of error and the reactions that are most important.

8.3   Model Simulation Results

In our preliminary calculations we started with a given set of initial molecular species concentrations, e.g., just pure H_2O. The irradiation source was 'turned on' and the evolution of the system chemistry was followed for 10^4 s. This partially simulates the experience in a nuclear reactor where coolant water would enter the reactor core and be exposed to a high flux of ionizing radiation for a short time. The residence time of the coolant in the SCWR

core is expected to be on the order of seconds based on existing reactor designs. The γ-radiation field in a reactor core is expected to be on the order of a few 1000 kGy·h^{-1} [16]. Coolant before entering the core and after exiting will be exposed to much smaller radiation fields (orders of magnitude lower) and the effects of such changes in radiation exposure rates are not considered in our preliminary calculations. The radiation field in the reactor core will also include high fluxes of neutrons and β-particles (most α-radiation will be confined to the nuclear fuel and fuel cladding). Again, for the sake of simplification, only the chemistry induced by γ-radiation is considered in our preliminary calculations.

We have performed a series of calculations as a function of temperature from 25 °C to 400 °C using both the VRM and LRM models to examine and compare the model predictions. We have discussed the effect of temperature on the radiolysis kinetics at temperatures below 250 °C and at a relatively low dose rate of 4.5 kGy·h^{-1} in the earlier chapters. For the calculations presented in this chapter we used a single radiation dose rate of 1000 kGy·h^{-1} to more closely simulate the proposed SCW reactor coolant conditions. All calculations start with pure water prior to a step function initiation of a continuous radiation flux. For liquid water, the system pressure was the saturation pressure at the target temperature. For vapour and SCW there can be many different combinations of temperature and pressure. To reduce the scope of work, the VRM calculations at any given temperature were performed at the saturation pressure at that temperature. The saturation pressure and water density [17] are listed in Table 8.2 for a number of temperatures. In both LRM and VRM calculations changes in water density affect the amount of radiation energy absorbed

per volume. In the VRM model calculations, the water density also affects the pseudo 2nd

order rate constants used for three-body reactions involving a water molecule.

Table 8.2: Densities of liquid water and water vapour as a function of temperature [IAPWS-IF97].

Temp (^{o}C)	Saturation Pressure (MPa)	Liquid Density (g·cm^{-3})	Vapour Density (g·cm^{-3})
25	0.003	0.997	2.31×10^{-5}
100	0.101	0.958	59.8×10^{-5}
150	0.476	0.917	2.55×10^{-3}
200	1.555	0.865	7.86×10^{-3}
250	3.976	0.799	19.96×10^{-3}
300	8.588	0.712	46.2×10^{-3}
350	16.529	0.575	0.114
374	22.064	0.322	0.322

8.3.1   Radiolysis product concentrations predicted by the LRM

The calculated time evolution of radiolysis product concentrations at three different temperatures representing normal liquid water (200 °C), sub-critical water (350 °C), and supercritical water (400 °C) are presented in Figure 8.2.   The radiolysis product concentrations in sub- and supercritical water show a similar time-dependent behaviour to that observed in liquid water. At times shorter than ~ 0.1 ms (Stage I) the concentrations of the primary radiolysis products, ($\bullet e_{aq}^- + \bullet H$), $\bullet OH$, H_2 and H_2O_2, all increase nearly linearly with time (i.e., the slope of log C vs log t is ~1). The rate of increase in the concentration of each species is nearly proportional to G-value $\times$ dose rate $\times$ density indicating that no

significant aqueous reactions of these species has occurred within this short time scale, as expected. However, as their concentrations build up chemical reactions between the primary radiolysis products occur at appreciable rates. As these reactions produce secondary products such as $\bullet O_2^-$, $HO_2\bullet$ and O_2, the concentrations of the secondary radiolysis products start to increase at faster rates than those of the primary products in Stage II (10 ms – 100 ms). As the concentrations of the secondary radiolysis products reach levels similar to those of the primary radiolysis products and the chemical reactions of the secondary products with the primary radiolysis products become significant the system reaches steady state (Stage III).
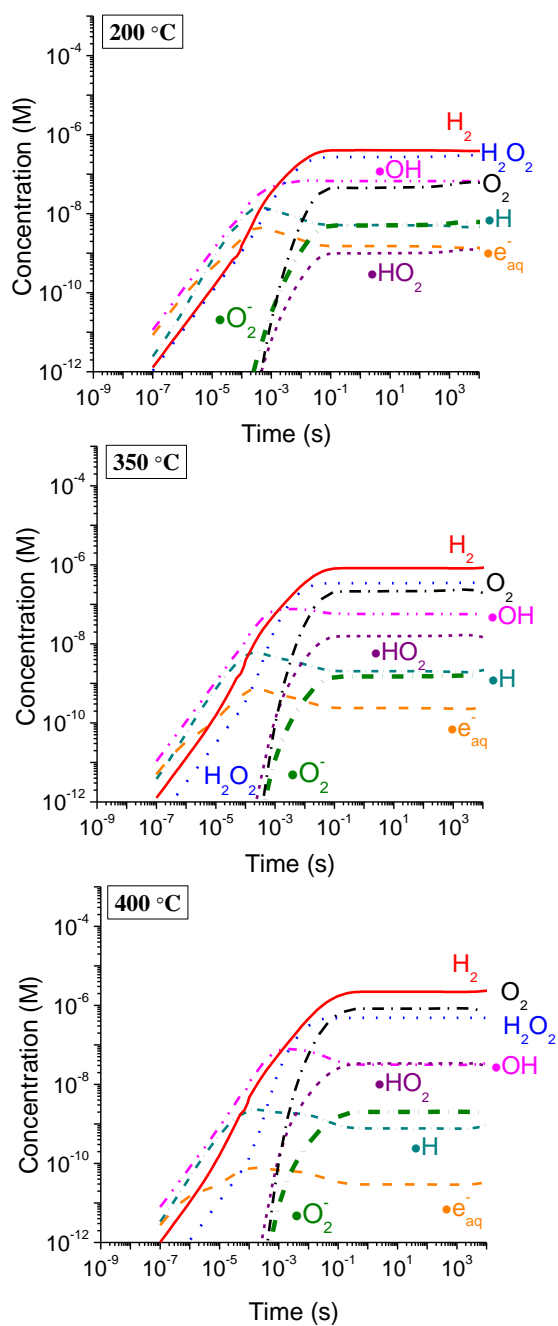
Figure 8.2: Time evolution of radiolysis product concentrations predicted by the LRM at 200 °C (liquid water), 350 °C (sub-critical water) and 400 °C (supercritical water) at a dose rate of 1000 kGy·h⁻¹.

As the rates of the chemical reactions of the radiolysis products approach their production rates their concentrations reach pseudo steady-state. The concentration of a more reactive species reaches pseudo steady-state faster. Hence, the concentrations of the primary radical products ($\bullet e_{aq}^-$, $\bullet H$, $\bullet OH$) reach a steady-state first (within ~ 0.1 ms) while the primary molecular products and secondary products all reach a steady-state in 10 ms − 100 ms. The time for the whole chemical system to reach a steady-state increases slightly with temperature, from ~ 10 ms at 200 °C to ~ 100 ms at 400 °C.

8.3.2   Radiolysis product concentrations predicted by the VRM

The VRM was also used to calculate the time evolution of the radiolysis of water vapour at the same temperatures used in the LRM calculations. The results for all temperatures are very similar as illustrated in Figure 8.3. The concentrations of the primary radiolysis products $\bullet H$, $\bullet OH$, $\bullet O$ and H_2 all increase linearly with time initially. The time required reaching an initial pseudo steady-state value varies considerably from species to species. The less chemically reactive the species, the longer it takes to reach steady-state and the higher concentration it reaches at steady-state. As a result, the VRM predicts $[\bullet H]_{SS} < [\bullet OH]_{SS} < [\bullet O]_{SS} < [H_2]_{SS}$. The concentration of $\bullet OH$ reaches pseudo steady-state by ~0.01 ms, a slightly shorter time scale than that predicted for the same point with the LRM. It takes longer, ~ 0.1 s, for the less reactive radical, $\bullet O$, to reach steady-state. The concentration of $\bullet H$ also reaches pseudo steady-state by ~0.01 ms but its concentration is very low and hence is not shown in Figure 8.3.
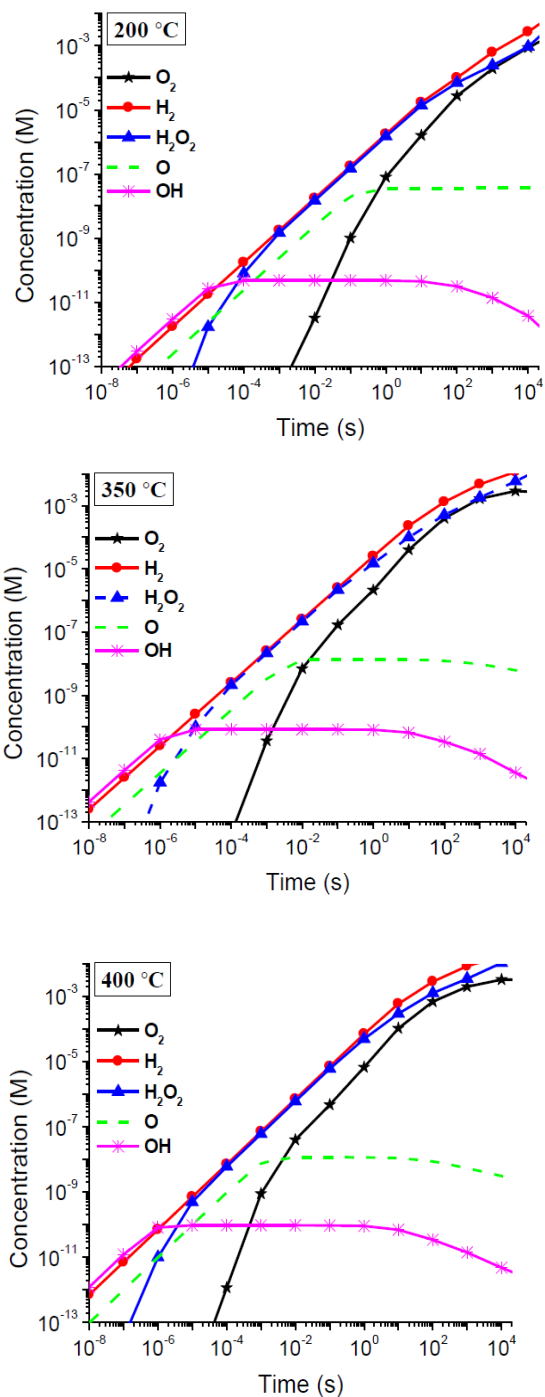
Figure 8.3: Time evolution of radiolysis product concentrations predicted by the VRM at 200 °C (water vapour), 350 °C (sub-critical water) and 400 °C (supercritical water) at a dose rate 1000 kGy·h^{-1}.

The concentrations of the secondary products, H_2O_2 and O_2, increase at faster rates initially ($\propto t^2$), but their increase slow down to be approximately linear with t after the concentrations of •OH and •O approach near steady-state. By 0.1 s their concentrations reach levels similar to that of primary radiolysis product H_2. The ratios of the concentrations of the radical primary radiolysis species at short times (t < 1 s) do not change much with temperature, but the concentrations of molecular products, H_2, O_2 and H_2O_2 increase continually with time and do not reach steady-state within the durations modelled (up to 10^4 s).

8.3.3   Comparison of the Temperature Dependences Predicted by VRM and LRM

Since the concentrations of different radiolysis products evolve at different rates with time, the effect of temperature was examined by comparing the two different model predictions at two different times, after 1 s in Figure 8.4 and after 1 h (3600 s) in Figure 8.5. For the LRM a change in temperature has a small impact on the radiolysis product concentrations at 1 s and a larger impact at 1 h. This is because the slower, more temperature dependent, chemical reactions in the water phase become increasingly more important in determining the steady-state concentrations.

With the VRM the temperature dependence of the radiolysis product concentrations is more pronounced in the lower temperature range (< 150 °C), but it diminishes at temperatures > 200 °C (Figure 8.4 and Figure 8.5). An important factor that complicates the interpretation of these results is that the VRM calculations were performed at different pressures at different temperatures. The water vapour saturation pressure at a given

temperature was used (Table 8.3). As a result the water vapour density changed considerably with temperature.   An increase in water vapour density increases the rate of energy absorption per unit volume ($\rho \cdot D_R$) and the rates of the primary radiolysis product formation. An increase in water vapour density also increases the rates of termolecular reactions that involve water molecules. The net consequence of increased water vapour density is that the concentrations of molecular species, H_2O_2, H_2, and O_2, all increase by about an order of magnitude when the temperature increases from 200 °C to 400 °C.   The increasing divergence in the LRM and VRM predictions with increasing time is consistent with our understanding of how they model radiolysis and chemistry. At short times the oxidizing species concentrations should depend more strongly on the primary radiolysis production rates than on the reactions of secondary radiolysis products.

It is encouraging to see that the range of differences in the two model predictions is relatively moderate at short times (< 1 s). This shows that the two different approaches for extrapolating the rate constants used in the VRM and LRM are useful and could provide bounding values for the chemical consequences of irradiation of SCW.
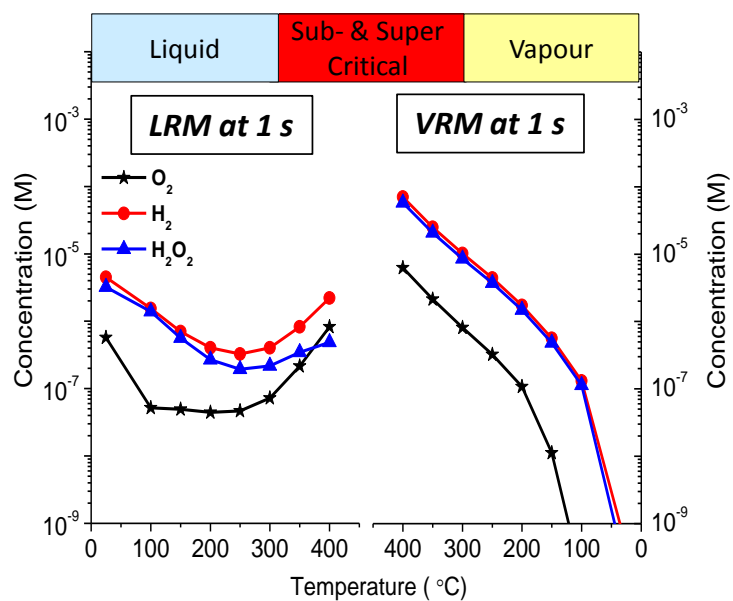
Figure 8.4: Radiolysis product concentrations as a function of temperature predicted by the LRM and VRM after 1 s of irradiation at a dose rate of 1000 kGy·h^{-1}.
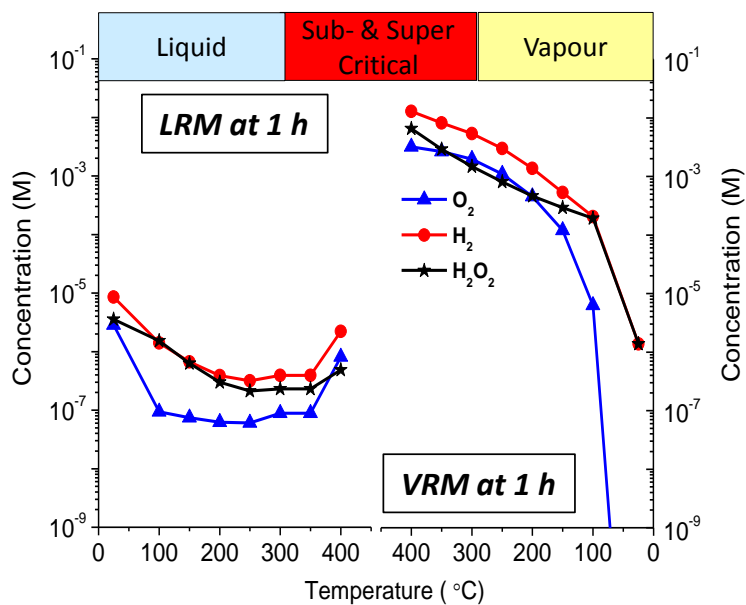
Figure 8.5: Radiolysis product concentrations as a function of temperature predicted by the LRM and VRM after 1 h of irradiation at a dose rate of 1000 kGy·h^{-1}.

8.3.4 Suppression of Water by H_2 Addition

Suppression of the net production of oxidizing radiolysis species by H_2 addition is a common practice in pressurized light and heavy water reactors [18–20]. The effects of H_2 addition on the radiolysis of SCW (at 24 MPa, 0.148 $g \cdot cm^{-3}$ water density) after 1 s at 400 °C as predicted by the LRM are shown in Figure 8.6. The calculations shows that H_2 addition could suppress the radiolytic production of O_2; the $[O_2]$ at both 1 s and 1 h is below 10^{-11} $mol \cdot dm^{-3}$ when $[H_2]_0 > 10^{-4}$ $mol \cdot dm^{-3}$ is added. However, addition of H_2 is less effective at suppressing H_2O_2; the $[H_2O_2]$ at both 1 s and 1 h remains at $\sim 10^{-7}$ $mol \cdot dm^{-3}$, even when $[H_2]_0 > 10^{-2}$ $mol \cdot dm^{-3}$ is added.

Figure 8.6: **Radiolysis product concentrations as a function of initial H_2 addition predicted by the LRM after 1 s and 1 h of irradiation at 400 °C and 1000 kGy·h^{-1}.**

The VRM predicts that addition of any reasonable amount of H_2 will not suppress the production of either O_2 or H_2O_2 after 1 s or 1 h (Figure 8.7). A similar result is seen at longer

times where the steady-state concentrations of O_2 and H_2O_2 are even higher. The only discernable effect of H_2 addition is a reduction in the [$\bullet$O] with $[H_2]_0 > 10^{-4}$ M due to the reaction:

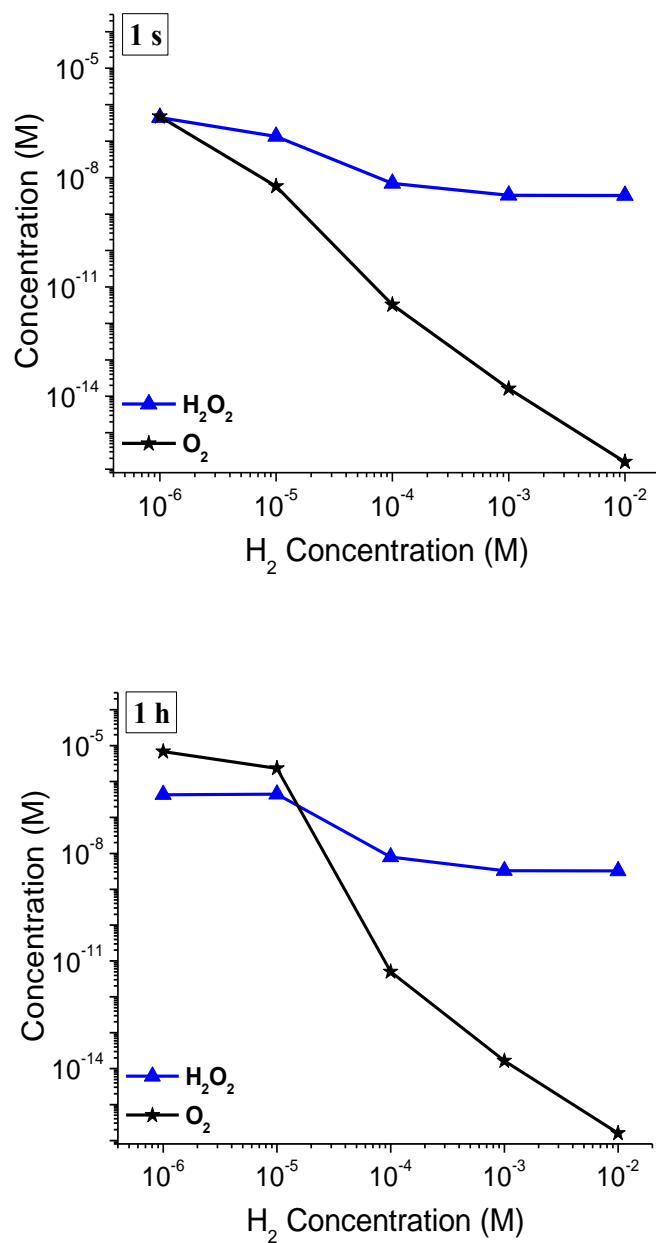$$\bullet O + H_2 \rightarrow \bullet OH + \bullet H \tag{8.3}$$

Figure 8.7: Radiolysis product concentrations as a function of initial H_2 concentration predicted by the VRM after 1 h of irradiation at 400 °C at a dose rate of 1000 kGy·h^{-1}.

8.3.5   Temperature Dependence of the Radiolysis of Supercritical Water

At this point we cannot extrapolate the values of rate constants of chemical reactions in liquid water to rate constants for the same reactions in SCW. Supercritical water will be more and more vapour-like as temperatures increase above 374 °C and hence our interest in using a VRM. The VRM predictions of the temperature dependence of the key molecular radiolysis products at 1 s and 1 h are presented in Figure 8.8 and Figure 8.9 respectively. The VRM predicts that a change in temperature over the range of 400 °C to 600 °C has only a small impact on the concentrations of H_2 and O_2 at both short and long times. Increasing temperature has a more significant impact on the concentration of H_2O_2, which is predicted to decrease by about one order of magnitude as the temperature is increased from 400 °C to 600 °C. If this result is verified, it could indicate that the coolant in an SCWR could be less chemically aggressive at higher temperatures, a result that is non-intuitive, but which could be beneficial.

Figure 8.8: Radiolysis product concentrations as a function of temperature predicted by the VRM after 1 s of irradiation at a dose rate of 1000 kGy·h⁻¹.
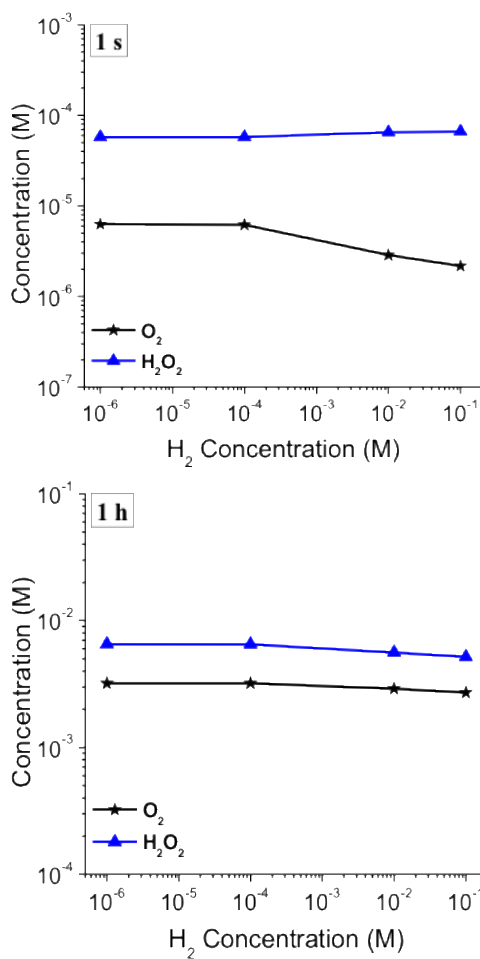

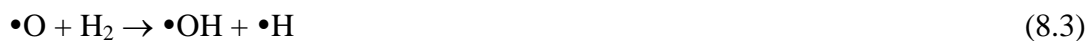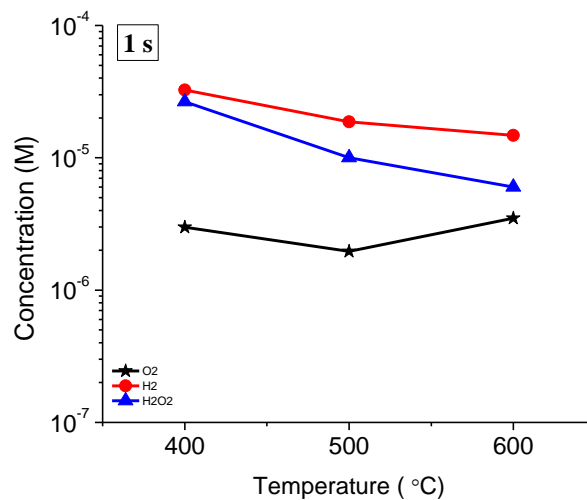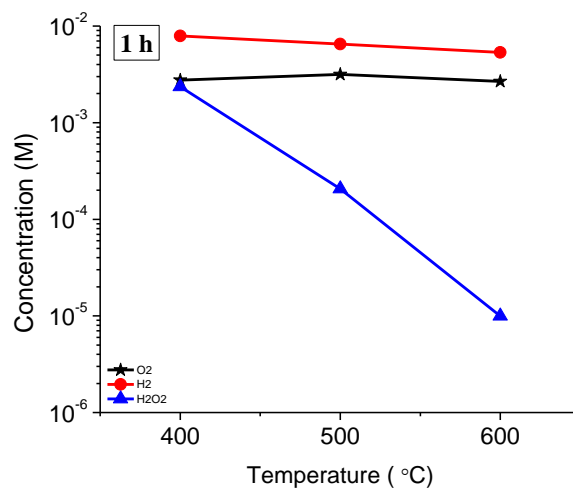**Figure 8.9: Radiolysis product concentrations as a function of temperature predicted by the VRM after 1 h of irradiation at a dose rate of 1000 kGy·h⁻¹.**

8.4   Conclusion

We have begun to develop a predictive model for the chemistry driven by radiation in supercritical water. Owing to the paucity of data available, we are approaching the modelling effort with a parallel approach. We are developing two models based on the radiolysis of liquid water or water vapour. The starting points for both models are the sets of primary radiolysis G-values, and chemical reactions and rate constants that are available in the literature. We have assembled first versions of both a liquid radiolysis model (LRM) and a vapour radiolysis model (VRM) based on extrapolations of literature data.

Primary calculations with both models for supercritical water radiolysis show noteworthy results. Both models predict similar concentrations of key molecular species after a short irradiation time (1 s) at 400 °C; the concentrations of key molecular oxidants, O_2 and H_2O_2, were in the range 10^{-5} and 10^{-4} mol·dm^{-3}. Though, as the irradiation time increases the gap between the two predictions widens. Also, both models predict that addition of H_2 will not be effective in suppressing the concentration of H_2O_2 that is generated by the radiolysis of supercritical water.

8.5   References

[1]   M. Zychová, A. Vojáček, M. Růžičková, R. Fukač, E. Křečanová, "New Research Infrastructure for SCWR in Centrum Výzkumu Řež", The 6th International Symposium on Supercritical Water-Cooled Reactors, March, 2013, Shenzhen, Guangdong, Chin4.
[2]   T.K. Yeh, M.Y. Wang, H.M. Liu, M. Lee, "Modeling Coolant Chemistry in a Supercritical Water Reactor", Transactions, Topsafe2012, Safety in Reactor Operations, Helsinki, Finland, April, 2012, 457.

[3]   J.C. Wren, J.M. Ball, "LIRIC 3.2 an Updated Model for Iodine Behaviour in the Presence of Organic Impurities", *Radiation Physics and Chemistry,* 60, 2001, 577.

[4]   J.C. Wren, G.A. Glowa, "A Simplified Kinetic Model for the Degradation of 2-Butanone in Aerated Aqueous Solutions under Steady-State Gamma-Radiolysis", *Radiation Physics and Chemistry*, 58, 2000, 341.

[5]   J.M. Joseph, B.S. Choi, P. A. Yakabuskie, J.C. Wren, "A Combined Experimental and Model Analysis on the Effect of pH and O_2(Aq) on γ-Radiolytically Produced H_2 and H_2O_2", *Radiation Physics and Chemistry*, 77, 2008, 1009.

[6]   P.A. Yakabuskie, J.M. Joseph, J.C. Wren, "The Effect of Interfacial Mass Transfer on Steady-state Water Radiolysis", *Radiation Physics and Chemistry*, 79, 2010, 777.

[7]   P.A. Yakabuskie, J.M. Joseph, C.R. Stuart, J.C. Wren "Long-term γ-radiolysis Kinetics of NO_3^- and NO_2^- Solutions", *Journal of Physical Chemistry A,* 115, 2011, 4270.

[8]   O.P. Arkhipov, A.O. Verkhovskaya, S.A. Kabakchi, A.N. Ermakov, "Development and Verification of a Mathematical Model of the Radiolysis of Water Vapor", *Atomic Energy*, 103, 2007, 870.

[9]   A.J. Elliot, D.M. Bartel, "The Reaction Set, Rate Constants and g-Values for the Simulation of the Radiolysis of Light Water over the Range 20° to 350°C", AECL Report 153-127160-450-001, Chalk River, Canada, 2009.

[10] M. Lin, Y. Katsumura, Y. Muroya, H. He, G. Wu, Z. Han, et al., "Pulse Radiolysis Study on the Estimation of Radiolytic Yields of Water Decomposition Products in High-Temperature and Supercritical Water: Use of Methyl Viologen as a Scavenger", *Journal of Physical Chemistry A*, 108, 2004, 8287.

[11] J.F. Wishart, P. Neta, "Spectrum and Reactivity of the Solvated Electron in the Ionic Liquid Methyltributylammonium Bis(trifluoromethylsulfonyl)imide", *Journal of Physical Chemistry B*, 107, 2003, 7261.

[12] A.A. Galkin, V.V. Lunin, "Subcritical and Supercritical Water: A Universal Medium for Chemical Reactions", Russian Chemical Reviews,74, 2005, 21.

[13] J.R. Cooper, Q. Mary, M.E. Road, S.I. Associates, Revised Release on the IAPWS Industrial Formulation 1997 for the Thermodynamic Properties of Water and Steam, The International Association for the Properties of Water and Steam, Lacerne, Switzerland, 2012.

[14] W.L. Marshall, E.U. Franck, "Ion Product of Water Substance, 0–1000 °C, 1–10,000 bars New International Formulation and its Background", *Journal of Physical and Chemical Reference Data,* 10, 1981, 295.

[15] D. Guzonas, F. Brosseau, P. Tremaine, J. Meesungnoen, J.P. Jay-Gerin, "Water Chemistry in a Supercritical Water-cooled Pressure Tube Reactor", *Nuclear Technology*, 179, 2012, 205.

[16] D. Janik, I. Janik, D.M. Bartels, "Neutron and β/γ Radiolysis of Water up to Supercritical Conditions. 1. β/γ Yields for H_2, ·H Atom, and Hydrated Electron.", *Journal of Physical Chemistry A*, 111, 2007, 7777.

[17] A.A. Alexandrov, B.A. Grigoriev, "The Tables of Thermophysical Properties of Water and Steam", MPEI Publication house, Moscow, 1999.

[18] P. Millet, "PWR Primary Water Chemistry Guidelines: Volume 1, Revision 4, EPRI, Palo Alto, CA, TR-105714-V1R4, 1999.

[19] D.M. Bartels, J. Henshaw, H.E. Sims, "Modeling the Critical Hydrogen Concentration in the AECL Test Reactor", *Radiation Physics and Chemistry*, 82, 2013, 16.

[20] H. Christensen, "Remodelling of the Oxidant Species during Radiolysis of High Temperature Water in a Pressurized Water Reactor", *Nuclear Technology*, 109, 1995, 373.

CHAPTER 9

Conclusion and Future Work

The research goal was to develop a sufficient understanding of steady-state radiolysis kinetics of SCW to be able to predict with reasonable accuracy the concentrations of key oxidizing species as a function of the proposed Canadian SCWR coolant conditions. Towards this goal, the objectives of this work were: (1) to develop a reliable experimental method to determine the concentrations of water radiolysis products, primarily H_2 and O_2, formed under γ-irradiation of sub- and supercritical water (SCW), and (2) to develop a chemical kinetic model for the radiolysis of sub- and supercritical water and to perform sensitivity analysis of the model to radiation and solution conditions.

Under objective (1) we have developed and tested a few design options for a test cell that can be used for the study of radiolysis kinetics of high-temperature liquid water and steam, subcritical and supercritical water. We have successfully conducted radiolysis kinetic tests at temperatures up to 250 °C. The cell design modification is continuing.

For objective (2) our current understanding of chemical reaction kinetics in sub-critical and supercritical water is not sufficient to construct a fully validated model for the γ-radiolysis of SCW under continuous (> ms) irradiation. In particular the effects of the changing water properties in the sub- and supercritical regimes are not fully understood. Thus, we have used a two-pronged approach to the kinetics modeling coming from high density (liquid-like) and low-density (vapour-like) perspectives and hence creating two

models: (1) a liquid radiolysis model (LRM) and (2) a vapour radiolysis model (VRM) for the continuous radiolysis of sub-critical and supercritical water. The two SCW radiolysis models are based on an existing liquid water radiolysis model and an existing water vapour radiolysis model. To extend the application of these models to SCW conditions with any confidence, the radiolysis kinetics of liquid water and water vapour as a function of temperature and pressure should be well understood.

Thus, under objective (2) we have modified the existing radiolysis models for liquid water and vapour to extend their application ranges to high temperatures and high pressures. The reactions considered in these models include primary radiolytic production of water decomposition products and the homogeneous chemical reactions of the radiolysis products in either aqueous or gas phase. In these models the detailed kinetics of the radiolytic processes were not modelled in detail. Instead the models used G-values for the creation of primary radiolysis products and the rate of radiation energy deposition into water. The kinetics of homogeneous phase chemical reactions were modelled using the classical chemical kinetics rate equations. In the models the rate parameters, mainly the G-values and the rates constants of the elementary chemical reactions, are defined as a function of temperature. Thus, although these models have not been validated extensively at higher temperatures, they have the capability to predict the evolution of the concentrations of radiolysis products as a function temperature. Using these models we have performed a series of calculations to determine the effect of pH and temperature on the net production of radiolysis products in liquid water and the effects of pressure and temperature on the net production of radiolysis products in water vapour.

For γ-radiolysis of liquid water for a given set of conditions (pH, temperature and dose rate) the concentrations of radiolysis products show three distinct periods over the time span of 0 to 10^4 s (~ 3 h) (where time 0 corresponds to initiation of the radiation flux). In all cases, in Stage I (< 1 ms) the concentration of a radiolysis product increases linearly with time at a rate determined by primary radiolytic processes, except for $•e_{aq}^-$. The concentrations of the less reactive radicals, •H and •OH, increase for a longer time before they reach steady state in Stage II. In Stage II, the concentrations of the primary molecular products, H_2 and H_2O_2, continue to increase nearly linearly with time and the concentrations of the secondary products, $•O_2^-$, $•HO_2$ and O_2, start to accumulate at very fast rates. As the concentrations of H_2O_2 and H_2 as well as the secondary products continue to increase in Stage II, the net rates of their decomposition reactions also increase and become equal to the net rates of their production rates. The whole radiolysis system approaches steady state (Stage III).

We have shown that for γ-radiolysis of liquid water, the net production rates of radiolyis products in Stage I depend largely on their primary radiolytic production rates (G-value × water density × dose rate). In this regard, the production rates of $•e_{aq}^-$ and •H should be considered together due to the fast forward reaction between them. We have shown that temperature has negligible effect on the primary radiolytic production rates; the greatest change occurs for H_2O_2 but even then, the rate decreases only by a factor of 2 when the temperature increases from 25 °C to 300 °C. However, as the concentrations of the primary molecular species and the secondary products increase their reactions become progressively more important in controlling the concentrations of the radiolysis products at later stages (>

ms). Since the chemical reaction rates increase with temperature, the whole radiolysis system reaches steady state at a slightly faster rate at a higher temperature; within 1 s at temperatures ≥ 150 °C. The liquid water radiolysis model predicts that the steady state concentrations of H_2 and H_2O_2 should decrease by an order of magnitude when temperature increases 25 °C to 250 °C. The steady-state concentration of secondary product O_2 should decrease with temperature at T ≤ 80 °C but starts to increase with temperature at T ≥ 150 °C. The variation of the O_2 concentration is within an order of magnitude.

The pH affects the $[\bullet e_{aq}^-]$ and $[\bullet H]$ at very early times in Stage I via the acid-base equilibrium of $\bullet e_{aq}^- + H^+ \leftrightarrows \bullet H$. At a $pH_{25^{\circ}C} > pKa$ of $\bullet H$, at temperatures below ≤ 80 °C, $[\bullet e_{aq}^-]$ increases to a level similar to that of $[\bullet OH]$ by the time when the secondary products are formed at substantial levels. At such conditions cyclic reactions between $\bullet e_{aq}^-$ and $\bullet OH$, and secondary products can accelerate the removal of $\bullet e_{aq}^-$ and $\bullet OH$ without affecting the secondary products. Due to the catalytic cycles, pH can have significant effect on the behaviour of radiolysis products in Stage II and Stage III. Thus, at temperatures ≤ 80 °C, the radiolysis kinetics behaviour in Stage II at pH 10.6 is markedly different from the behaviour observed at lower pHs and steady-state is reached at a longer time. However, the effect of pH diminishes as temperature increases.

Water vapour model calculations show that although the absolute concentrations of radiolysis products depend on temperature, their time-dependent behaviours are very similar at all temperatures. At a given temperature, the concentrations of the primary radiolysis products, $\bullet H$, $\bullet OH$, $\bullet O$ and H_2, all initially increase linearly with time and then reach steady

state. The chemically more reactive species reach steady state at earlier times. The most reactive species ($\bullet$H) reaches steady state very early whereas the less chemically reactive radicals, $\bullet$OH and $\bullet$O, take longer to reach steady state (< 0.1 ms and < 1 s, respectively at 150 °C). (Unlike for the water radiolysis model, the species $\bullet e_{aq}^-$ is not considered because ions are not stabilized in dilute water vapour.) We have shown that the reactions of the primary radical species, $\bullet$H, $\bullet$OH and $\bullet$O, are the main production precursors for the molecular products, H_2, H_2O_2 and O_2, respectively. Thus, the water vapour model predicts that the concentrations of H_2 and H_2O_2 start to increase at very early times at linear rates related to the G-values of the respective reactant radicals. As temperature increases the concentrations of the reactive radicals reach steady state at earlier times. Consequently the concentrations of the less reactive molecular species start to increase at a linear rate at earlier times. The net consequence of the increases in both the radiolytic production and gas phase reaction rates is that the concentrations of molecular species, H_2O_2, H_2, and O_2, all increase proportionally with $\rho(T){\cdot}D_R$ when the temperature increases from 100 °C to 400 °C. At the lower temperatures the concentrations of the molecular species do not follow the simple linear dependence on $\rho(T){\cdot}D_R$.

In Chapter 7 we have presented experimental results from the radiolysis of biphasic liquid-vapour water system at 25 °C, 150 °C and 250 °C, and compared them with the model simulation results using the liquid and vapour radiolysis models. Model calculations were capable of reproducing experimental results. As temperature increases the saturation pressure (water vapour density) in the headspace increases, and the production of the molecular radiolysis products, H_2, H_2O_2 and O_2 in the vapour phase dominates the net production in the

biphasic system. The model simulation results show that the contribution from the radiolysis of liquid phase to the net production of H_2 and H_2O_2 in a leak-tight radiolysis cell is negligible at $T \geq 150$ °C. This suggests that at temperatures near critical region, when water approaches the supercritical fluid state, model predictions based on an extension to the low pressure water vapour radiolysis model may be more useful. In the model simulations of the biphasic water system we have performed the calculations using each model independently. In the future study, efforts should be made to merge the two radiolysis kinetic models and include the interfacial transfer of the molecular species as a function of time.

We have begun to develop a predictive model for the chemistry driven by radiation in SCW. Owing to the paucity of data available, we approached the modelling effort with a parallel approach, developing two models based on the radiolysis of liquid water or of water vapour. Our aim is to have the models converge as they mature. In Chapter 8 we have described the rationales behind this approach, the assignment of the kinetic parameters (G-values and rate constants) at the SCW temperatures and pressures, and analysis of the modelling results.

Preliminary calculations with both models show interesting results. Both models predict similar concentrations of key molecular species after a short irradiation time (1 s) at 400 °C; the concentrations of key molecular oxidants, O_2 and H_2O_2, were in the range 10^{-5} and 10^{-4} mol·dm^{-3}. The gap between the two predictions, however, widens as the irradiation time increases. As well, both models predict that addition of H_2 will not be effective in

suppressing the concentration of H_2O_2 that is generated by the radiolysis of supercritical water.

A considerable number of approximations and assumptions were made in assembling the first versions of the radiolysis models. The effects of changes in the temperature-dependant properties of water have not been included in the models. Further critical evaluations of the input parameters in the models are needed to improve their applicability. A more comprehensive analysis of modelling results would be very useful to identify the key reactions and reaction rate parameters that are important in determining the net radiolytic production of H_2, O_2 and H_2O_2 under reactor coolant conditions.

Irradiation experiments on sub- and supercritical water are extremely difficult due to the high temperatures and pressures that are involved. The challenge is further compounded for γ-radiolysis studies where extra safety precautions are required, physical restrictions in the irradiation volume are present, materials selection is challenging, and sampling is delayed due to the necessary cool-down period for the reaction vessel.

The high temperature radiolysis studies should be continued to include more tests at subcritical and supercritical temperatures. That requires the development of a radiolysis test cell for experiments in the supercritical region. We describe the initial steps in the development and evaluation of possible test cell options. There have been failures and indication of a design direction leading to success. Much future work is required to explore and improve the high temperature test cell design, and then to use this design to establish a database for model evaluation and validation.

Curriculum Vitae

Name: Nastaran Yousefi

Post-secondary Education and Degrees:

Islamic Azad University, Tehran North Branch
Tehran, Iran
2005-2009.

The University of Western Ontario
London, Ontario, Canada
2012-2014.

Related Work Experience

Teaching Assistant
The University of Western Ontario
2012-2014

Research Assistant
The University of Western Ontario
2012-2014

Management Assistant
Kolon I'Networks Corp., Tehran Branch
2009- 2012

Research Assistant
Islamic Azad University, Tehran North Branch
Sep. 2008-Dec.2008

Publications:

N. Yousefi, J. M. Joseph, V. Subramanian, J. C. Wren, "The Effect of Radiolysis on Material Degradation Under Sub and Supercritical Water Conditions", in the proceedings of 38th Annual Student Conference of the Canadian Nuclear Society, Vancouver, Aug 24-28 (2014), 5 pages.
N. Yousefi, J. M. Joseph, V. Subramanian, J. C. Wren, "Chemical Kinetics Models for the Gamma-Radiolysis of supercritical Water", AECL, (2014), 40 pages.
N. Yousefi, J. M. Joseph, L. M. Alrehaily, J. C. Wren, "Effect of High Temperature on the Steady State Radiolysis Product Behaviour", in the proceedings of 37th nnual Student Conference of the Canadian Nuclear Society, Toronto, June 9-12 (2013), 5 pages.

Poster Presentations (Presenting author bolded):
N. Yousefi, J. M. Joseph, V. Subramanian, J. C. Wren, "The Effect of Radiolysis on Material Degradation ☐Under Sub and Supercritical Water Conditions", Canadian Nuclear Society, Vancouver, BC, Aug 2014.

P. Yakabuskie, **N. Yousefi**, J. M. Joseph, J. J. Noël, J. C. Wren, "Radiation-Based Technology For Waste ☐Treatment", Sustainability and Environment Research Showcase, London, ON, Mar 2014.

N. Yousefi, J. M. Joseph, J. C. Wren, "Effect of Temperature on the Steady-State Concentrations of Water ☐Radiolysis Products", University Network of Excellence in Nuclear Engineering, Toronto, ON, Dec 2013.

N. Yousefi, J. M. Joseph, L. M. Alrehaily, J. C. Wren, "Effect of High Temperature on the Steady-State Radiolysis Product Behaviour", Canadian Nuclear Society, Toronto, ON, Jun 2013.